

Wayne State University Dissertations


January 2018

Analysis Of Micromixers To Minimize Scaling Effects On Reverse Osmosis Membranes

Jeremy Walker

Wayne State University, jeremy.walker2@wayne.edu

Follow this and additional works at: https://digitalcommons.wayne.edu/oa_dissertations

 Part of the [Civil Engineering Commons](#), and the [Environmental Engineering Commons](#)

Recommended Citation

Walker, Jeremy, "Analysis Of Micromixers To Minimize Scaling Effects On Reverse Osmosis Membranes" (2018). *Wayne State University Dissertations*. 2132.

https://digitalcommons.wayne.edu/oa_dissertations/2132

This Open Access Dissertation is brought to you for free and open access by DigitalCommons@WayneState. It has been accepted for inclusion in Wayne State University Dissertations by an authorized administrator of DigitalCommons@WayneState.

ANALYSIS OF MICROMIXERS TO MINIMIZE SCALING EFFECTS ON REVERSE OSMOSIS MEMBRANES

by

JEREMY STEPHEN WALKER

DISSERTATION

Submitted to the Graduate School

of Wayne State University,

Detroit, Michigan

in partial fulfillment of the requirements


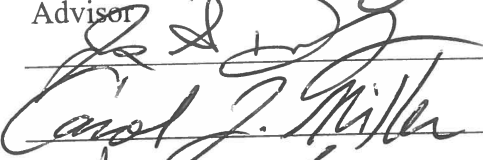


for the degree of

DOCTOR OF PHILOSOPHY

2018

MAJOR: CIVIL ENGINEERING

Approved By

	11/6/2018
Adviser	Date
	10/26/2018
Carol J. Miller	10/26/2018
	10/26/2018
Zhang	10/26/2018
	10/26/18
Dean	10/26/18

© COPYRIGHT BY
JEREMY STEPHEN WALKER
2018
All Rights Reserved

ACKNOWLEDGMENTS

I wish to acknowledge the following individuals who have made possible the completion of this PhD:

Dr. McElmurry for his support and professional guidance throughout the course of this research and who pushed me to meet the deadlines.

Dr. Dusenbury for his advice and encouragement during this journey. The weekly meeting that forced me to split my time efficiently between my daily work and research.

My family still at home Christie, Kelsey, and Zachary for their patience and understanding and those who are away Kaley and Kylyn.

My twin brother Shawn who always pushed me to achieve more than I thought I could or should by example.

My Dad who inspired me to become a civil engineer and who set the bar so high I can only hope to achieve what he accomplished.

My Mom and Step-Dad who were always available for a phone call and always willing to listen.

TABLE OF CONTENTS

Acknowledgments	ii
List of Tables.....	iv
List of Figures	v
Chapter 1: Introduction.....	1
Chapter 2: Background	5
Chapter 3: Direct Print Micromixers for Enhanced Fluid Flow.....	19
Introduction	19
Material and Methods	23
Results	30
Discussion.....	49
Conclusion.....	52
Chapter 4: Direct Printing of Micromixers on Reverse Osmosis Membrane Surfaces Reduce Chemical Fouling	53
Introduction	53
Material and Methods	57
Results	63
Discussion.....	75
Conclusion.....	78
Chapter 5: Reverse Flow Feature of Micromixer for Enhanced Cleaning.....	80
Introduction	80
Material and Methods	83
Results	86
Discussion.....	95
Conclusion.....	97
Chapter 6: Significance & Conclusions.....	98
Appendix A	104
Appendix B.....	106
References.....	111
Abstract	118
Autobiographical Statement.....	120

LIST OF TABLES

Table 2.1 Summary of pretreatment options (adapted from Solutions 2010).....	14
Table 3.1 Breakdown showing how the percent area was calculated for the 90 degree angle.....	35
Table 3.2 Breakdown to show how the percent coverage for the ten models were calculated. The optimal design is highlighted in green.....	36
Table 3.3 The percent coverage in the defined feed channel for each velocity region of interest as a comparable unit area of quantification for the ten models evaluated. The optimal design is highlighted in green having the highest enhanced zone and minimal fouling zones.	53
Table 4.1 Elemental concentration of calcium and sulfur from XRF verifying calcium sulfate scale was the only foulant present.....	71

LIST OF FIGURES

Figure 2.1: Solution-diffusion model – (adapted from Wijmans and Baker 1995).....	8
Figure 2.2: Image of a 0.508 mm (20 mil) mesh feed spacer on top of a RO membrane under normal typical operating conditions in a transparent acrylic cross flow cell (Sterlitech; Kent, Washington).	10
Figure 3.1: The base micromixer design was A = 90 degree chevron, offset pattern, Lc = 3mm chevron lengths, width of chevron (W) = 0.01 mm, Lg = 5.75 mm gap.	26
Figure 3.2: Pressure profile for 90 degree chevrons with an offset base design pattern that included a 3mm chevron length and 5.75 mm gap length. An inlet velocity of 0.104 m/s and a specified outlet pressure of 20.7 bar.....	31
Figure 3.3: Full velocity profile from 0 to 0.3 m/s for the 90 degree angle. To quantify flow regimes, A) an area of quantification was identified from a larger modeling area to ensure boundary conditions did not impact velocity profiles, B) the unit area of quantification was extracted, and C) the image of the unit area of quantification was transformed into a binary image for analysis to determine the amount of area with a given flow condition.	32
Figure 3.4: Full velocity profile from 0 to 0.3 m/s showing influence of angle: A) 60 degree angle B) 90 degree angle C) 120 degree angle on the amount of open channel flow and velocity regions with the base design pattern: offset, 3mm chevron length, and 5.75 mm gap inlet velocity of 0.104 m/s.....	37
Figure 3.5: Percent feed channel coverage for the enhanced zone, 0.2 to 0.3 m/s velocity profile for different angles modeled: A) 60 degree angle – 25.6% B) 90 degree angle – 39.2% C) 120 degree angle – 25.4%. The 90 degree geometry showed maximum coverage of enhanced flow conditions.	37
Figure 3.6: The different velocity zones compared for each angle modeled using the base design base pattern: offset, 3mm chevron length, and 5.75 mm gap. The 90 degree geometry provides the optimal conditions across all flow velocity ranges with 39.2 in the enhanced region. (Note: Areas presented do not include 6.3% due to chevron and 1.5% image processing error.)	39
Figure 3.7: The percent feed channel coverage for the enhanced zone, 0.2 to 0.3 m/s	

velocity profile for the continuous pattern: A) 60 degree angle – 15.3% B) 90 degree angle – 24.0% C) 120 degree angle – 29.6%. The continuous pattern decreases the area of enhanced flow conditions compared to the offset pattern.

..... 40

Figure 3.8 Full velocity profile from 0 to 0.3 m/s showing influence of continuous pattern for different angles: A) 60 degree angle B) 90 degree angle C) 120 degree angle on the amount of open channel flow and velocity regions with the base design pattern: offset, 3mm chevron length, and 5.75 mm gap inlet velocity of 0.104 m/s. The continuous pattern created channeling that increases percent coverage in the low velocity zone for all angles modeled.

..... 40

Figure 3.9: The different velocity zones compared for each angle modeled in a continuous pattern using the base design base pattern: offset, 3mm chevron length, and 5.75 mm gap. The 90 degree offset geometry provided the optimal conditions across all flow velocities with 39.2 percent coverage in the enhanced region. (Note: Areas presented do not include 6.3% due to chevron and 1.5% image processing error.)..... 41

Figure 3.10 Full velocity profile from 0 to 0.3 m/s showing influence of different gap lengths: A) 0.75 mm B) 5.75 mm C) 10.75 mm on the amount of open channel flow and velocity regions with the base design pattern: offset, 3mm chevron length, and 5.75 mm gap inlet velocity of 0.104 m/s. The micromixer gap length impacted the amount of channeling and high velocity spiking between micromixers..... 42

Figure 3.11: The percent feed channel coverage for the enhanced zone, 0.2 to 0.3 m/s velocity profile for different gap lengths: A) 0.75 mm – 9.5% B) 5.75 mm – 39.2% C) 10.75 mm – 25.2%. The 5.75mm gap length provides the highest flow coverage in the enhanced zone..... 43

Figure 3.12: The different velocity zones compared for each gap length modeled using the base design pattern: offset, 3mm chevron length, and 5.75 mm gap. The 90 degree offset geometry provided the optimal conditions across all flow velocities with 39.2 in the enhanced region. (Note: Areas presented do not include 6.3% due to chevron and 1.5% image processing error.)..... 44

Figure 3.13: Forward Full velocity profile from 0 to 0.3 m/s showing influence of different chevron lengths: A)3 mm B)4 mm C)5 mm on the amount of open channel flow and velocity regions with the base design pattern: offset, 3mm chevron length, and 5.75 mm gap inlet velocity of 0.104 m/s. As the chevron length increases, the velocity profile through the channel increases. 45

Figure 3.14: The percent feed channel coverage for the enhanced zone, 0.2 to 0.3 m/s velocity profile for different chevron lengths: A) 3 mm – 39.2% B) 4 mm – 35.7% C) 5 mm – 24.3%. The 5.75mm gap length provides the highest flow coverage in the enhanced

zone.....	46
Figure 3.15: The different velocity zones compared for each chevron length modeled using the base design pattern: offset, 3mm chevron length, and 5.75 mm gap. The 90 degree offset geometry provided the optimal conditions across all flow velocities with 39.2 in the enhanced region. (Note: Areas presented do not include 6.3% due to chevron and 1.5% image processing error.)	47
Figure 3.16: Forward flow profile front of chevron – 2 μ florescent beads with 90 degree angle, offset pattern, 5.75 mm gap and inlet velocity of 0.104 m/s supporting modeled fluid flow profile (video of tip of chevron micromixer fluorescence imaging bead flow profile available at https://doi.org/10.6084/m9.figshare.7312313.v1).	48
Figure 3.17: Forward flow profile back of chevron – 2 μ florescent beads with 90 degree angle, offset pattern, 5.75 mm gap inlet velocity of 0.104 m/s supporting modeled fluid flow profile (video of fluorescence imaging bead flow profile available at https://doi.org/10.6084/m9.figshare.7309148.v1).	49
Figure 4.1:Depiction of the two different type of scaling phenomenon that can occur with calcium sulfate initiated by boundary layer effects. Heterogeneous nucleation and surface initiated scale (Yoram Cohen, personal communication, 2018 November 4, 2018, Surface initiated Dihedral crystallization image) or bulk precipitation brought on by homogeneous nucleation followed by deposition on the feed spacer and membrane surface.....	58
Figure 4.2: Experimental RO membrane test system. System utilizes modified Sepa®CF membrane cell outfitted with 2 conductivity sensor, 2 pressure sensors, and 1 flow meter.	61
Figure 4.3: Normalized permeance and salt rejection for modified and unmodified membranes: (A) the active membrane area for the modified was 88 cm ² based on measuring the physical micromixer dimensions (B) the average active membrane area was calculated to be 120 cm ² using the average pure water flux for the unmodified membranes based on no concentration polarization effects and salt rejection being within 3% showing no membrane damage.....	67
Figure 4.4: The normalized specific flux of the modified and unmodified membranes over the course of scaling experiments. After stable filtration of a 0.340 M NaCl solution was established, the 0.0304 M CaCl and 0.0304 M NaSO ₄ scaling solutions were introduced at time point A. The ionic strength in the flow cell reached steady state at time point B. Calcium sulfate scaling initiated and equilibrated at time point C and followed	

by cake fouling of the unmodified membrane began at time point D. Average permeance (n=3) is reported with standard deviation. 71

Figure 4.5: After the scaling experiment the scaled unmodified membrane was removed and a sample was analyzed by a Bruker AXS S4 Pioneer sequential X-ray fluorescence spectrometer (XRF) which verified the scale present was calcium sulfate.. 72

Figure 4.6: Optical and SEM imaging of micromixers printed directly on the membrane surface before and after scaling experiments showing minimal scale deposition on the membrane and micromixers..... 73

Figure 4.7: Optical imaging of membrane surface and mesh feed 20 mil mesh feed spacer after scaling experiments showing heavy membrane scaling on spacer and membrane 74

Figure 4.8 SEM imaging of unmodified membrane surface utilizing a 20 mil mesh feed spacer after scaling experiments showing bulk scaling with no surface initiated scale. .. 75

Figure 4.9 Mesh feed spacer scaling in transparent crossflow cell with extensive nucleation, growth and deposition on spacer..... 76

Figure 4.10: The modified membrane with scaling in transparent crossflow cell showing minimal nucleation, growth and deposition..... 77

Figure 5.1: Fouled spiral wound reverse osmosis element (TARDEC 1998). 83

Figure 5.2: Full velocity profile from 0 to 0.3 m/s showing influence of different reverse flow velocities: A) 0.052 m/s B) 0.104 m/s C) 0.156 m/s on the amount of open channel flow and velocity regions with the optimal design pattern: 90 degree, offset, 3mm chevron length, and 5.75 mm gap..... 87

Figure 5.3: Full fluid flow profile for feed velocity of 0.104 m/s A) forward flow B) reverse flow with offset pattern, 3mm chevron length, and 5.75 mm gap, and 90 degrees. 90

Figure 5.4: Full fluid flow profile for feed velocity of 0.104 m/s A) forward flow with offset pattern, 3mm chevron length, 5.75 mm gap and 90 degree B) video of fluorescence imaging bead flow profile (available at <https://doi.org/10.6084/m9.figshare.7309148.v1>).. 91

Figure 5.5: Full fluid flow profile for feed velocity of 0.104 m/s A) reverse flow with offset pattern, 3mm chevron length, 5.75 mm gap and 90 degree B) video of fluorescence imaging bead flow profile (available at <https://doi.org/10.6084/m9.figshare.7309220.v1>). 92

Figure 5.6: Fluorescence imaging bead flow profile for A) top and B) bottom of chevron with a feed velocity of 0.104 m/s. Reverse flow with an offset pattern, 3mm chevron length, 5.75 mm gap and an angle of 90 degrees..... 93

Figure 5.7: Reverse flow effectively removed scale A) membrane scale after 24 hour scaling experiment (video available at <https://doi.org/10.6084/m9.figshare.7309208.v1>) B) reverse flow remove the majority of the scale C) minimal scale left for removal D) reverse flow cleaning after five minutes the majority of the scale was removed (video available at <https://doi.org/10.6084/m9.figshare.7309211.v1>)..... 94

Figure 5.8: Return to normal forward flow effectively removing remaining scale A) membrane scale after five minutes of reverse flow B) minimal scale left after forward flow for 30 seconds..... 95

Figure 5.9: Average water quality data for 3 modified and 3 unmodified membranes during reverse flow cleaning after membranes were scaled. At start of reverse flush water sample, time zero, showed no difference for calcium sulfate removal. Samples after 5 minutes of reverse flow and followed by return to normal operations also showed no significant difference. .. 96

CHAPTER 1: INTRODUCTION

In this dissertation a novel method for separating reverse osmosis (RO) membrane leaves in spiral wound elements is developed and evaluated. This method utilizes 3-dimensional (3D) printing with the aim of optimizing feed channels to minimize fouling potential of the membrane while maximizing permeate flux. Standard diamond shaped feed channel spacers commonly used in spiral wound membrane elements are not ideal as they are susceptible to plugging and fouling, both of which reduce membrane flux and operational life. Additionally, flow reversal with traditional feed channel spacers is not feasible due to the high pressure drop and mechanical entrapment of foulants. When foulant build up begins to decrease permeate flux membranes are typically cleaned using strong chemicals, some of which are hazardous and caustic. This cleaning step is part of routine maintenance and is initiated prior to when the extent of fouling becomes essentially irreversible. To address these limitations, this research focuses on printing microstructures in an optimized geometry and pattern directly onto the RO membrane surface to reduce fouling. Optimized microstructures were then evaluated to determine if flow reversal could successfully remove foulant buildup. By keeping the membrane surface and feed channel free of scale, the ultimate aim of this research is to evaluate if it is possible to eliminate or reduce the need for cleaning chemicals.

In **Chapter two**, the current state of science of membrane spacer design is discussed. This chapter begins with an overview of physical-chemical processes important to understand membrane filtration and fouling. Current practice for identifying fouling and typical maintenance techniques implemented by membrane operators to manage fouling

are then described. Finally, the chapter ends with a discussion of the ways researchers have attempted to reduce membrane fouling, such as by modifying the surface of membranes and alternatives to mesh feed spacers that are ubiquitous throughout the industry.

Chapter three describes the design process employed to optimize the pattern and geometry of micromixer elements printed directly to membrane surfaces. This work was guided by the hypothesis that optimized microstructure design and patterning can maximize the area of enhanced channel feed velocities (0.2 – 0.3 m/s) and minimize velocities associated with fouling (<0.1 m/s, >0.3 m/s). This process utilizes computational hydrodynamic modeling in COMSOL Multiphysics 3.0 (COMSOL Inc., Burlington, MA) to evaluate fluid flow dynamics in membrane channels. A modified BioBots 3D printer (BioBots Inc., Philadelphia, PA) was used to print patterns directly on the membrane. The use of 3D printers to modify membrane surfaces has been proposed by a few (Ho, 2008; Altman, 2010). These past studies utilized multi-step processes that were not automated and utilized equipment that deposited continuous patterns on the membrane that then had to be oven cured, making them difficult to scale up to modern industrial production. Additionally, the processes presented thus far have not allowed for the deposition of individual features that could be tailored to specific system requirements (e.g. to adjust for specific water conditions). Based on hydrodynamic models, an enhanced design and pattern of chevron micromixers were identified. Printed membranes were then subjected to laboratory experiments to confirm fluid flow profiles predicted from the theoretical models.

Chapter four details laboratory experiments conducted to compare the scaling of membranes with standard mesh feed spacers to the scaling of modified membranes with enhanced 3D printed micromixer patterning. The hypothesis that the optimal design and pattern of the micromixer identified through computational modeling, based on hydrodynamics, will minimize scaling relative to a standard feed spacer was evaluated. Membrane properties were characterized for pure water flux and salt rejection before fouling. Then a high ionic strength feed solution containing elevated concentrations of calcium sulfate was used to evaluate chemical fouling. Permeate flux was monitored over time. Microscopy was used to evaluate scale. Overall, membranes with 3D printed micromixers were found to maintain water flux longer than traditional membranes paired with mesh feed spacers.

Chapter five explores the use of reverse flow cleaning with modified membranes containing 3D printed micromixers to enhance scale removal. Accordingly, the following hypothesis was evaluated: during flow reversal, printed micromixers will create hydrodynamic conditions that enhance scale removal. Computational fluid dynamic modelling was used to evaluate flow velocities in RO feed channels during reverse flow cleaning. Theoretical results were again confirmed with laboratory experiments. Fluid flow paths observed were consistent with those predicted by computational models and enhanced scale removal was observed under reverse flow conditions.

This dissertation provides a proof-of-concept design optimization for the next generation of membrane spacers. The concept of moving away from a material insert as the means for separating membrane leaves in a spiral wound element opens up numerous

design possibilities that can be leveraged to enhance membrane transport properties and reduce fouling. The ability of printed 3D micromixers to be tailored so that the feed channel is optimized for site-specific feed water quality and the ability to vary the design of micromixers in the pressure vessels are two advances that are likely to improve membrane performance and reduce RO operational costs.

CHAPTER 2: BACKGROUND

2.0 Membrane filtration

With the majority, 97%, of the accessible water to the world being from the ocean, desalination will be required to meet a growing water demand created by industry, population growth, and the ever-changing environment. Prior to the 1990s distillation dominated the conversion of salt water to pure water. The development of reverse osmosis (RO) and its technology advancements throughout the decades have reduced its total operational footprint such as a lower membrane costs, reduced pretreatment costs, and low energy cost, 10% of the of thermal distillation making RO the current industry solution (Cohen et al. 2017).

While membrane filtration has been applied as early as 1920 in a laboratory in Germany where a microfiltration membrane was used to filter bacteria. Membranes for industrial application such as desalination weren't developed until around 1960 with the achievement of asymmetric membranes. Previously membranes were symmetric with the permeation rate being limited by the thickness of the membrane. With the development of a porous support layer that had an integrated thin dense top layer much higher flux could be achieved with thinner membranes. This is based on the fact that the flux is inversely proportional to the thickness of the barrier layer (Mulder 1991). For most membrane operations the permeation rate through the membrane is proportional to the driving pressure. Outside of the applied pressure, the membrane itself influences flux and determines selectivity. Based on this, size exclusion and molecular weight cutoff membranes can be classified into low pressure membranes and high pressure membranes.

Microfiltration (MF) and ultrafiltration (UF) are considered low pressure membrane filtration due to the typical maximum operating pressure of 40 psi required for water to pass through the membrane. While nanofiltration (NF) and RO need up to 1200 psi to produce water depending on the osmotic potential of the feed solution. The low pressure membrane processes work primarily through size exclusion not diffusion as RO and NF. The suspended particles are removed based on their size compared to the nominal or absolute pore size rating of the membrane. Pore size however is a relative term since most of the true membrane morphology is not a repeating pattern of identical cylindrical channels that reject particles above a specific pore size. Due to the process in which membranes are made they have a range of pore sizes that manufacturers attempt to classify to a “micron rating” (i.e. a measure of the membrane pore size in micrometers) for standardization purposes relating to use and sales. Membrane manufacturers typically provide the average pore size defined as nominal or the absolute (maximum) pore size. MF membranes typically have pore classifications from 0.1 to 0.2 μm UF membranes cover a pore size range of 0.01 to 0.05 μm (EPA, 2005).

While all the membrane separation processes described above require pressure to drive the process. RO allows water molecules to cross the semipermeable membrane through a combined concentration gradient leaving the dissolved contaminants behind. Osmosis is the process where water passes through a “semipermeable” membrane. The water transport is facilitated by the concentration gradient due to a dilute solution on one side of the membrane and a concentrated solution on the other side. Water naturally wants to flow from the lower concentration to the higher concentration side to reach an

equilibrium. Applying pressure that exceeds the osmotic potential of the concentrated solution on the concentrate side forces water through the membrane to the lower concentrated solution reversing the process of osmosis; hence the name RO which was developed to purify water with dissolved contaminants specifically salt such as sea water (Wijmans and Baker 1995). RO membranes are primarily configured in the spiral wound element (SWE) configuration using a mesh spacer to separate the membrane leaves. The concentration at the liquid-membrane interface and the limitations of the current feed spacer technology play an integral role in the fouling of membranes and the drive for extensive pretreatment.

2.1 Membrane transport

There are many models to describe membrane transport including classics such as the solution-diffusion, pore flow and Nernst–Planck solution-diffusion model. The most commonly accepted model to describe solute and solvent transport through dense non-porous RO membranes is the solution diffusion. Originally developed by Lonsdale et al. (1965), the base assumption was that both solute and solvent dissolve into the surface layer of the membrane from the feed water side and then proceed to diffuse through it independently to the product water side. As can be seen by Figure 2.1 the difference in pressure which produces a chemical gradient across the membrane in the solution diffusion model is depicted as equal across the whole membrane. Each one facilitating its own throughput based on its own individual chemical potential gradient. With permeants having varying rates of membrane diffusivity and diffusion out of the bulk into the membrane itself a separation occurs between the permeants (Wijmans and Baker 1995;

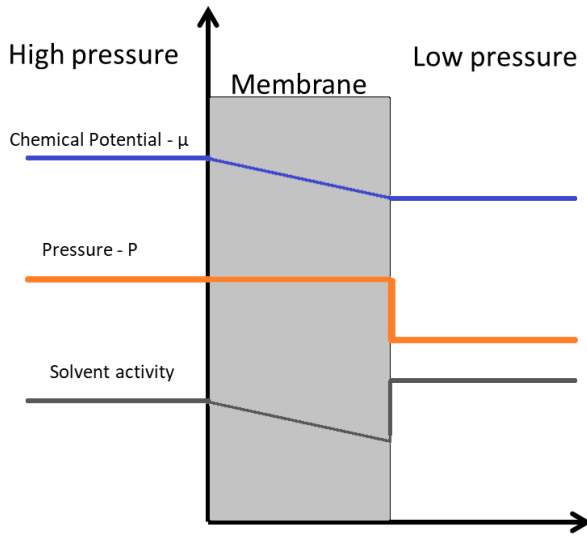


Figure 2.1 Solution-diffusion model – (adapted from Wijmans and Baker 1995)

Wang et al. 2014).

Membrane performance is primarily characterized by flux and rejection. The volumetric water flux (J_w) is derived from Henry's law and Fick's first law of diffusion,

$$J_w = A(\Delta P - \Delta \pi) = \frac{K_w D_w^m}{\Delta x} \frac{V_w}{R_g T} (\Delta P - \Delta \pi) \quad \text{Equation 1}$$

Where A is the water permeability, Δp is the pressure differential and $\Delta \pi$ is the osmotic pressure difference across the membrane, D_{wm} is the water diffusion coefficient of the membrane, K_w is the water-membrane partition coefficient, Δx is the membrane thickness, and V_w is the molar volume of water. The solute transport (J_s) ignores Henry's law and is derived from Fick's law based on the driving force being due to the concentration differences,

$$J_s = J_w C_p = B(C_m - C_p) = \frac{K_s D_s^m}{\Delta x} (C_m - C_p) \quad \text{Equation 2}$$

The observed Rejection can be calculated from the concentration in the product and the concentration in the feed as can be seen in equation 3 (Wang et al. 2014).

$$R_0 = 1 - \frac{c_p}{c_f} \quad \text{Equation 3}$$

2.2 Module configuration

Low-pressure membranes are typically configured as hollow-fiber modules. The majority of these modules are created by taking a bundle of fibers lengthwise and potting the membrane ends into a housing that allows direct or cross-flow filtration. The filtration either works by passing water from the outside of the fiber through the fiber wall and into the lumen or from the lumen to the outside. Operating outside in reduces the potential for blocking the fibers with particulate matter which varies based on the inner diameter of the fiber. Whether direct or tangential filtration, modules are typically backwashed after reaching a specific pressure or flux loss to remove cake formation on the influent side of the membrane and to prevent irreversible fouling from occurring. Certain studies cite the particle fouling layer as a mechanism for enhanced microbial removal and aided rejection. Yet the secondary layer created is highly variable based on the source water being treated and not easy to reproduce (EPA 2005).

The SWE configuration is the module design choice for RO and NF. This format allows for the most active membrane area in the smallest footprint with 400 ft² for an 8 inch by 40 inch standard RO element. Other module designs that have been used like the plate and frame only have half the packing density (Yang et al. 2013). While the transmembrane pressure (TMP) drives the water across the membrane surface overcoming the osmotic potential of the solution there is also a feed channel pressure associated with

SWEs which is the pressure between the inlet feed and the concentrate outlet (Araujo et al. 2012). This configuration utilizes a spacer to separate the membrane leaves and create a channel for feed water to flow. Typical feed spacers consist of a diamond mesh pattern that is woven or extruded and range from 0.33 mm (13 mils) to 2 mm (80 mils) in thickness with a density of 6 to 32 strands per inch. The most common mesh feed spacer used is 0.8636 mm (34 mils). This has been the norm since the inception of this technology providing the benefit of increased mass transfer due to promoting turbulence versus laminar flow. Flux increases have been reported to be three to five times for spacer-filled channels when compared with empty channels (Schwinge et al. 2004).

2.3 Feed spacer technology

Feed spacers for commercial spiral wound RO elements, Figure 2.2 are more complex than a simple classification of a mesh material with a diamond shape. At first

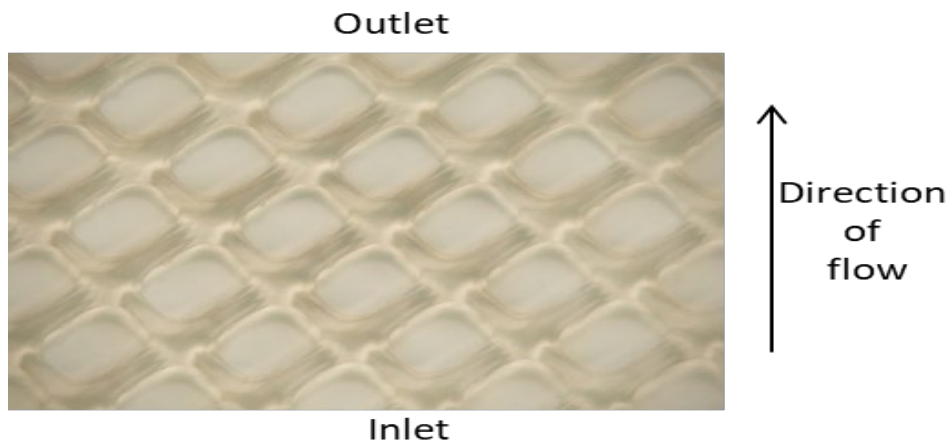


Figure 2.2 Image of a 0.508 mm (20 mil) mesh feed spacer on top of a RO membrane under normal typical operating conditions in a transparent acrylic cross flow cell (Sterlitech; Kent, Washington).

glance one would think it seems pretty simple, water transverses the mesh channel in the path of least resistance and diffuses through the membrane where the spacer does not block flow. With the geometrical characterization and directional orientation of flow identified from previous researchers (Bucs 2013) insight is gained into the potential benefits and pitfalls created by feed spacer selection. First off, not all of the mesh contacts the membrane. The mesh is created by either extruding or laying single strands equal distance apart from each other and overlaying with the same type of strands perpendicular creating a square. The intersection points of these strands called nodes are where the feed spacer contacts the membrane surface. The square feed spacer is turned, inserted between two membrane leaves, and rolled into the SWE configuration; feed flows into the diamond geometry at a predetermined contact angle. Another key feature of the current mesh feed spacers are that most of the filaments do not carry a uniform diameter throughout, there are thinner diameter segments between the nodes. Where the mesh spacer physically rests on the membrane surface low flow zones (dead zones) are created in the feed channel. This is due to laminar flow through the SWE with a typical Reynolds number <300 calculated based on the hydraulic diameter of a square feed channel impinged by the feed spacer geometry (Bucs et al. 2015). These dead zones create opportunity for fouling to setup and proliferate throughout the membrane surface and feed channel. (Suwarno et al. 2012; Piciooreanu et al. 2009; Koutsou et al. 2007; Vrouwenvelder et al. 2006; Vrouwenvelder et al. 2009; Radu et al. 2010)

Extensive modeling using computational fluid dynamics software has been done to gain a better understanding of the impact of feed spacers and the potential for feed spacer

improvements. The primary focus of these efforts were to determine how to improve the hydrodynamics of the feed channel for increased flux or reduced fouling or both. Researchers have modeled modifications such as filament shape, angle of attack and node shape to determine if optimizing these parameters would enhance membrane transport and/or reduced fouling. A rectangular spacer, a cylindrical spacer, and a triangular spacer were modeled to determine potential enhancement in the fluid flow of the feed channel with the triangular configuration providing the best mass transport and lowest pressure drop (Ahmad et al. 2006). This was followed up by Ngene (2010) who modeled an offset circle, star shape, tear drop, and a kite shape as potential node replacement geometries to facilitate improved fluid dynamics and reduced fouling at the points where the feed spacer contacts the membrane surface. The star and circular geometry showed formation of recirculation zones downstream of the structure. The kite and tear shape structures provided a continuous streamline with fluid reconnecting at the back of the geometry. All designs were created using stereolithography on a glass plate channel and showed particulate deposition and biofouling in experiments with no specific reduced fouling.

Another aspect of feed spacer design is the ability to support the separation of the membrane leaves when rolled into a SWE configuration. Strand count density (e.g. count per inch/cm), angle of intersection and thickness of the spacer are all factors that influence the structure and performance of SWE. As SWE are wound tighter the channel thickness decreases and there is a need for more support, a higher strand count density is typically required. Additionally, the packing density impacts the number of contact points per unit area between the mesh feed spacer and membrane, which create more points of flow

disruption at the membrane surface. If eddies and low flow regions form around these points of contact, it is expected that this will impact the likelihood of scale formation. Unfortunately, the amount of contact points and gap distance does not correlate directly to channel stability. Therefore, membrane manufacturer's simply supply enough mechanical support to ensure the spacer region does not collapse when the SWE is constructed. One notable exception to the standard mesh feed spacer design that was commercialized was the use of corrugated feed spacers in the 1980's (Riley and Milstead 1992). One corrugated design with 8 mm intervals was developed for large channel flow by Kurita waste industries of Japan and successfully applied in 40 plants. Another, corrugation design with the ridges running parallel to the direction of flow was developed by Osmonics; however, this design was found to collapse during element rolling and was not used. Overall, there are opportunities to enhance performance of SWE by optimizing feed spacer design based on water quality, but it is important to recognize that this optimization must also consider the structural support these elements provide to the SWE.

2.4 Fouling

Fouling is defined in the Dow Filmtec RO technical manual as the accumulation of foreign materials from feed water on the active membrane surface and/or on the feed spacer to the point of causing operational problems (Solutions 2010). Fouling can mean scaling, colloidal fouling, biological fouling or organic fouling. Colloidal fouling is when particulates or colloidal matter gets trapped within the membrane feed channel or deposits onto the membrane surface or both. Biological fouling is the growth of a biofilm by a diverse microbial community that utilizes extracellular polymeric substances (EPS) to

obstruct removal by flow and cleaners. Organic fouling are compounds such as humic or fulvic substances that adhere to the membrane surface. Scaling is the precipitation and deposition of sparingly soluble salts such as calcium sulfate (Solutions 2010, EPA 2005).

Current mitigation of fouling is best achieved by removing the foulants up front before they become a problem. Filmtec provides information on pretreatment options Table 2.1, depending on what type of foulant or foulants are present. No good predictive model exists to assess fouling potential and determine exactly what type of pretreatment will work for an RO plant based solely on feed water quality. Even determining chemicals

Table 2.1 Summary of pretreatment options (adapted from Solutions 2010).

Pretreatment	Inorganic Scale	Silt Density Index (SDI)	Bacteria	Oxidizers	Organic Matter
Chemical addition (acid, antiscalant, etc.)	■				
Ion Exchange	■				
Change of operational parameters	■				
Coagulation-flocculation		■			■
Microfiltration-ultrafiltration		■			■
Chlorination			■		
Dechlorination				■	
Granular activated carbon				■	■

and dosages to reduce scaling are not straightforward. Pilot plant studies are setup onsite to operate on the source water with the proposed treatment processes identified to ensure all fouling mechanisms have been identified and addressed. Sometimes even multiple pretreatment trains are built and tested to ensure that not only the best treatment process is selected but also the best value is chosen before the actual plant is built (Barger, 1989).

The industry standard for evaluating the water quality before it enters the RO treatment process falls on the silt density index (SDI). This field test for RO feed water

quality was developed by E.I. DuPont de Nemours and Company. The test filters water at a constant pressure, 30 psi through a 0.45 μm filter. The amount of time required to collect the first 500 mls of filtrate is noted along with the time it takes to collect another 500 ml of filtrate after 15 minutes. These two numbers are used to obtain a plugging factor which is divided by the time of the test to obtain a dimensionless SDI value. Most membrane manufactures require a feed water to be maintained at an $\text{SDI} \leq 5$ with a recommendation of an $\text{SDI} < 3$ to minimize fouling. While a reduced SDI value might inhibit fouling, the 0.45 μm filter used works on the size exclusion principle and only rejects particulates above 0.45 μm . The test does not provide a basis for evaluating dissolved organic matter however, which passes through without impacting the SDI and is known to promote fouling such as biofilm development (Walker, 1986). A smaller filter or an additional filtration step of the filtrate water might be provide a better measure of fouling for the SDI test. Membrane plants and manufacturers are still exploring improved analytical tools to assess fouling potential until something is identified SDI will continue to be called out in membrane manufacturers specification sheets.

Researchers have tried to solve the problems associated with fouling in numerous ways such as surface modification of the membrane or new membrane chemistry. Modifying the current thin film composite polyamide RO membrane surface to be resistant to oxidants without impact to its high rejection and flux would be ideal. This would allow membranes to be cleaned with better and cheaper chemicals like chlorine adding another tool to fight foulants such as biofouling. No new membrane chemistry's or surface improvements have been developed to date that achieve the same high rejection and flux

while provide fouling reduction. A surface modification has been created for RO membranes to be cleaned with stronger oxidizers but the coating wears down and additional chemicals have to be applied to recreate the sacrificial surface coating.

The Army's research program has focused on improvements to the RO membrane and element through the reduction in and removal of fouling materials from the surface of the RO membrane. The specific projects were: 1) Development of chlorine-resistant and non-fouling RO membranes 2) Development of improved coagulating agents for water treatment 3) Development of innovative thin-film composite membranes 4) Evaluation of standard RO element feed spacer configuration 5) Development of new RO element feed spacer configuration 6) Development of a new membrane module configuration 7) identification of commercial biocides for RO element storage 8) Evaluation and selection of biocides for ROWPU storage 9) Development of a membrane separation technique using Donnan exclusion (Downing et al. 1994). Industry has followed over the last 24 years to touch on similar research effort and studies without any major changes being incorporated to utilizing RO membranes for desalination. However, manufacturing of RO membranes in the SWE configuration has been optimized and streamlined reducing the cost substantially almost making RO elements a consumable item at least for the military.

Miller, et al. used polydopamine- and polydopamine-g-poly(ethylene glycol) (PEG) to modify the membrane surface. The modified membranes were tested for fouling using the one hour static adhesion test which showed significant decrease in bio-fouling. However, during longer-term biofouling studies in a membrane fouling simulator, the PEG surface modifications did not show reduced biofouling. The results of this work

demonstrate that polydopamine and polydopamine-g-poly(ethylene glycol) coatings do not effectively control biofouling. The result is most likely due to the complex interactions within a natural water source which ultimately reach an equilibrium favoring the source water and dominating the surface properties/conditions of the membrane (Miller et al. 2012). This study also showed the importance of developing the right screening technique to validate biofouling has been prevented or controlled.

Modified feed spacer designs such as the novel spacer design created by Liu et al. using stereolithography to make a repeating micromixer that moves fluid in the bottom and top layer of the feed channel to the middle where both layers are then replaced by fluid from the middle breaking down concentration effects. Experiments showed that when using the same power input, the new spacer increased the mass transfer coefficient by 20%. Unfortunately, to reproduce this design would cost more than the increase in mass transfer warrants (Liu et al. 2013).

Shear induced techniques such as vibrating, ultrasonic, ultrasonic cavitation of bubbles, among other methods have been explored (Yang et al. 2013). Some have found niche markets in membrane treatment primarily specific high solids waste streams. Thus far shear mechanical technology have not been successfully employed for desalination (Feng et al. 2006).

Printing directly on the RO membrane surface was tried as early as 1998 using a 3D Systems ThermoJet process. While printing a feed spacer on the membrane and testing in a cross-flow cell was found feasible the technology at the time was not advanced enough to create a durable printed layer that would survive winding the membrane into a RO

module to even test the performance in a SWE configuration. This technology was also not capable of directly imprinting individual microstructures onto the membrane surface. In fact the thermal inkjet printers modified to perform this task had temperatures ranging between 200-300 °C which typically damaged the membrane compromising the rejection. This flaw steered the technology towards piezoelectric actuated inkjet printing, acoustic, and electrostatic all generating low heat.

Sandia National labs utilized a process they developed called robocasting to apply a continuous chevron geometry as a micromixer on the membrane surface for inducing three-dimensional flow (Ho et al. 2008 and Altman et al. 2010). While their experiments were inconclusive when comparing their modified membrane to a membrane using a regular feed spacer the error was found to be the laboratory biofouling experiments. Their conclusion stated that a series of more controlled experiments with replicates needed to be conducted (Ho et al. 2008 and Altman et al. 2010). The selection of the chevron pattern as a micromixer was not thought to be an issue in their experiments. A modified BioBots 3D printer which has a high resolution will be used to directly print individual micromixers on the membrane surface. The light source for curing was modified from 405 nm to 365 nm so a compatible ink, UV15TK from Master bond can be used. A base chevron design will be utilized as the micromixer minimally reducing the active membrane area impacted, previous researchers modeling work, and the potential for enhanced flow in one direction and cleaning in the reverse.

CHAPTER 3: DIRECT PRINT MICROMIXERS FOR ENHANCED FLUID FLOW

3.1 Introduction

Reverse osmosis (RO) membranes are typically utilized in the spiral wound element (SWE) design. Winding membrane sheets, or leaves, maximizes the amount of active membrane area in a small footprint. This configuration utilizes a spacer to separate the membrane leaves and create a channel for feed water to flow. The most common feed spacers utilized are non-woven, extruded netting in a diamond shaped mesh ranging from 0.33 mm to 2 mm thickness with a density of 6 to 32 strands per inch. The most common thickness used for mesh spacers in the United States is 34/1000 of an inch, commonly referred to as 34 mils (0.8636 mm). The use of non-woven extruded netting has been the norm since the inception of SWE membrane modules. The spacer material keeps the membrane leaves separated and provides an additive benefit of increasing mass transfer by promoting unsteady state flow while in a laminar flow regime, Reynolds number < 300 . Water flux is reported to be three to five times greater for spacer-filled channels compared with empty channels (Schwinge et al. 2004). While beneficial for increased flux, mesh spacers increase the pressure drop and create low-velocity zones where fouling can occur.

Typical diamond lattice spacers have been extensively modeled using computational fluid dynamics to provide a better understanding of mesh spacer hydrodynamics (Bucs et al. 2014; Bucs et al. 2015; Kodym et al. 2011; Piciooreanu et al. 2009; Fimbres-Weihs and Wiley 2010). The thickness of the feed spacer dictates the channel height and therefore the cross-flow velocity. A spacer filled channel has more

complex flow paths than a simple open channel. Thinner feed spacers, with a denser mesh, allow for the element to be rolled tighter, increasing the active membrane area in a SWE (per given diameter). The filament diameter, the mesh length, the angle between the filaments all play a key role in determining water flux and pressure loss (Schwinge et al. 2004). Guillen and Hoek (2009) modeled different shaped filaments such as a circle, square, ellipse and even a tear drop to elucidate the potential benefits of these different geometries on maximizing mass transfer while minimizing the amount of pressure loss. Based on their modeling simulations different feed channel geometries had little impact on mass transfer. Non-circular filament shapes showed reduced pressure loss identifying a potential area for spacer improvement. While improvements can be made to existing mesh feed spacers by changing the shape of the filament or adding an additional filament, thus far, performance benefits have not overcome the cost of changing current manufacturing practice. Commercial feed spacers cost less than \$1.00 per square meter of membrane to manufacture (Sreedhar et al. 20018). However, research continues to be conducted to try to find a solution to overcome the inherent problems associated with feed spacers and find a novel solution that minimizes pressure drop, shear stress, and concentration polarization while increasing mass transfer (Amokrane et al. 2015).

The inherent flaw with mesh spacers are that the filaments create constrictions in the flow path. Not only are there no unimpeded flow paths, closed recirculation zones (eddies) are present and contribute to flow constrictions (Koutsou et al. 2007). These eddy's are created at the filament contact points and have a negative impact on concentration polarization (Amokrane et al. 2015). Unsteady flow with local recirculation

zones have been identified at higher flow velocities (> 0.3 m/s) (Bucs et al. 2015). Common inlet velocities of $0.06 - 0.17$ m/s are found to produce laminar flow with mixing increasing as the inlet velocity increases (Gimmelshtein et al. 2005). Enhanced velocities are considered beneficial as the turbulence disrupts the boundary layer and deposition on the membrane surface, enhancing flux and reducing scale buildup. Eddies have the opposite effect and allow deposition/fouling to occur. This establishes that a balance needs to be achieved where an enhanced zone is created from a factor improvement over the inlet feed velocity but below a feed velocity of 0.3 m/s to ensure non-recirculating zones are not created.

Even with material insert limitations Liu et al. (2013) used stereolithography to make a static mixing spacer design that redirects the flow at the membrane surface into a chimney creating enhanced flow in the middle of the channel. While these mixers provided a higher mass transfer coefficient there was additional pressure drop and cost associated with fabricating this elaborate design (Liu et al. 2013). Xie et al. (2014) modeled and fabricated an optimized sinusoidal spacer channel that showed increased permeate flux. Yet, this also created a high pressure drop and minimal active membrane area per spacer design. Both efforts highlighting the balance that needs to be obtained between increased mass transport and pressure drop.

The only way to create a feed channel that has fluid paths that are primarily unhindered is to integrate features directly on the membrane that can act as pillars to separate the membrane leaves while at the same time minimizing pressure drop and enhancing flux or reducing fouling. Sandia National Laboratories created a novel process

called robocasting which enabled them to deposit a repeating chevron line on the membrane surface with a UV curable epoxy (Masterbond UVTK15) in 2008. Once the epoxy was deposited the membrane coupon was placed into a UV curing oven using an 8 W, 254 nm wavelength UV source. FTIR analysis of the membrane was conducted to verify no significant changes occurred during application or curing of the epoxy. Issues with repeatable biofilm formation during swatch testing were deemed inconclusive (Ho et al. 2008). Sandia continued this work in 2010 but had again had inconclusive results from the metrics being used to measure biofouling (Altman et al. 2010).

Ngene et al. (2010) used computational fluid dynamic (CFD) modeling to evaluate five different individual geometries representing nodes at the intersection points of a mesh spacer. These geometries varied in shape from a star pattern to a circle. CFD modeling results showed channel flow with low velocity profiles between the individual structures. These shapes were created on a glass plate using phase separation micro-molding, requiring a further development step to evaluate the effectiveness of this approach using membranes. Despite this limitation, experiments showed particulate fouling setup at the front of the shapes and biofouling setup with a tail at the end of each structure. The different types of attachment are a well observed phenomenon that biofouling sets up at feed spacer intersections, low flow zones (Ngene, 2010).

Most research efforts to date have focused on creating as much chaotic mixing, turbulence and disruption of the boundary layer to obtain a high mass transfer rate and, reduce scaling and fouling while maintaining a minimal pressure drop primarily using a uniform material such as a mesh spacer. The objective of this work was to use computation

fluid dynamics modeling to enhance an individual microstructure for printing directly on the membrane surface in a pattern that enhances the inlet velocity and maximizes the amount of membrane area exposed to open channel flow at a constant velocity between 0.2 m/s and 0.3 m/s to provide enhanced hydrodynamic conditions. With this focus, one hypothesis was evaluated: 1) Optimized microstructure design and patterning will maximize the area of enhanced velocity (0.2 – 0.3 m/s) and minimize velocities associated with fouling (<0.1 m/s, >0.3 m/s).

3.2 Material and Methods

3.2.1 Model development and parameters

COMSOL Multiphysics 5.0 (COMSOL Inc., Burlington, MA) was used to model the fluid flow channel with different microstructure geometries and patterning in 2D to enhance the fluid flow regime in the channel. Velocities, specific ranges of interest were defined based on creating zones that reduce fouling and provide an enhancement from the inlet feed velocity of 0.104 m/s. The inlet feed velocity was selected based on defined modeling inputs from other researchers and that it fell within the middle of the typical inlet velocity used by industry (Ngene et al. 2010). The velocity ranges in the channel were broken into four categories 1) 0.0-0.1 m/s, no/low flow zone 2) 0.1-0.2 m/s, unimproved zone 3) 0.2 -0.3 m/s, enhanced zone and 4) greater than 0.3 m/s, non-recirculating zone.

The no/low flow zone from 0.0-0.1 m/s was based on the focus of the micromixer providing an improved fluid flow in the channel. Velocities developed after the inlet feed velocity that are in this range support that the spacer created feed channel is actually hindering the flow and reducing the mixing and fouling disruption. Especially, when the

velocity decreases to zero or close to which has been shown repeatedly in literature as where fouling starts and named appropriately as “dead zones” establishing these upper and lower limits for this range.

While the unimproved zone from 0.1-0.2 m/s provides flow through the channel and does not create a fouling zone. At the same time it does not provide an improvement factor over the original inlet feed velocity or enhance the hydrodynamics of the feed channel thus contributing to mass transfer and reduced fouling. Showing a factor improvement will be critical when attempting to replace typical low cost mesh feed spacers. As previously stated typical inlet feed velocities can range up to 1.7 m/s and have been modeled to show laminar flow with no improved mixing.

Anything greater than 0.3 m/s has the potential to create eddies and is classified in the non-recirculating zone. Recirculation eddies have also been noted to contribute to flow constriction and localized wall shear stress maxima (Koutsou et al. 2007). These zones have the potential even with surrounding higher velocity regions to entrain foulants and become a fouling issue.

In summary, with inlet velocities for SWEs between 0.06 – 0.17 m/s (Gimmelshtein et al. 2005) a 0.104 m/s inlet feed velocity was chosen for modeling. Research has shown flow zones with eddy formations created at filament contact points (Amokrane et al. 2015). Fouling correlated with dead zones of low flow and mixing (Ho et al. 2008) 0 to 0.1 m/s established as a no/low flow zone (or dead zone). Mass transfer was shown to be enhanced by the increased transverse flow velocity (Schwinge et al. 2004) so 0.1 – 0.2 m/s was defined as an unimproved zone. Flow velocities > 0.3 m/s produced unsteady flow with

eddy's identified (Bucs et al. 2015) > 0.3 m/s is non-recirculating zone also with the potential to foul. The goal of this work was to create enhanced flow conditions (0.2 – 0.3 m/s) while minimizing potential fouling flow conditions.

3.2.2 Geometry Enhancement

The chevron geometry and pattern as seen in Figure 3.1 will be utilized as the base micromixer design established from previous researchers modeling work, minimally reducing the active membrane area impacted by printing, and the potential for enhanced flow in one direction and cleaning in the reverse. Additional background and explanation was provided in the chapter 2. The variables chosen were comparable to typical parameters associated with feed spacer design such as the flow attack angle, distance between spacer filaments, filament diameter and filament length. The typical gap distance for mesh spacers varies from 2.4 mm to 2.8 mm with membrane contact points varying from 0.28 mm to 0.98 mm for mesh feed spacers as described by Bucs et al. (2013). While the enhanced base design that was selected for evaluation has a distance of approximately 4 mm and contact points of 3 mm. If the 1.2 mm difference from a typical gap width of 2.8 mm for mesh spacers is found to impact structural integrity of a spiral wound element a post or other feature enhancement to minimize this gap will be evaluated.

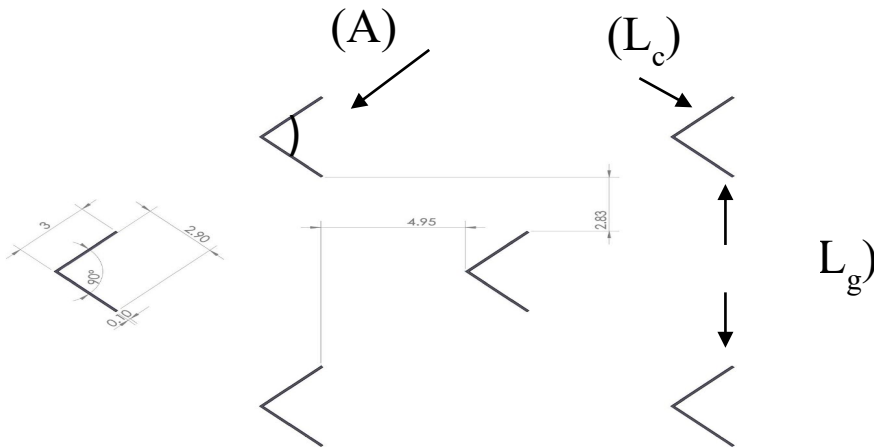


Figure 3.1 The base micromixer design was A = 90 degree chevron, offset pattern, $L_c = 3$ mm chevron lengths, width of chevron (W) = 0.01 mm, $L_g = 5.75$ mm gap.

Different models with varying chevron angle, pattern, distance between features, and length were created for analysis. The channel was modeled with a maximum of seventeen chevrons when using the offset pattern and minimum of nine chevrons when using the continuous pattern to ensure the fluid flow profile being examined was a true representation of the impact of a repeating pattern or geometry variation and not impacted by the boundary conditions of the side walls. The area examined for interpolation of the velocity profile included the centered chevron slicing through the surrounding area to establish a unit area of quantification that does not show any repeating flow. This was to ensure the velocity profile could be compared for the different geometries.

3.2.3 Simulation conditions

The Navier-Stokes and continuity equations assuming Newtonian incompressible fluid was used for the flow,

$$\rho u * \nabla u + \nabla p = \eta \nabla^2 u \quad \text{Equation 1}$$

$$\nabla u = 0 \quad \text{Equation 2}$$

(ρ is density (kg/m^3), u is the velocity vector (m/s), η the viscosity (Ns/m) and p is pressure (Pa)).

The boundary conditions that were applied were the left channel wall as the inlet with the inlet flow velocity and pressure were defined. The right channel wall was the exit with the outlet pressure set to the inlet pressure. The remaining structure walls are all set to no slip wall boundaries.

3.2.4 Image analysis software

For each variable that was modeled a velocity profile was generated. Each image was edited using a graphic art program to crop the image down to the representative unit area of quantification for imaging and inputted into ImageJ (Rasband 2018). The image was then converted to an 8 bit image followed by manually adjusting the threshold color to ensure when it was converted to a binary image it captured all of the velocity coverage shown in the color image. The pixels present along with the percent coverage of the velocity profile covering the representative feed channel for each zone was identified along with a base pattern to allow subtraction of the background chevrons. The full velocity range was also imaged and analyzed and used as a comparison to ensure not velocity ranges were missed.

3.2.5 Materials

Commercial flat sheet RO membranes (Dow Filmtec SW30XLE; Midland, MI) were used in this study. The flux range specified by the manufacturer was 23-29/800 (gallons per square foot of membrane per day)/psi with a NaCl rejection of 99.5%. All membranes were stored as packaged from shipping until ready for use. A UV curable

epoxy (Masterbond UV15TK; Hackensack, NJ) was used for printing features on membrane. Solutions were prepared using de-ionized water and sodium chloride (Reagent Plus NaCl >99.0%) purchased from Sigma Aldrich (St. Louis, MO). Fluorescent dragon green 1.9 μm in diameter styrene beads were purchased from Bangs Laboratories (Fishers, IN) and refrigerated until ready for use.

3.2.6 Printer

A 3D printer from BioBots, BioBots 1 (Philadelphia, PA) was modified by the manufacturer per requested specifications to print a stabilized micromixer directly on the surface of a membrane without needing any additional processing steps. This included an enhanced print head with one, UV 365 nm LED light and a larger print platform to be able to print the active membrane area utilized by the cell.

3.2.7 Printing of micromixers on membrane

An enhanced chevron and pattern based on the CFD modeling was selected to be the micromixer design to be printed on the thin film composite polyamide reverse osmosis membrane. A Solidworks (Dassault Systèmes, Vélizy-Villacoublay, France) drawing was generated fitting within the pattern in the dimensions of the Sterlitech crossflow cell feed channel. The STL file was uploaded to the BioBots print platform where it was prepared for the printer using slicing software. The UV curable epoxy, UV15TK was poured into the syringe to the 5 ml mark. A needle was screwed onto the syringe and inserted into the metal cylinder for printing. The pressure was set at 30 psi based on previous reports, manufacturer recommendations, and experimental results to the viscosity of the epoxy to make sure the epoxy came out at the correct flow for optimal deposition and curing on the

membrane. The epoxy and static curing process were previously verified through FTIR analysis to not cause any significant chemical changes in the membrane. (Altman et al. 2010)

3.2.8 Low pressure transparent membrane cross flow cell system

The test apparatus used was a low pressure acrylic cross flow cell with an effective membrane surface area of 140 cm² purchased from Sterlitech. The cell channel depth was 0.8636 mm (34 mil) so acrylic shims were used to achieve the 0.508 mm (20 mil) feed channel height of the printed feed spacer and low foulant feed spacer. The volume of the polypropylene feed tank was 16 liters. A high pressure pump with a variable frequency drive (Hydra-Cell model F20K52GSNEM, Wanner Engineering, Minneapolis, MN) was used to pump the feed solution at 0.5 liter per minute to the crossflow cell and to set a constant feed flow velocity. A backpressure reducing valve (Model BPH05-02T, Straval, Elmwood Park, NJ) to allow for constant stabilized pressure from start to finish of each run was utilized. An injection syringe was plumbed at the inlet of the high pressure pump to inject the fluorescent beads.

3.2.9 Membrane Performance Testing Membrane characterization

Membranes were stored in a glass beaker fully submerged in deionized water for one hour prior to being inserted into the crossflow cell. Two acrylic shims were placed in the feed channel to reduce the thickness of the feed channel to 0.508 mm for all experiments. Membrane experiments were conducted in a small plate-and-frame rectangular crossflow laboratory acrylic test cell. Flowrate to the cell was controlled by a variable frequency drive set to maintain a feed flow of 0.5 LPM. Pressure was adjusted to

20.7 bar for the entirety of the test. Membranes were run for 24 hours with distilled water at 20.7 bar to ensure compaction and stabilization. Once the flux was determined to be constant fluorescent dragon green 1.9 μm in diameter styrene beads were injected into a recirculating loop for the crossflow cell. The cell was placed under a Nikon SMZ-18 stereo fluorescence microscope (Nikon Melville, NY) to take time lapse pictures and video to determine fluid flow velocity profile using the fluorescent beads to verify fluid flow modeling profile.

3.3. Results

3.3.1 Pressure profile

The primary concern with varying different feed channel characteristics or implementing a new feed channel design is that it will induce pressure drop that is too high to be of practical use. This was shown to be a problem in the static mixing spacer design by Liu et al. (2013) and other 3D mixer designs by researchers. CFD modeling of chevron micromixers developed for this study did not show significant pressure drop across the unit area of quantification. Figure 3.2 provides an example of the pressure drop observed for the optimal design which is described in more detail later.

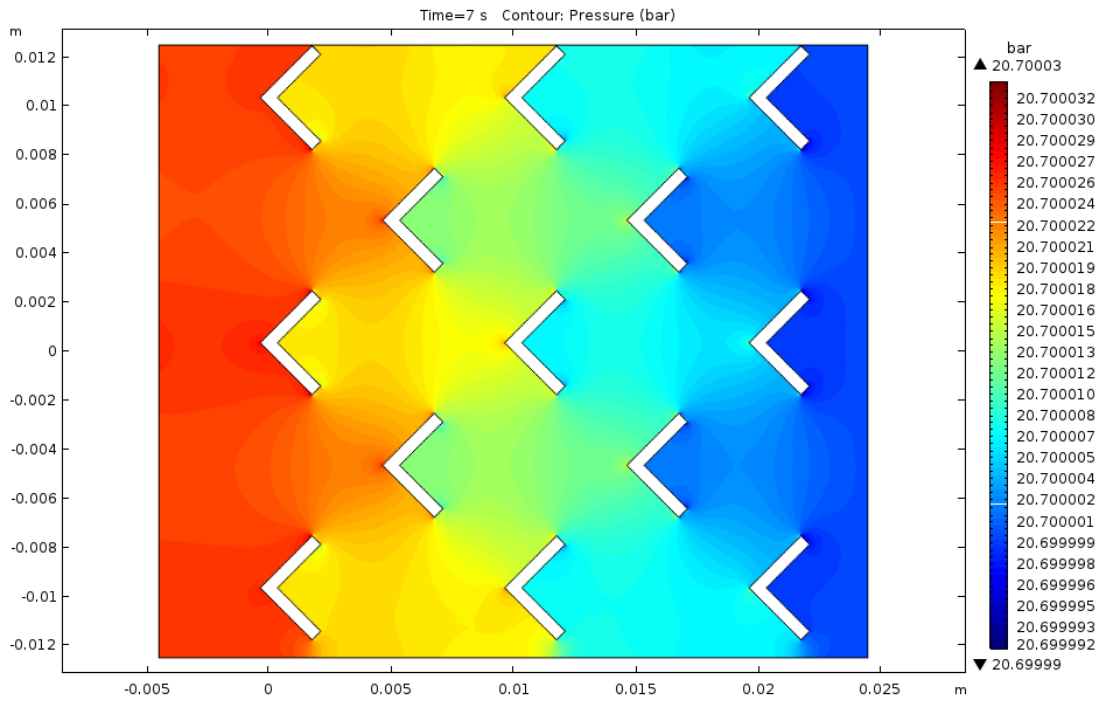


Figure 3.2 Pressure profile for 90 degree chevrons with an offset base design pattern that included a 3 mm chevron length and 5.75 mm gap length. An inlet velocity of 0.104 m/s and a specified outlet pressure of 20.7 bar.

3.3.2 Image analysis of velocity profiles

The main focus of the COMSOL modeling was the velocity profile generated based on inputted parameters. While this was informative, to determine the percent coverage in the defined feed channel for each velocity region of interest a comparable unit area of quantification was selected. As shown in Figure 3.3 the velocity profile for the 90 degree angle exhibits low velocity regions (dark blue) around the outer edge of the model due to no slip boundary conditions. While these regions will occur in the SWEs they are very small and not the representative section that details the influence of the variables selected. The unit area of quantification outlined with the dotted line in Figure 3.3A, B captures the

non-repeating segment of velocity around the centered most chevron with equal segments boxed off around it. This is representative of a unit area of quantification influenced by the specific variable in front, behind, and on the sides in the fully developed model. The extraction of the unit area of quantification shown in Figure 3.3B followed by the transformation in to the binary image Figure 3.3C allows the percent coverage to be calculated for comparison purposes using the ImageJ software.

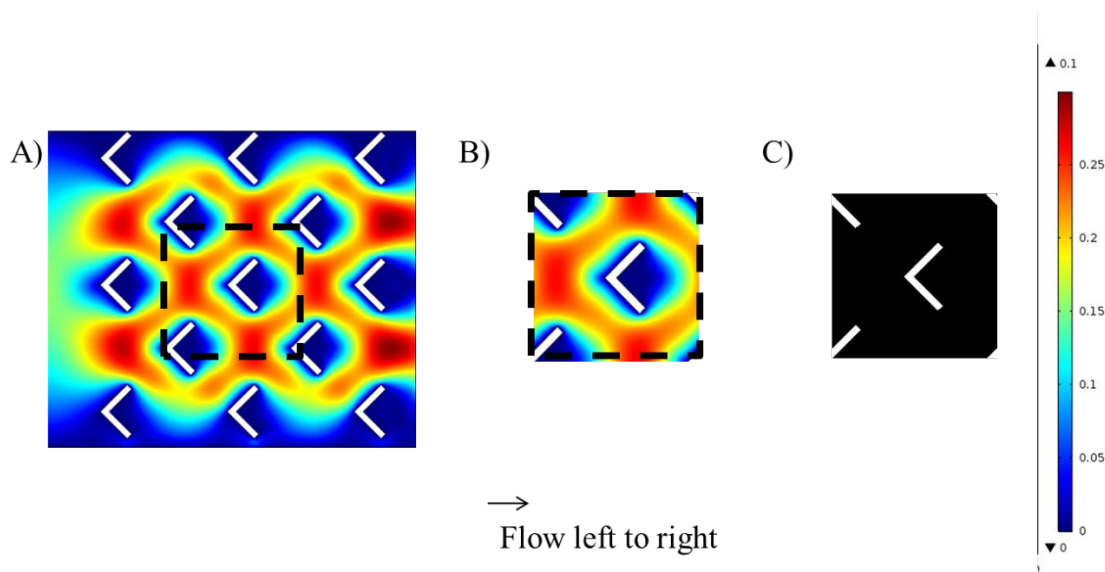


Figure 3.3 Full velocity profile from 0 to 0.3 m/s for the 90 degree angle. To quantify flow regimes, A) an area of quantification was identified from a larger modeling area to ensure boundary conditions did not impact velocity profiles, B) the unit area of quantification was extracted, and C) the image of the unit area of quantification was transformed into a binary image for analysis to determine the amount of area with a given flow condition.

To quantify the percent coverage for each range the velocity minimum and maximum were set in COMSOL to show only the color profile for the specific velocity ranges of interest. From this image (jpeg) a unit area of quantification was identified (Figure 3.3A) and an image was cut out for further analysis (Figure 3.3B). Each area of quantification was then converted to a binary image (Figure 3.3C) and analyzed in ImageJ to calculate the percent membrane area covered by a given velocity range. The percent area that was calculated for the 0 m/s image (the chevron lines) was then subtracted from all the other percent areas images as background to determine the actual coverage for each velocity range. The quantification of flow velocities for the 90-degree chevron offset pattern are presented in Table 3.1. The percent coverage was calculated for each range as shown in Table 3.1 and the summation provide in 3.2C, the percent area covered by individual flow regimes. The sum of all the flow regimes (0-0.1 m/s, 0.1-0.2 m/s, 0.2-0.3 m/s, and >0.3 m/s) for all geometries and patterns tested were then compared to the percent coverage for the image with all the velocities ranges present (0 – 0.5 m/s). Results of this error analysis are presented in Table 3.2. Column A, the percent area due to the chevron represents the amount of space that the chevrons themselves take up in the unit area of quantification. This background was subtracted from one-hundred percent to show the percent available space for fluid flow, where the velocity profile will develop. COMSOL was used to generate a full velocity profile that was analyzed with ImageJ to determine the percent area covered by 0.0 to 0.5 m/s, column B. Adding the percent area due to the chevron (column A) to the area covered by flow (column B) equals 100%. The percent error was calculated by subtracting

column C from column B then dividing by column B and multiplying by one-hundred. This small error is associated with splitting the velocity profiles and conversion to the binary image. This allowed a full comparison regardless of the amount of coverage generated by the change in geometry or pattern. The error associated with the image analysis was less than 4% in all cases.

Table 3.1 Breakdown showing how the percent area was calculated for the 90 degree angle.

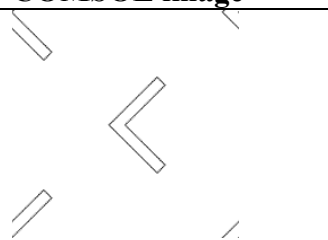
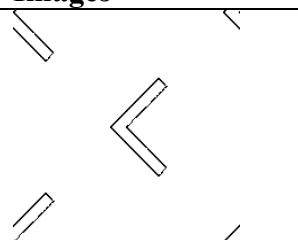


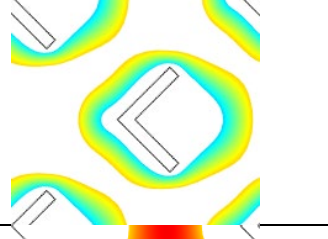

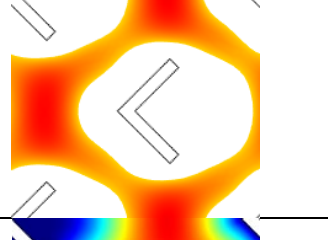

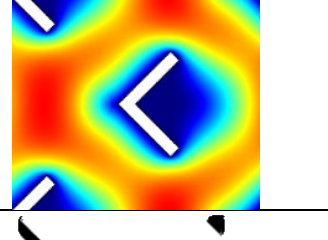


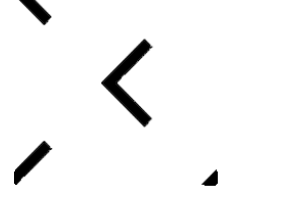
Range	COMSOL image	ImageJ	% Area	Pixel
No flow			1.6	232
0-0.1 m/s			$23.5 - 1.6 =$ 21.9	$9455 - 232 =$ 9223
0.1-0.2 m/s			$32.8 - 1.6 =$ 31.2	$13394 -$ $232 =$ 13162
0.2-0.3 m/s			$40.8 - 1.6 =$ 39.2	$16491 -$ $232 =$ 16259
All velocities			$95.4 - 1.6 =$ 93.7	$38332 -$ $232 =$ 38100
Chevron only			6.3	2159

Table 3.2 Breakdown to show how the percent coverage for the ten models were calculated. The optimal design is highlighted in green.

	Percent area due to chevron	Percent area covered by 0.0 - 0.5 m/s	Percent area covered by individual flow regimes	Image processing percent error
	A	B	C	D
60 degree offset	6.1	93.9	91.5	2.6
90 degree offset	6.3	93.7	92.3	1.5
120 degree offset	5.3	94.7	93.1	1.7
60 degree continuous	1.7	98.3	98.2	0.2
90 degree continuous	2.3	97.7	97.2	0.5
120 degree continuous	1.8	98.2	98.7	-0.5
Gap 0.75 mm	13.5	86.5	83.0	4.0
Gap 10.75 mm	3.6	96.4	94.0	2.5
4 mm length	5.2	94.8	91.5	3.5
5mm length	6.7	93.3	91.9	1.5

Note. Maximum velocity generated was 0.5 m/s

3.3.3 Effect of micromixer design on velocity profiles

A design of experiments analysis was conducted to down select to the improved dimensioned individual chevron and pattern to create the feed channel with the greatest enhanced zone, 0.2 m/s to 0.3 m/s. The optimal condition was identified as the highest percent active membrane area covered by the enhanced zone. The maximum velocity color range was set to 0.3 m/s to allow for a direct comparison of velocities gradients by color. Three different angles: 60, 90, and 120 were evaluated using the same base chevron design shown and described in Figure 3.1.

Figure 3.4, shows the repeating chevron pattern with the different angles modeled along with the impact of the boundary effects from the side walls. To be able to compare each variable modeled and have a representative quantified percent coverage, a dashed frame of the centered chevron with boundaries to half of the surrounding chevrons was established as stated in section 3.2.2.

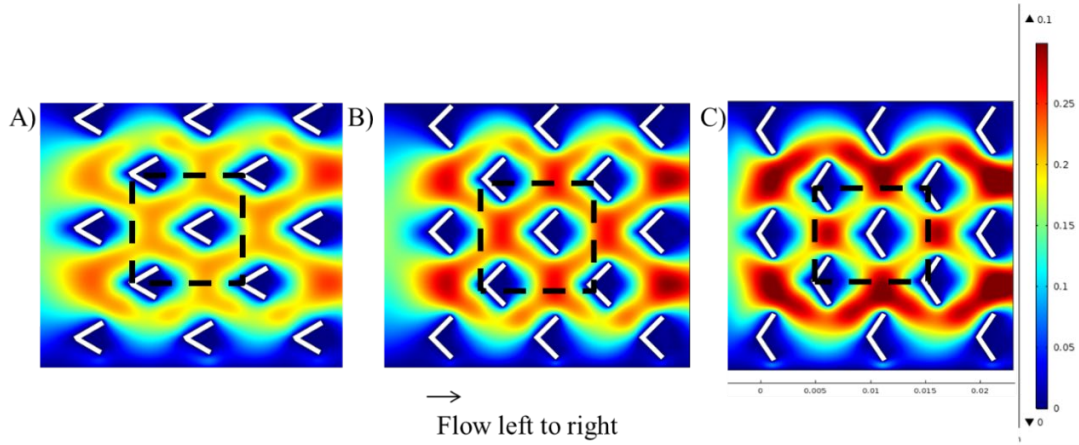


Figure 3.4 Full velocity profile from 0 to 0.3 m/s showing influence of angle: A) 60 degree angle B) 90 degree angle C) 120 degree angle on the amount of open channel flow and velocity regions with the base design pattern: offset, 3 mm chevron length, and 5.75 mm gap inlet velocity of 0.104 m/s.

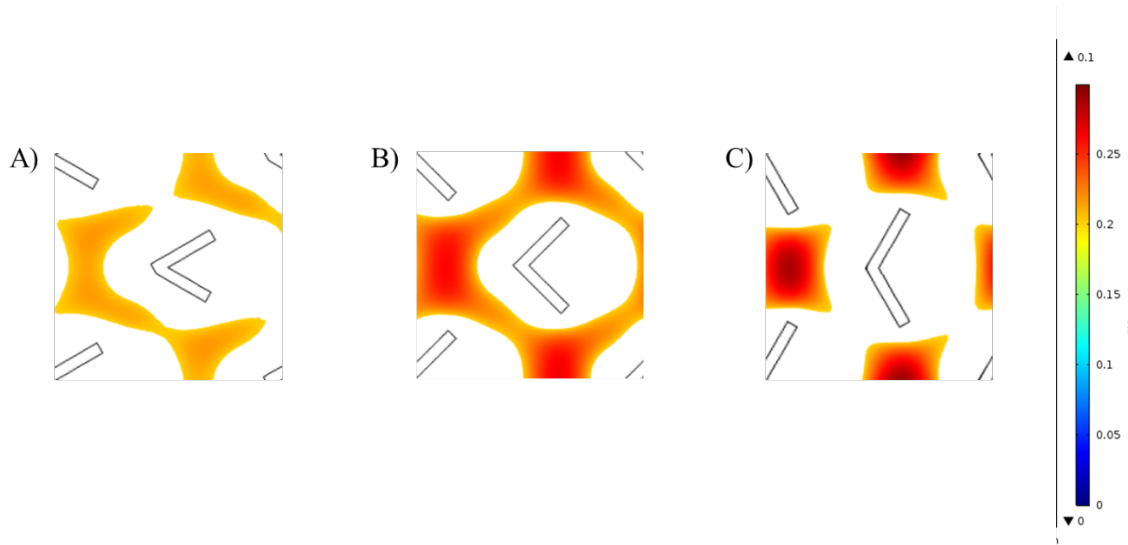


Figure 3.5 Percent feed channel coverage for the enhanced zone, 0.2 to 0.3 m/s velocity profile for different angles modeled: A) 60 degree angle – 25.6% B) 90 degree angle –

39.2% C) 120 degree angle – 25.4%. The 90 degree geometry showed maximum coverage of enhanced flow conditions.

This created a velocity profile distribution based on percent coverage as can be seen in Figure 3.6. The 60 degree and the 120 degree angle had the lowest coverage for the 0.2 to 0.3 m/s velocity range, 25.6% and 25.4%. The 90 degree angle had the highest coverage for the enhanced range at 39.2%. All three velocity profiles created an enhanced zone of continuous fluid flow in the channels not near the chevrons themselves. The area around the chevrons experienced the lowest velocity range, 0 to 0.1 m/s with membrane coverage of 21.9% for the 90 degree chevron and 19.2% and 26.0% coverage respectively for the 60 degree and 120 degree variant. This low flow and zero velocity distribution developed primarily behind each micromixer for all three models. The 0.1 to 0.2 m/s range for all three angles were also similar for all three models and no velocities zones developed over 0.3 m/s. Based on the 90 degree angle having the highest enhanced velocity and the lowest no/low flow coverage this geometry feature was selected to carry through to compare against the next variable modeled.

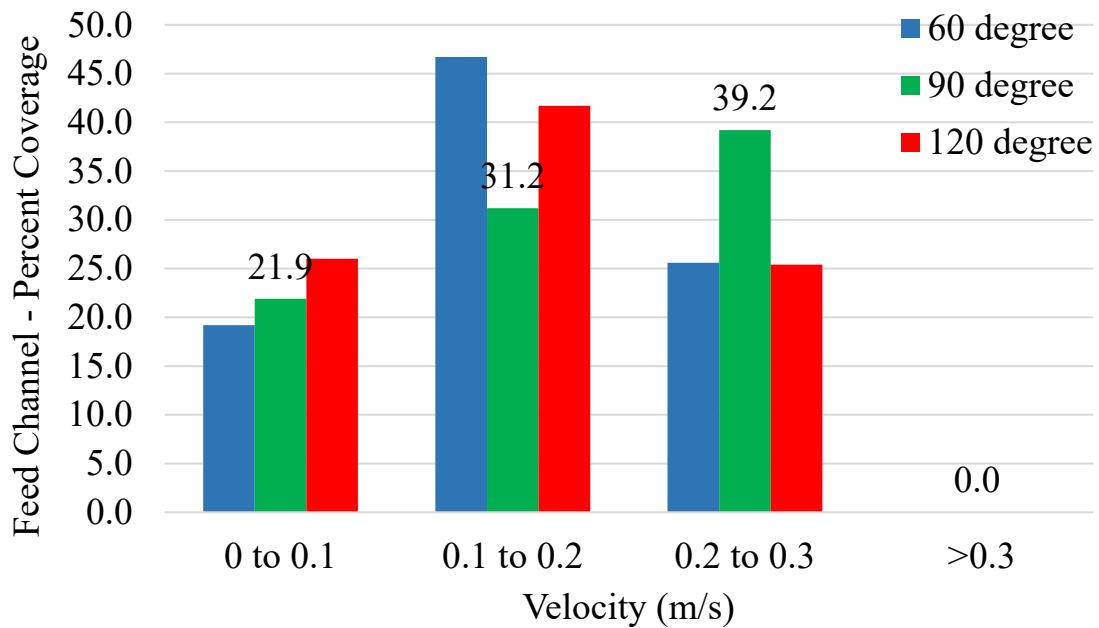


Figure 3.6 The different velocity zones compared for each angle modeled using the base design base pattern: offset, 3 mm chevron length, and 5.75 mm gap. The 90 degree geometry provides the optimal conditions across all flow velocity ranges with 39.2 in the enhanced region. (Note: areas presented do not include 6.3% due to chevron and 1.5% image processing error)

To determine if there was a benefit of an offset pattern versus a continuous repeating pattern. The same angles: 60 degree, 90 degree, and 120 degree using the same base chevron geometry of 3 mm length, 0.1 mm width, and 5.75 mm gap were evaluated using a continuous pattern. This variable change impact on the enhanced velocity profile can be seen in Figure 3.7, a reduced velocity in the enhanced zone for the 90 degree and 60 degree down to 24.0% and 15.3% with an approximate 5% increase for the 120 degree angle to 29.6% coverage. This velocity region also shifted to primarily above and below the

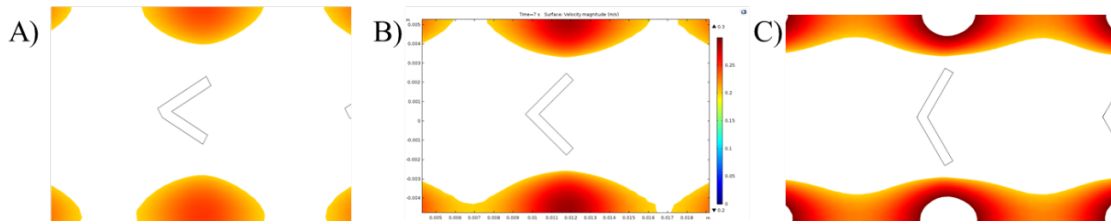


Figure 3.7 The percent feed channel coverage for the enhanced zone, 0.2 to 0.3 m/s velocity profile for the continuous pattern: A) 60 degree angle – 15.3% B) 90 degree angle – 24.0% C) 120 degree angle – 29.6%. The continuous pattern decreases the area of enhanced flow conditions compared to the offset pattern.

chevrons as can be seen in Figure 3.8. Examining all the velocity zones in Figure 3.8, a significant increase in membrane coverage for the 0 to 0.1 m/s range for all three angles modeled was observed with the 60 degree angle increasing to 31.9%, the 90 degree angle increasing to 37.7%, and the 120 degree angle increasing to 38.9%. As can be seen

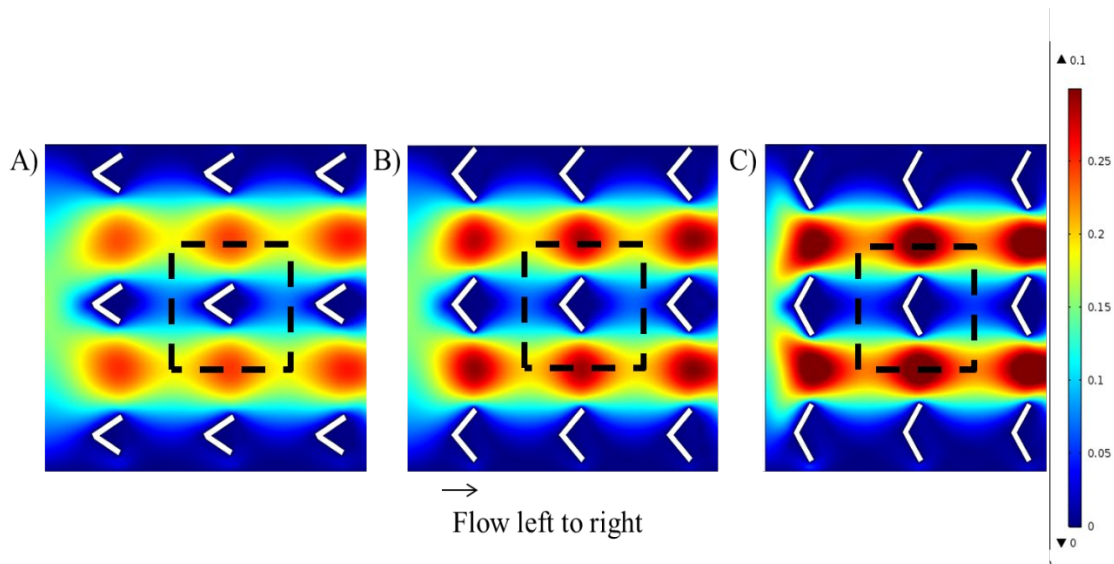


Figure 3.8. Full velocity profile from 0 to 0.3 m/s showing influence of continuous pattern for different angles: A) 60 degree angle B) 90 degree angle C) 120 degree angle on the

amount of open channel flow and velocity regions with the base design pattern: offset, 3 mm chevron length, and 5.75 mm gap inlet velocity of 0.104 m/s. The continuous pattern created channeling that increases percent coverage in the low velocity zone for all angles modeled.

in Figure 3.8, the velocity profile for this range extended in front and behind each chevron.

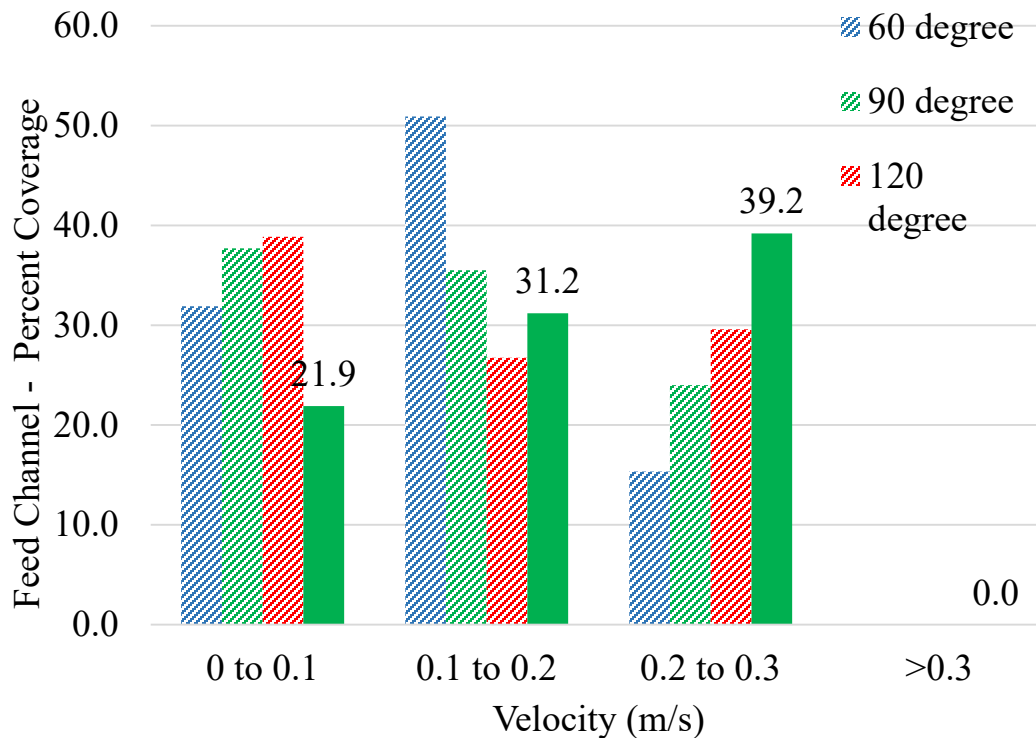


Figure 3.9 The different velocity zones compared for each angle modeled in a continuous pattern using the base design base pattern: offset, 3 mm chevron length, and 5.75 mm gap. The 90 degree offset geometry provided the optimal conditions across all flow velocities with 39.2 percent coverage in the enhanced region. (Note: areas presented do not include 6.3% due to chevron and 1.5% image processing error)

Based on the modeling of the angle and patterning the next variation evaluated was the distance between the chevrons (the gap length) from the base model: 3 mm in length, 0.1 mm thickness, a 90 degree angle in an offset pattern with a gap of 5.75 mm. The additional two distances were 0.75 mm and 10.75 mm to determine if there was any benefit to increasing or reducing flow restriction for creating a higher percent enhanced zone and low fouling zones. The variations in the feed channel velocity profiles for these three gap distances can visual be compared in Figure 3.10. The 0.75 mm gap developed a 9.1%

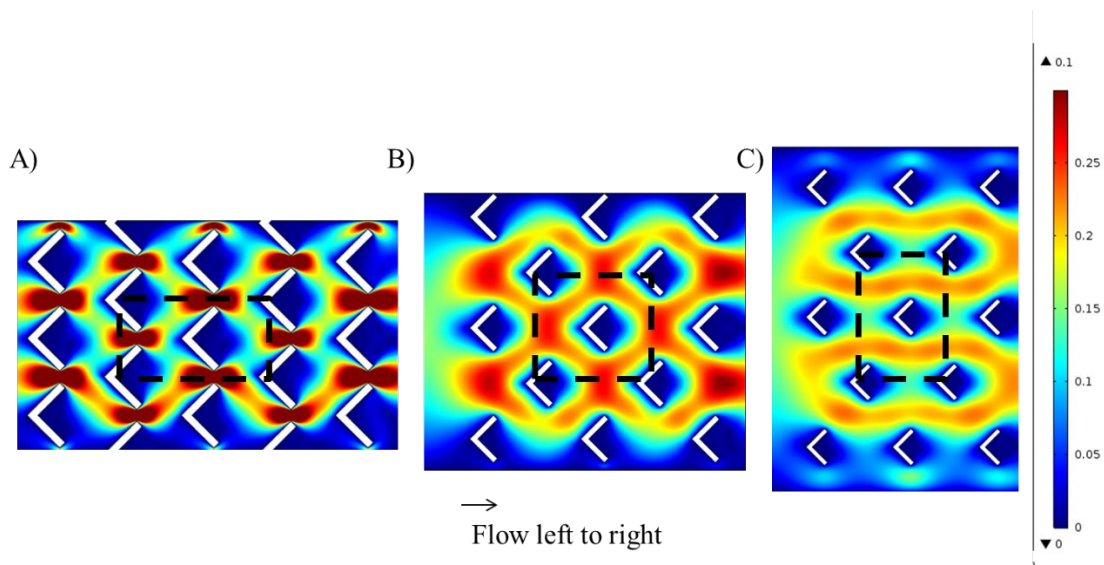


Figure 3.10 Full velocity profile from 0 to 0.3 m/s showing influence of different gap lengths: A) 0.75 mm B) 5.75 mm C) 10.75 mm on the amount of open channel flow and velocity regions with the base design pattern: offset, 3 mm chevron length, and 5.75 mm gap inlet velocity of 0.104 m/s. The micromixer gap length impacted the amount of channeling and high velocity spiking between micromixers.

velocity profile in the 0.3 m/s region, non-recirculating zone, Figure 3.12 not previously seen in this study. The 0.75 mm gap model also showed an increase in the 0 to 0.1 m/s range to 33.4%, both fouling zones and a similar profile in the 0.1 to 0.2 m/s range 31.0%

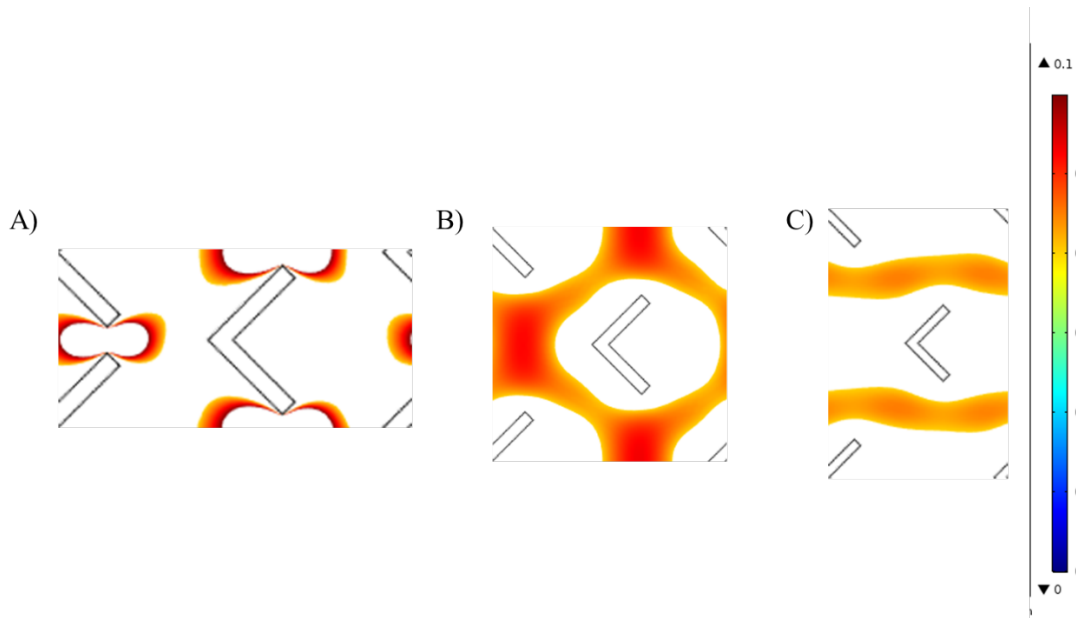


Figure 3.11 The percent feed channel coverage for the enhanced zone, 0.2 to 0.3 m/s velocity profile for different gap lengths: A) 0.75 mm – 9.5% B) 5.75 mm – 39.2% C) 10.75 mm – 25.2%. The 5.75mm gap length provides the highest flow coverage in the enhanced zone.

coverage and only 9.5% coverage in the enhanced zone, 0.2 to 0.3 m/s range, Figure 3.12. The model with the increased gap size of 10.75 had similar membrane coverage in the 0 to 0.1 m/s range, 21.1% coverage and 47.7% coverage of the 0.1 to 0.2 range. For this model there was no velocity profile generated in the greater than 0.3 m/s range and the enhanced zone membrane coverage was reduced to 25.2%.

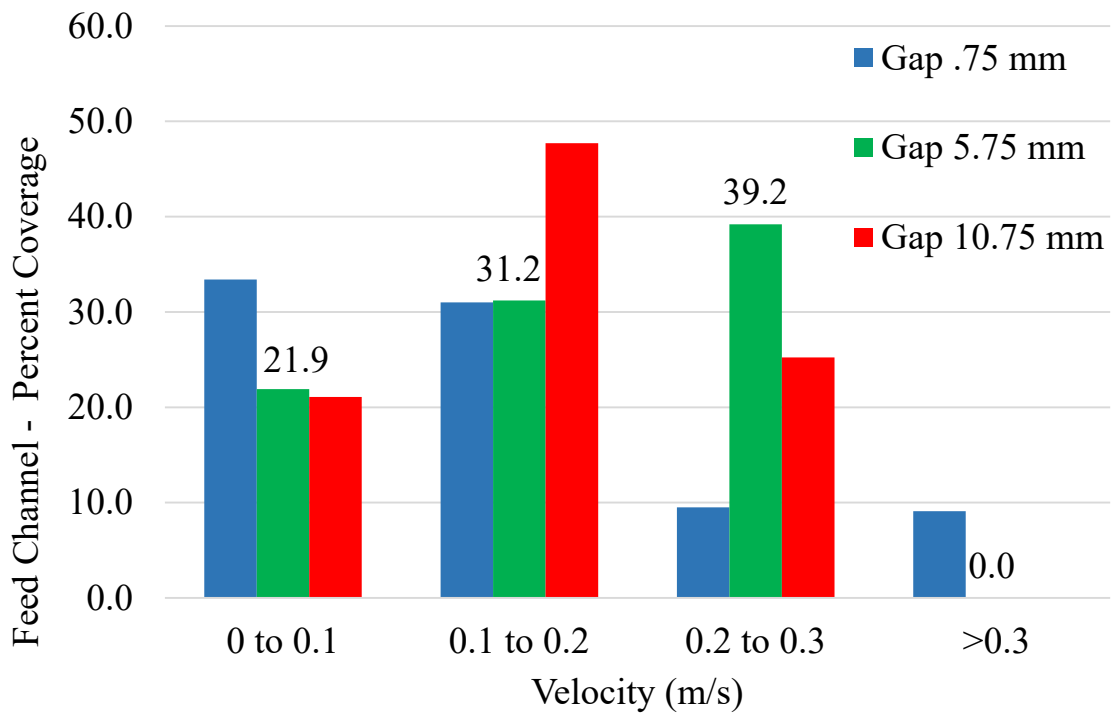


Figure 3.12. The different velocity zones compared for each gap length modeled using the base design pattern: offset, 3 mm chevron length, and 5.75 mm gap. The 90 degree offset geometry provided the optimal conditions across all flow velocities with 39.2 in the enhanced region. (Note: areas presented do not include 6.3% due to chevron and 1.5% image processing error)

To determine if there was any benefit to an increased length the chevron length was varied from the base, 3 mm to 4 mm and 5 mm all using the same characteristics of a 0.1mm thickness, 90 degree angle in an offset pattern with a 5.75mm gap. The velocity profile variations caused by altering this dimension can be seen in Figure 3.10. Both

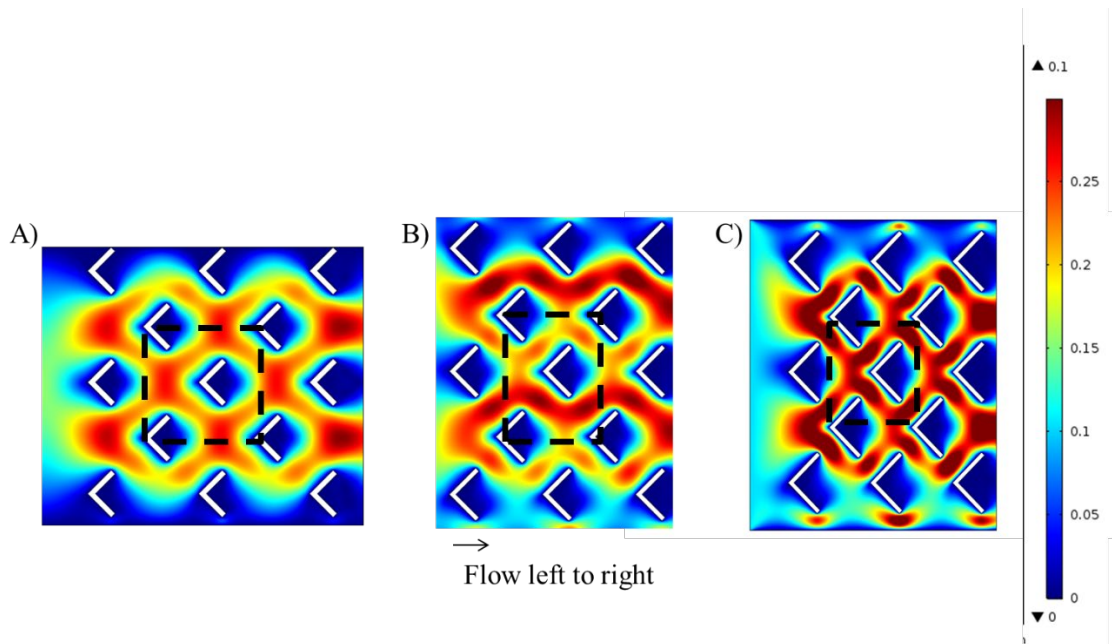


Figure 3.13 Full velocity profile from 0 to 0.3 m/s showing influence of different chevron lengths: A)3 mm B)4 mm C)5 mm on the amount of open channel flow and velocity regions with the base design pattern: offset, 3 mm chevron length, and 5.75 mm gap inlet velocity of 0.104 m/s. As the chevron length increases, the velocity profile through the channel increases.

changes showed a shift in the velocity profile in the greater than 0.3 m/s range from zero coverage for the 3 mm to 4.0% coverage for the 4 mm and 23.6% coverage for the 5 mm. The enhanced zone was similar for the 4 mm variation with 35.7% coverage while the 5 mm length dropped to 24.3% coverage, Figure 3.14. Both the 4 mm and 5 mm models

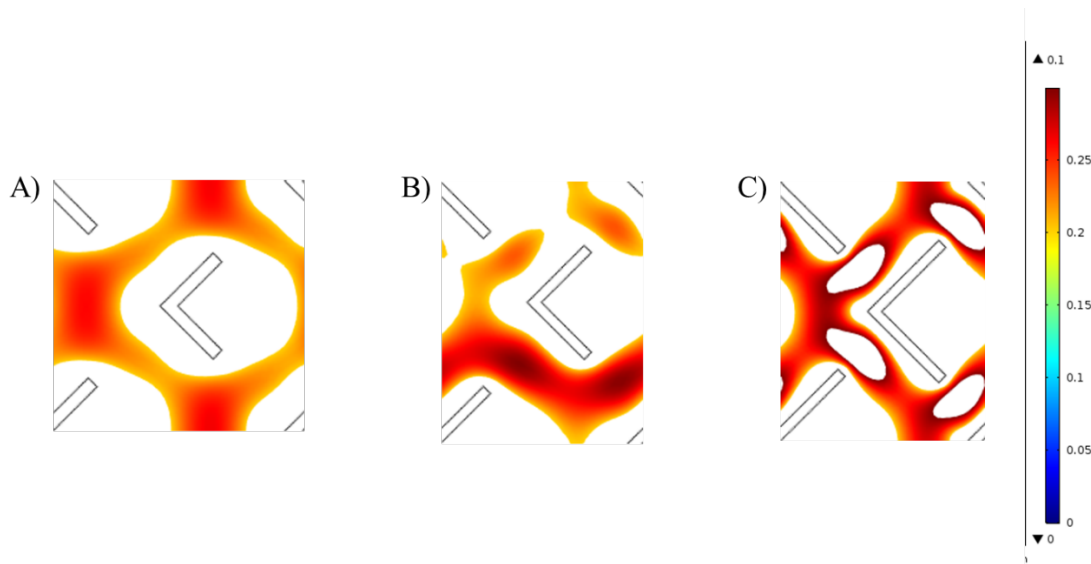


Figure 3.14 The percent feed channel coverage for the enhanced zone, 0.2 to 0.3 m/s velocity profile for different chevron lengths: A) 3 mm – 39.2% B) 4 mm – 35.7% C) 5 mm – 24.3%. The 5.75mm gap length provides the highest flow coverage in the enhanced zone.

reduced coverage in the 0 to 0.1 m/s range to 24.2% and 25.8%, Figure 3.15. While an increase in coverage in the unimproved zone to 27.6% for the 4 mm and 18.2% for the 5 mm models.

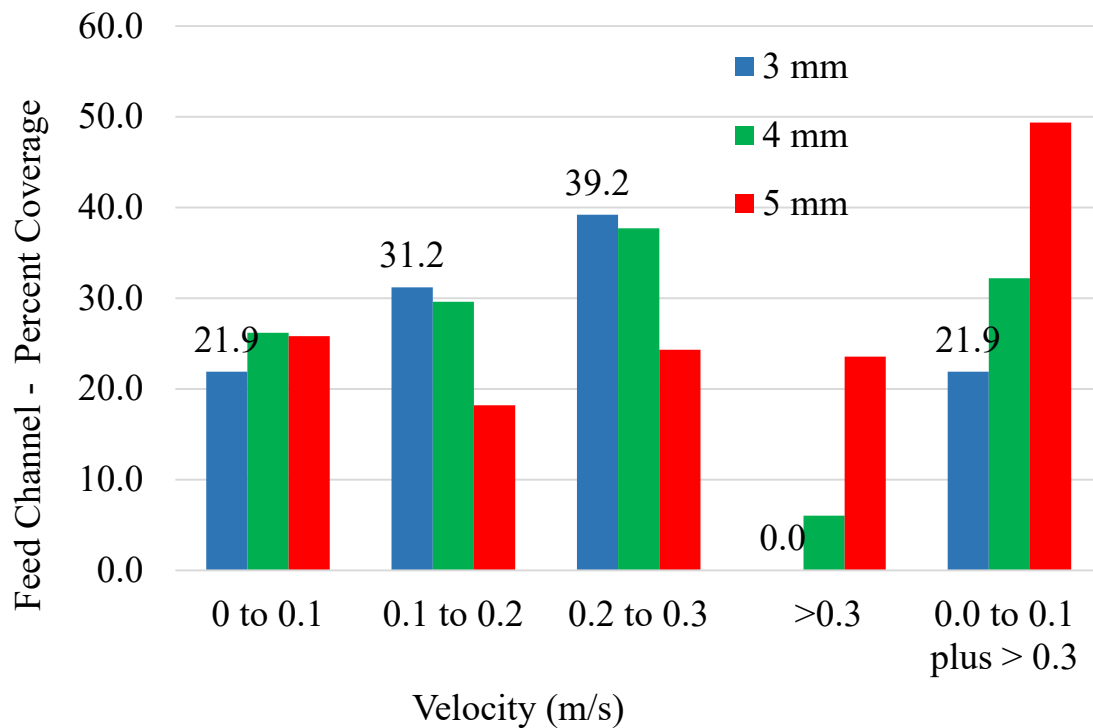


Figure 3.15 The different velocity zones compared for each chevron length modeled using the base design pattern: offset, 3 mm chevron length, and 5.75 mm gap. The 90 degree offset geometry provided the optimal conditions across all flow velocities with 39.2 in the enhanced region. (Note: Areas presented do not include 6.3% due to chevron and 1.5% image processing error.)

3.3.2 Fluid flow profile

A modified membrane was placed into a transparent acrylic crossflow cell for fluid flow visualization. The membrane swatch was run 24 hours for compaction and equilibration under experimental condition parameters previously defined. After 24 hours, fluorescence beads were introduced for fluid flow imaging which showed the beads moving straight without turbulence at the front of the chevron in the open channel, between

the micromixers then veering off and flowing down the side of the chevron, Figure 3.16. The video and imaging of the backside of the chevron showed an unhindered flow path with beads flowing from

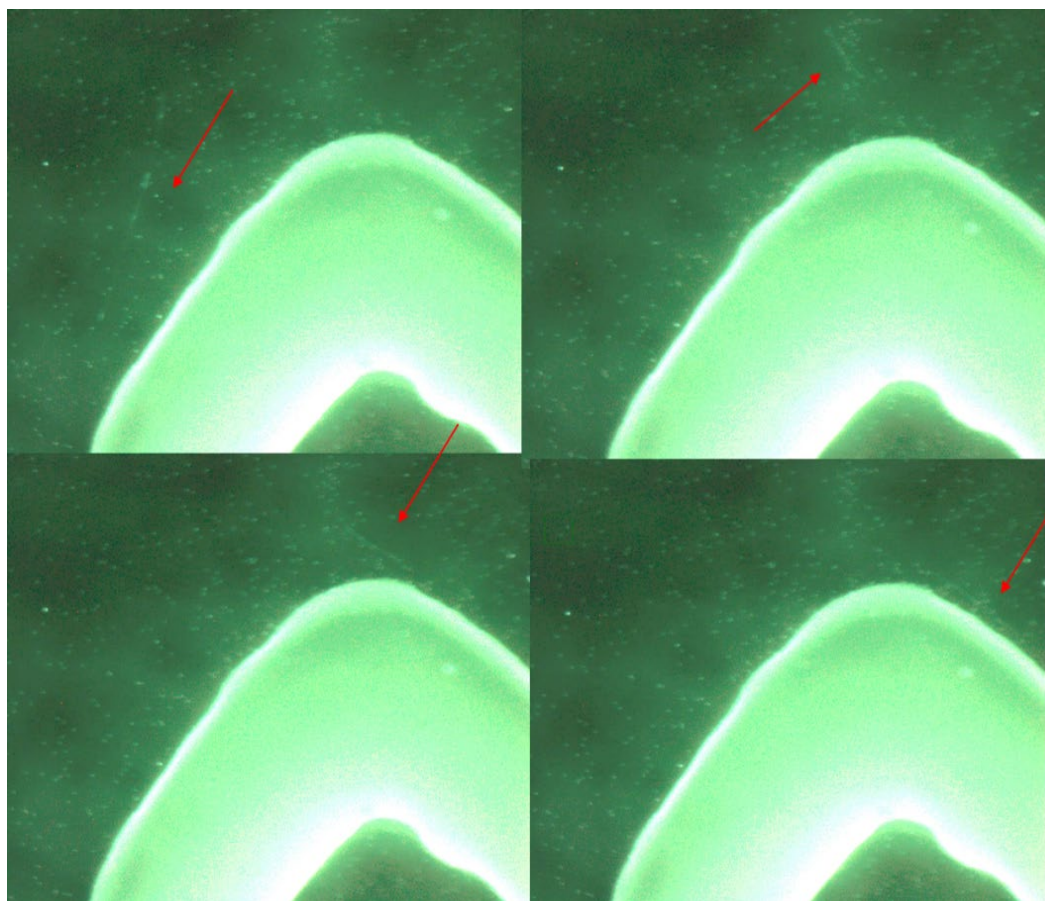


Figure 3.16 Forward flow profile front of chevron – 2 μm florescent beads with 90 degree angle, offset pattern, 5.75 mm gap and inlet velocity of 0.104 m/s supporting modeled fluid flow profile (video of the flow at the tip of chevron micromixer observed with the aid of fluorescence beads is available at <https://doi.org/10.6084/m9.figshare.7312313.v1>). around the sides of the chevron into the backside of the chevron and then out the back as depicted in Figure 3.17. These images integrated with the flow modeling validate the fluid flow.

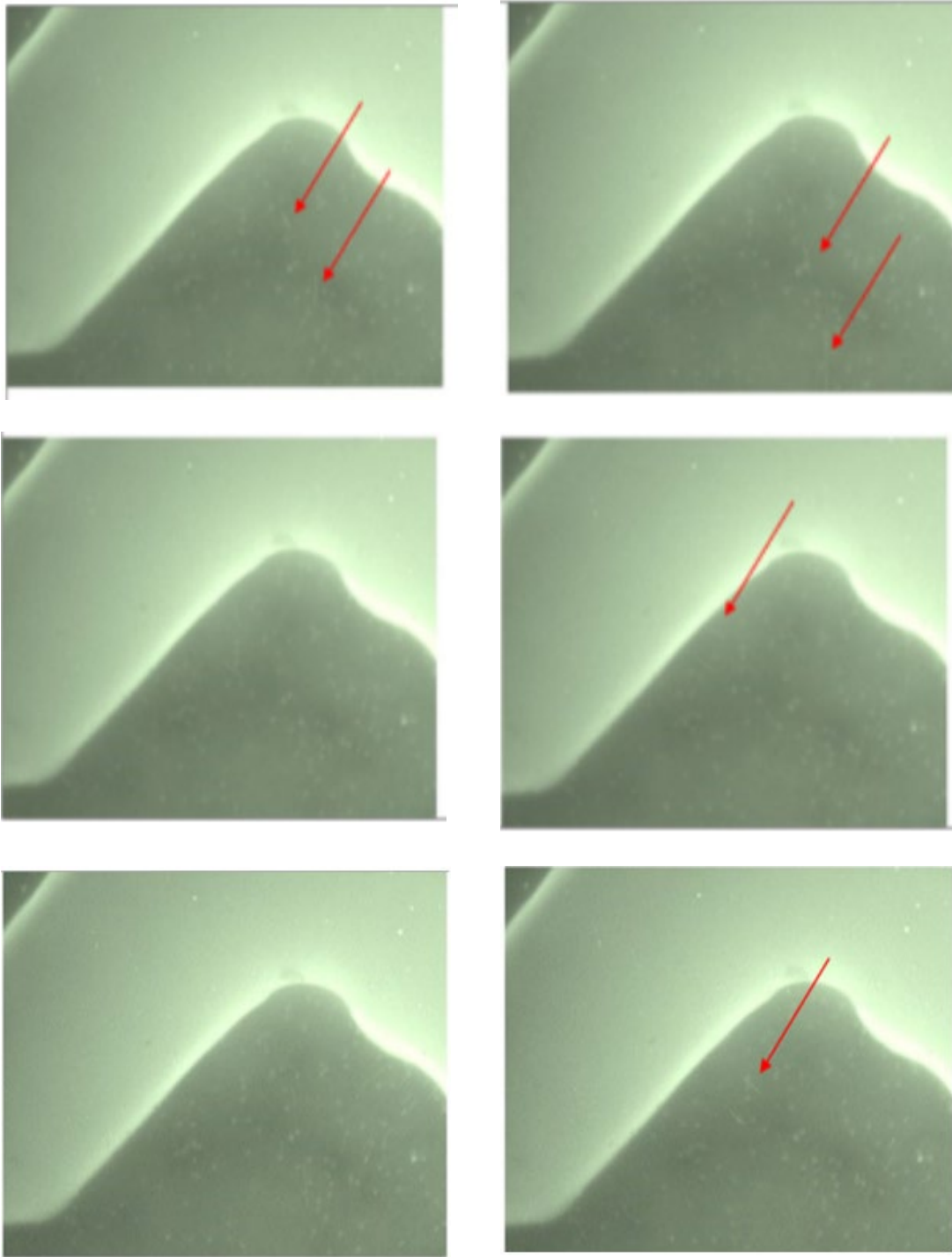


Figure 3.17 Forward flow profile back of chevron – 2 μm florescent beads with 90 degree angle, offset pattern, 5.75 mm gap inlet velocity of 0.104 m/s supporting modeled fluid

flow profile (video of flow profile observed with the aid of fluorescence beads is available at <https://doi.org/10.6084/m9.figshare.7309148.v1>).

3.4. Discussion

Different chevron features were modified and modeled to determine which chevron geometry and pattern created a feed channel with the greatest coverage in the enhanced zone, 0.2 m/s to 0.3 m/s and the lowest coverage in the 0 to 0.1 m/s range, low flow and dead zone. As described in section 3.3.1 the base model was a chevron geometry of 3 mm length, 0.1 mm width, 5.75 mm gap, 90 degree angle and an offset pattern.

The first variations modeled were all three angles: 60, 90, and 120. The no/low flow zones developed slightly in front of each chevron with the majority directly behind each feature. The higher percent area covered by the low flow zone correlated to more potential for fouling to initiate and develop on the membrane and feed channel. The low flow zone setting up around the chevron indicated that the feature itself had the potential to be a point of fouling. The enhanced velocity region was pronounced in the open channels around the chevrons, Figure 3.4. The velocity profile, Figure 3.5, showed the 90 degree angle providing the best continuous feed channel coverage in the enhanced zone of 39.2% while the 60 and 120 degree angle had less than 30% coverage. The 90 degree angle also generated minimal comparable membrane surface coverage for the low flow zone, 21.9%.

Using the same parameters described above except for changing the patterning from offset to continuous showed extreme channeling of the velocity profile for all angles as can be seen in Figure 3.8. All three models showed greater than 30% coverage in the no/low

flow velocity zones (0 to 0.1 m/s) behind each chevron extending to the front of the following chevron. The percent coverage of the velocity profile in the enhanced zone, Figure 3.7, did not improve for any angle by changing from the offset to the continuous pattern clearly showing no benefit of a continuous pattern for maximizing unhindered open channel flow at velocities in the enhanced zone and minimal in the no/low flow zone based on these modeling parameters. Both minimizing the percent coverage defined by the fouling zone velocities and maximizing the enhanced velocity zone percent coverage were achieved by the 90 degree angle offset previously described, when compared between the six models. Based on this modeling data the 90 degree offset model with the base design parameters established previously was selected for continuation into the next modeling variation.

Evaluating two additional gap distances showed that a constriction of 0.75 mm created a high velocity area between the chevrons with 9.1% coverage compared to the 5.75 mm and 10.75 mm which produced zero coverage in this zone. The small gap area also generated the highest coverage in the no/low flow zone behind and in front of the feature at 33.4% clearly showing this was not an optimal design enhancement. Moving this gap in the other direction, the 10.75 mm width had the opposite effect with no zones going over 0.25 m/s and channeling occurring as if in a continuous pattern. The majority of the coverage was in the unimproved zone showing that a large gap eliminates previous benefits with similar design characteristics. Neither increasing nor decreasing the width between the chevrons provided and improvement in coverage of the enhanced zone from the original width. In fact, the 5.75 mm width originally modeled had 1.5 more coverage

in coverage compared to the 10.75 mm gap, and a 5.5 more coverage than the 0.75 mm gap for the enhanced zone, Figure 3.11. While having a distance too far between the features minimized the offset pattern enhancement for the dimensions modeled generating a velocity profile more like the continuous pattern with channeling of the enhanced velocity in the gap between the chevrons with an unimproved zone behind each feature and to the next. Based on the percent velocity coverage of 39.2% the 3 mm in length, 0.1 mm thickness, 90 degree angle in an offset pattern with a gap of 5.75 mm still provided the most enhancement and least fouling potential as an integrated feed channel based on the modeling parameters selected.

Modifying the chevron length to 5 mm showed an increase in the membrane area covered in the non-recirculating zone, greater than 0.3 m/s of almost 24%; the enhanced zone, the primary focus was approximately 24%. The increase of the chevron size to 4 mm and 5 mm resulted in the no/low flow region immediately behind the chevrons increasing slightly compared to the 3 mm, 24.2% and 25.8% respectively. The 4 mm chevron length provided similar coverage in the velocity range from 0.2 to 0.3 m/s. However, the total fouling zone (0 to 0.1 m/s and >0.3 m/s) was 1.5 times that observed when using a 3 mm chevron length. Based on zero coverage for the increased velocity profile greater than 0.3 m/s and minimal no/low flow behind for the 3 mm chevron the final design variation supported the selection of a chevron 3 mm in length, with a 90 degree angle, with a 5.75 mm gap and in an offset pattern.

Table 3.3 The percent coverage in the defined feed channel for each velocity region of interest as a comparable unit area of quantification for the ten models evaluated. The optimal design is highlighted in green having the highest enhanced zone and minimal fouling zones.

	Velocity Profile (m/s)					Sum of Fouling Zones 0 to 0.1 and > .3
	No/low flow zone 0 to 0.1	Unimproved zone 0.1 to 0.2	Enhanced zone 0.2 to 0.3	Non-recirculating zone >0.3		
60 degree offset	19.2	46.7	25.6	0.0	19.2	
90 degree offset	21.9	31.2	39.2	0.0	21.9	
120 degree offset	26.0	41.7	25.4	0.0	26.0	
60 degree continuous	31.9	50.9	15.3	0.0	31.9	
90 degree continuous	37.7	35.5	24.0	0.0	37.7	
120 degree continuous	38.9	26.7	29.6	3.5	42.4	
Gap 0.75 mm	33.4	31.0	9.5	9.1	42.5	
Gap 10.75 mm	21.1	47.7	25.2	0.0	21.1	
4 mm length	24.2	27.6	35.7	4.0	32.2	
5mm length	25.8	18.2	24.3	23.6	49.4	

3.5 Conclusion

CFD modeling was used to evaluate different microstructures dimensions and patterning to determine the shape and pattern of chevron micromixers that created the optimal hydrodynamic conditions to reduce fouling and enhance flow in a SWE feed channel. The model results support the hypothesis that optimized microstructure design and patterning can maximize the area of enhanced channel feed velocities (0.2 – 0.3 m/s) and minimize velocities associated with fouling (<0.1 m/s, >0.3 m/s). The optimized chevron geometry was a 90 degree angle with an offset pattern, a 3 mm chevron length, and a 5.75 mm gap. The optimal micromixer design and pattern were printed directly on the RO membrane as a proof of concept demonstration that individual features could be printed on a membrane surface by a 3-D printer. The flow profile observed during

laboratory trials were consistent with CDF model predictions and confirmed the individual micromixers provided an unhindered flow path.

CHAPTER 4: DIRECT PRINTING OF MICROMIXERS ON REVERSE OSMOSIS MEMBRANE SURFACES REDUCE CHEMICAL FOULING

4.1 Introduction

The use of reverse osmosis (RO) membranes for desalination has tripled since 2000 with 16,000 plants operational worldwide. RO currently makes up 65% of the technology market for desalination with the closet follower, multi-stage flash at 21%. The emergence of RO as the leading choice is due to requiring only ten percent of the energy of distillation (note this is still seen as energy intensive), modularity of the treatment trains allowing scale up, and the support chain associated with using the RO process for desalination (Cohen et al. 2017). While RO is primarily utilized for desalination it is also effective at rejecting a wide array of potential pollutants (e.g., metal, bacteria, pesticides) making it a viable treatment process for water reuse from sources such as wastewater effluent and processed waters. Overtime, the buildup of materials on the active membrane surface and/or on the feed spacer (i.e. fouling) causes reduced operational performance. There are multiple types of fouling that occur simultaneously depending on the physical-chemical conditions present within the RO unit. The type of fouling can be broadly classified as: (1) scale fouling - due to the chemical precipitation of solutes due to the high concentration gradient at or near the membrane surface; (Thompson et al. 2017) (2) colloidal fouling - due to the entrapment of particulate or colloidal matter, such as iron flocs or silt; (3) biofouling - the growth of a biofilm on the membrane surface or feed spacers present between the membranes; and (4) organic fouling - the adsorption of specific organic compounds such as humic substances and oil on to the membrane surface. (Ho et al. 1992; Solutions 2010)

Researchers have tried to solve the problems associated with fouling in numerous ways such as surface modification of the membrane, new feed spacer designs, and printing directly on the membrane surface with limited success (Suwarno et al. 2012; Picioreanu et al. 2009; Koutsou et al. 2007; Vrouwenvelder et al. 2006; Vrouwenvelder et al. 2009; Radu et al. 2010). Hydrodynamics within the feed channel are critical to controlling fouling initiation and growth (Guillen and Hoek 2009). In Chapter 3 computational fluid dynamic (CFD) modeling was employed to enhance hydrodynamic conditions in membrane feed channels using microstructures. Printed membranes were then used to verify CFD model results. Based on Chapter 3 results, the area where fouling was likely to occur, based on hydrodynamics, was minimized by optimizing the shape and pattern of the printed microstructures. In this chapter, the chemical fouling of the enhanced 3D printed micromixer design and pattern is explored.

Scale fouling at the membrane surface is major limiting factor in the service life of RO membranes (Karabelas et al. 2014). Scale formation occurs as salts build up at the membrane surface causing concentrations to exceed the limits of mineral saturation (Thompson et al. 2017). Sparingly soluble salts such as calcium carbonate, barium sulfate, calcium sulfate, strontium sulfate and calcium fluoride are often the first to precipitate out of solution (Solutions 2010). The concentrations of salts at the liquid-membrane interface is known as concentration polarization (CP) and is known to induce the scale formation and deposition onto the membrane surface and in the feed channel (Gallab et al. 2017). This reduces the flux that can be achieved without irreversible scaling out the membrane

or adding an antiscalant prior to RO when mineral salts are present which has other limitations.

Calcium sulfate is commonly used to evaluate scaling as the chemical reactions are well defined (not sensitive to pH variation, straight forward kinetics, etc.) (Shmulevsky et al. 2017; Bystrianský et al. 2016; and Karabelas et al. 2014). Crystallization of calcium sulfate in membrane processes has been extensively studied and is known to occur in either the bulk (homogeneous) or surface (heterogeneous) or both as can be seen in **Figure 4.1** below. Bulk crystallization is due to “random collisions of the ions in motion” in the concentrate stream building upon each other until a cluster of ions form and precipitation occurs. Surface initiated crystallization may be caused by the roughness of the membrane surface with both occurring in the CP boundary layer. As a result, the deposition of crystal formation in the bulk phase causes flux decline due to a cake layer formation while the dihedral growth of crystals on the membrane itself cause flux decline due to surface blockage (Lee and Chung-Hak 2000).

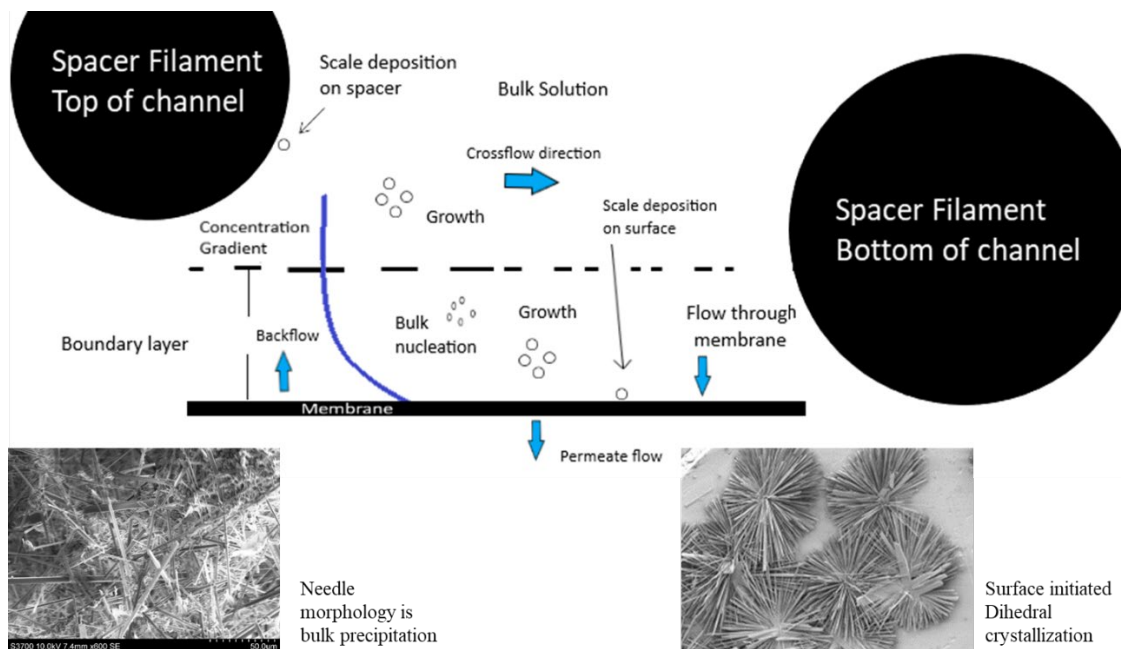


Figure 4.1. Depiction of the two different type of scaling phenomenon that can occur with calcium sulfate initiated by boundary layer effects. Heterogeneous nucleation and surface initiated scale (Yoram Cohen, personal communication, November 4, 2018, Surface initiated Dihedral crystallization image) or bulk precipitation brought on by homogeneous nucleation followed by deposition on the feed spacer and membrane surface.

The objective of research presented in this chapter was to evaluate the scaling potential of the 3D printed micromixers, compared to standard feed spacers used throughout the industry, and determine if the enhanced hydrodynamics translate into maintaining longer periods of adequate flux. With this aim, the following hypothesis was evaluated: the optimal design and pattern of the micromixer identified through computational modeling, based on hydrodynamics, will minimize scaling relative to a standard feed spacer. To evaluate scaling, precipitation of calcium sulfate was selected as

the fouling mechanism to compare spacer modifications that were surface enhanced versus standard operating conditions due to the repeatability of creating the scaling water.

4.2. Materials and Methods

4.2.1 Printing of micromixers on membrane

A BioBots model 1 (Philadelphia, PA) 3D printer was modified in-house at the United States Army Tank Automotive Research, Development and Engineering Center (TARDEC) in Warren, MI to print stabilized micromixers directly on the surface of a membrane without additional processing steps. This included an enhanced print head with four, ultraviolet light emitting diodes (UV LED) with a separate power source to control intensity. A larger print platform was also utilized to print to the entire active membrane area utilized by the cell.

4.2.2 Printing of micromixers on membrane

Enhanced micromixers based on previous CFD modeling (Chapter 3) were printed on the thin film composite polyamide reverse osmosis membranes. Solidworks (Dassault Systèmes, Vélizy-Villacoublay, France) was used to translate the enhanced design pattern to the feed channel dimensions of the Sterlitech (Kent, WA) laboratory crossflow cell utilized in the scaling experiments. The STL file was uploaded to the BioBots print platform where it was prepared for the printer using a slicing software, Repetier host (Hot-World GmbH & Co. KG, U.S.). The UV curable epoxy, UV15TK (Masterbond, Hackensack NJ) was poured into the syringe to the 5 ml mark capped with a 30 gauge needle and inserted into the printer for printing. Through a trial and error process, a pressure setting of 30 psi was found to provide the optimal deposition on the membrane

surface. The epoxy and static curing process were previously verified through FTIR analysis to not cause any significant chemical changes in the membrane (Altman et al. 2010)

4.2.3 High pressure membrane cross flow cell system

A modified high pressure cross flow membrane system purchased from Sterlitech was used to conduct experiments, see Figure 4.2. The system contained one RO cell for running a flat sheet membrane with an effective membrane surface area of 140 cm². The cell channel depth was 0.8636 mm (34 mil) so stainless-steel shims were used to achieve the 0.508 mm (20 mil) feed channel height of the printed feed spacer and low foulant mesh feed spacer. The volume of the stainless steel feed tank was 16 liters with an integrated chiller (Model 6506 Polyscience Warrington, PA) to maintain a constant temperature of 25°C during each experiment. A high-pressure pump with a variable frequency drive (Hydra-Cell model F20K52GSNEM, Wanner Engineering, Minneapolis, MN) was used to pump the feed solution at 0.5 liter per minute to the crossflow cell and to set a constant feed flow velocity.

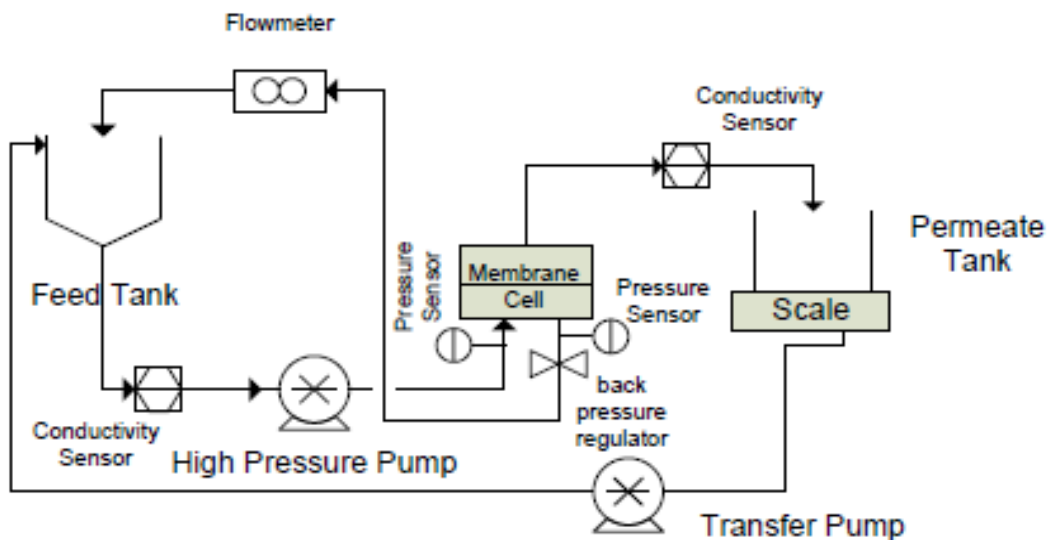


Figure 4.2 Experimental RO membrane test system. System utilizes modified Sepa®CF membrane cell outfitted with 2 conductivity sensor, 2 pressure sensors, and 1 flow meter.

The fine tune valve for adjusting pressure from 400-1000 psi was replaced with a backpressure reducing valve (Model BPH05-02T, Straval, Elmwood Park, NJ) to provide constant pressure from start to finish of each run. A remote conductivity sensor was integrated into the flow cell to allow real-time measurement of product water conductivity. A product water collection system was setup on the benchtop scale (EL6001 Mettler Toledo; Columbus, OH) to allow real-time measurement of the permeate flow. The bulk feed water composition was maintained by an automated system that periodically emptied the product water back into the feed tank based on the volume reaching approximately 1 Liter. The system configuration allowed experiments to be run continuously (i.e. 24 hrs. per day) with uninterrupted data logging of key parameters through a human interface to

an automatic data acquisition. Parameters logged included: inlet feed pressure and reject feed pressure, feed and permeate conductivity, and permeate mass collected per unit of time.

4.2.4 Membrane Performance and Characterization

Commercial flat sheet RO membranes, SW30XLE manufactured by Dow Filmtec (Dow Chemical Co., Midland, MI) were used in this study. Manufacture specified flux range was 23/800 to 29/800 (GFD)/psi with a NaCl rejection of 99.5%. Membranes were stored in a glass beaker fully submerged in deionized water for one hour prior to being inserted into the crossflow cell. Solutions were prepared using de-ionized water and sodium chloride (Reagent Plus NaCl >99.0%) purchased from Sigma Aldrich (St. Louis, MO). Membrane experiments were conducted in the Sterlitech stainless steel crossflow laboratory test cell, with an active membrane area of 140 cm². Two metal shims were placed in the feed channel to reduce the thickness of the feed channel to 0.508 mm for all experiments. Flowrate to the cell was controlled by a variable frequency drive set to maintain an inlet feed velocity of 0.104 m/s.

Experiments began by running distilled water at 20.7 bar through the membranes for 24 hours to ensure compaction and stabilization. Once the flux was determined to be constant, 1L of 0.4 M NaCl solution was added to the reservoir while the system was running; resulting in a 16L, 0.034 M NaCl feed solution. Periodically during the experiment, the pressure regulator was adjusted slightly to maintain a feed pressure of 20.7 bar \pm 0.2 bar. The system was run for 24 hours and considered stable and ready for scaling experiments once the product water flux and salt rejection stabilized and were within 3%

of the membrane manufactures specifications. Conductivity measurements were used to quantify salt concentrations. Salt rejection was considered stable when the calculated rejection was within 3% of membrane specifications based on inline conductivity measurements (see Appendix A for additional information). Additional measurements of the conductivity of the bulk feed solution and product water were made using a handheld conductivity meter before scaling tests were initiated for calibration verification.

4.2.5 Calcium Sulfate Scaling Experiment

After 48 hours of membrane operations as described above if the membrane was determined to be within 3% of the membrane manufacturer specifications for flux and rejection the scaling study was started. If the membrane was outside of the 3% the experiment was stopped and started over again with a new membrane. Solutions were prepared using de-ionized water, ACS grade calcium chloride ($\text{CaCl}_2 \cdot 2\text{H}_2\text{O}$) from LabChem and ACS grade sodium sulfate (Na_2SO_4) from Sigma Aldrich (St. Louis, MO). While the system was running, two liters of the feed solution were drained from the reservoir into a 2 Liter beaker this volume was replaced by a 1 liter 0.407 M CaCl_2 added to the 14 liter feed solution followed by addition of 1 liter of 0.408 M Na_2SO_4 to the 15 liter solution, resulting in a 16 liter 0.0304 M Na_2SO_4 and 0.0304 M CaCl_2 feed solution at the onset of the scaling experiment. This protocol ensured the same scaling solution would be used each time. Scaling experiment were carried out for 24-48 hours and were conducted in triplicate to account for experimental variation. After 24-48 hours of scaling the pressure was slowly reduced until it reached zero and the flow stopped by reducing power to the feed pump.

Following scaling, membranes were removed and analyzed using a Bruker AXS S4 Pioneer sequential X-ray fluorescence spectrometer (XRF). It is capable of qualitative and quantitative chemical analysis of materials. Followed by SEM analysis to determine what type of crystallization occurred.

4.2.6 Cleaning System

Once the scaling experiment was complete the feed tank was completely drained. The reservoir was cleaned with tap water until precipitate was no longer visible on the inside of the tank and cooling coils. The tank was then rinsed with distilled water (DI) until water from the system drain had a conductivity equal to that of DI water ($1.65 \mu\text{s}/\text{cm}$ at $23.3 \text{ }^\circ\text{C}$). The cell was released from pressure and removed from the cell holder. The membrane was removed from the cell along with shims, feed spacer for the unmodified membrane and permeate spacer where appropriate and rinsed first with tap water then DI water. A waste membrane with imperfections was then loaded into the cell to perform the additional cleanings and flushing. Once clean, the feed tank was filled with DI water. The reject hose was disconnected and placed into a separate collection container and run at 0.5 LPM for five minutes. Chlorine and vinegar were added at dilute concentrations, 60 ml each to the feed tank and recirculated for four hours then drained. The feed tank was flushed again with DI water and the system was drained with all parts exposed to air to dry.

4.2.7 Optical Assessment of Scale Formation

To visually assess the formation of scale over time, fouling experiments were also carried out in a low pressure acrylic cross flow cell supplied by Sterlitech (Kent, WA). The acrylic cell had an effective membrane surface area of 140 cm^2 . The cell channel depth

was 0.8636 mm so acrylic shims were used to achieve the 0.508 mm feed channel height of the printed feed spacer and low foulant feed spacer. The same experimental setup (i.e. polypropylene feed tank (16 Liters), pump (Hydra-Cell model F20K52GSNEM, Wanner Engineering, Minneapolis, MN) backpressure reducing valve (customized product ¼ inch BPH05-02T)) described previously were also used for optical experiments. For the optical experiments a constant inlet feed velocity of 0.104 m/s was maintained. A digital color camera DS-Fi3 5.9 megapixel (Nikon Melville, NY) was utilized to take photos every one minute so that scale development could be visually characterized.

4.3. Results

4.3.1 Channel crossflow velocity

Standard feed channel dimensions without a printed spacer or feed spacer were used to calculate the fluid flow characteristics, consistent with laminar flow conditions typical of spiral wound elements. With a cell width of 165 mm and a channel height of 0.508 mm (20 mil) result in a calculated the inlet flow velocity of 0.104 m/s. The calculated velocity is for an un-impinged feed channel. Typical flow rates of a lead element range from 0.07 to 0.6 m/s (Gimmelshtein et al. 2005). However, in the actual spiral wound element configuration with two membrane leaves separated by a mesh feed spacer the velocity created in the channel does not exceed 0.4 m/s (Koutsou et al. 2007). The inlet velocity used in this work, 0.104 m/s, within this typical range and was used to allow for comparison to other work (Bucs et al. 2014). A velocity of 0.104 m/s was also used for the CFD modeling presented in Chapter 3. Using this velocity and the cell parameters described above the Reynolds (Re) number was calculated to be 102 which is laminar flow based on

the transition from laminar to turbulent flow occurring at a Re 2000 (Mulder 1991). Based on the flowrate used the printed micromixer pattern would provide 43% percent coverage in unimpeded channel flow in the enhanced zone 0.2 to 0.3 m/s.

4.3.2 Membrane characterization

To ensure that the process of curing the individual micromixers onto the membrane surface did not impact the membrane, a control sample was run. The control sample was handled like the printed membranes but without curable epoxy applied to the membrane surface. Importantly, the control membrane was exposed to the same intensity and duration of UV light as the printed membranes. Following UV exposure, the control membrane soaked for one hour in DI water and placed in the RO cell to determine flux and salt rejection. After 24 hours of running with DI water followed by 24 hours of 0.034 M NaCl feed solution the flux and salt rejection of the control membrane was found to be within 3% of the membrane manufacturer's specifications.

Printed micromixers, individual chevrons, were characterized using a profilometer. A total of 81 micromixers were printed in the 140 cm² of active membrane area utilized by the high-pressure crossflow cell. The design created in Solidworks were printed micromixers 0.1 mm thick and 0.508 mm high; theoretically reducing the active membrane surface area by 1 cm². The 3D printer was not able to print a 0.1 mm width micromixer, instead the line thickness averaged 3 mm reducing the active membrane area to 88.2 cm². The calculation utilized was the same equation used by Sandia (Altman et al. 2010) to calculate their active membrane area after robocasting.

Based on the calculated active membrane area, a significantly improvement in pure water flux was observed relative to non-printed membranes, Figure 4.3. While an improved flux would be beneficial it is unlikely based on the modification that was made. The pure water flux is not impacted by concentration polarization so it is more likely that the active membrane is higher than the calculated area used to determine flux.

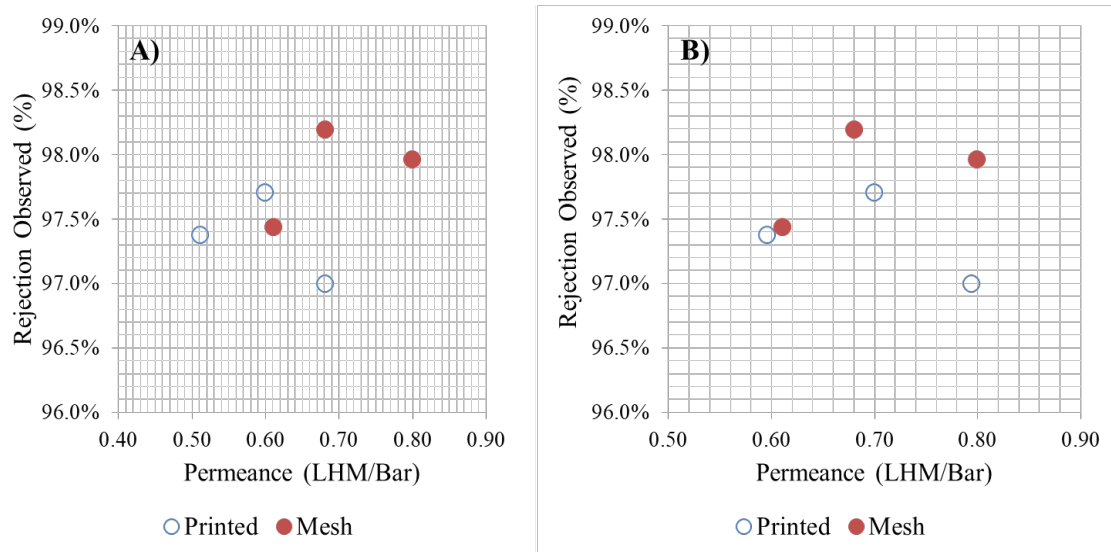


Figure 4.3 Normalized permeance and salt rejection for modified and unmodified membranes: A) the active membrane area for the modified was 88 cm² based on measuring the physical micromixer dimensions B) the average active membrane area was calculated to be 120 cm² using the average pure water flux for the unmodified membranes based on no concentration polarization effects and salt rejection being within 3% showing no membrane damage.

The pure water flux (J_w) was measured and used to calculate the pure water permeability (A) where ΔP is the pressure differential across the membrane and the osmotic pressure differential is zero for pure water (see Appendix A for additional

information). A 0.034 M NaCl solution was then introduced as the feed solution and the permeate flow was measured along with the product water conductivity. Once stabilized, the product water conductivity measurements were used to determine the observed salt rejection. Both intrinsic membrane transport properties were within 3% of the membrane manufacturers specifications. The values calculated for the modified membranes compared to unmodified membranes indicating the printing process did not damage the membranes and ensuring that the membrane samples were operating with at the same metrics at the start of the scaling experiments.

4.3.3 Scaling experiment

Calcium sulfate scaling experiments were conducted in triplicate for surface modified membranes with individual micromixers and unmodified membranes using a standard feed spacer. The initial flux of 14.5 LMH was established at the beginning of each test and the pressure was held constant through the remainder of the experiment to allow for a direct comparison of flux response over time. Each membrane test began by passing DI water through the flow cell at a rate of 0.104 m/s for 24 hour to ensure membrane compaction and a constant permeate flux. With the pressure and permeate flow rates stabilized, a 0.4 M NaCl solution was passed through the RO filter for 24 hours to validate the integrity of the membrane was not compromised, and then the calcium sulfate solution (0.0304 M CaCl and 0.0304 M NaSO₄) solution was introduced to induce scale.

As observed in Figure 4.4, a stable flux was observed for the 5.5 hours prior to introducing the scaling solution. Both the modified and unmodified membranes behaved similarly after introduction of the scaling solution for the first 10 hours with the first 5

hours equilibrating to the increased ionic strength of the feed solution. This was followed by a sharp, linear decline in flux for 3 hours. This decline was observed for both printed and non-printed membranes. Then the flux leveled off and was stable for the next 2 hours. It was at this point that the flux for the mesh feed spacer rapidly declined over the next 12 hours to 78% of its original value while the printed feed spacer only dropped by 24%.

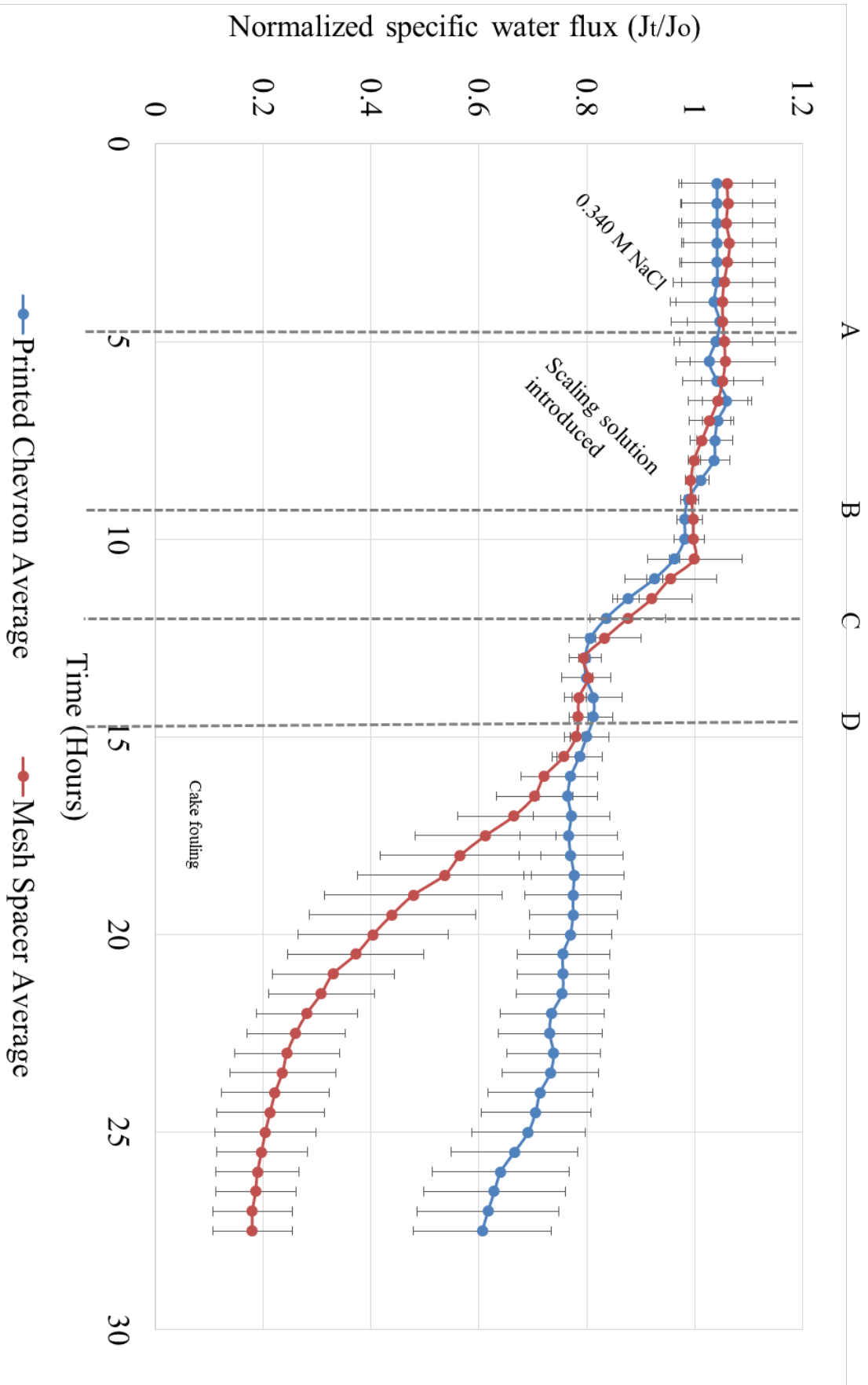


Figure 4.4 The normalized specific flux of the modified and unmodified membranes over the course of scaling experiments. After stable filtration of a 0.340 M NaCl solution was established, the 0.0304 M CaCl and 0.0304 M NaSO₄ scaling solutions were introduced at time point A. The ionic strength in the flow cell reached steady state at time point B. Calcium sulfate scaling initiated and equilibrated at time point C and was followed by cake fouling of the unmodified membrane at time point D. Average permeance (n=3) is reported with standard deviation.

4.3.4 Surface characterization.

Samples were taken from the different swatches after the scaling experiments. X-Ray analysis confirmed that the elemental composition of the scaling layer was in fact calcium sulfate, Table 4.1 with peaks at calcium and sulfur, see Figure 4.5. Samples were also examined using SEM analysis to look at the scale crystallization. No surface initiated scaling was present on any of the swatches sampled all scaling was needle morphology

Table 4.1 Elemental concentration of calcium and sulfur from XRF verifying calcium sulfate scale was the only foulant present.

Element	Atomic #	Conc. (%)	Stat. Dev
Na	11	0.05	0.0074
Si	14	0.163	0.0077
S	16	9.362	0.043
Cl	17	0.23	0.014
Ca	20	9.675	0.033
Ti	22	0.0469	0.0027
Cr	24	0.015	0.0019
Fe	26	0.0855	0.0025

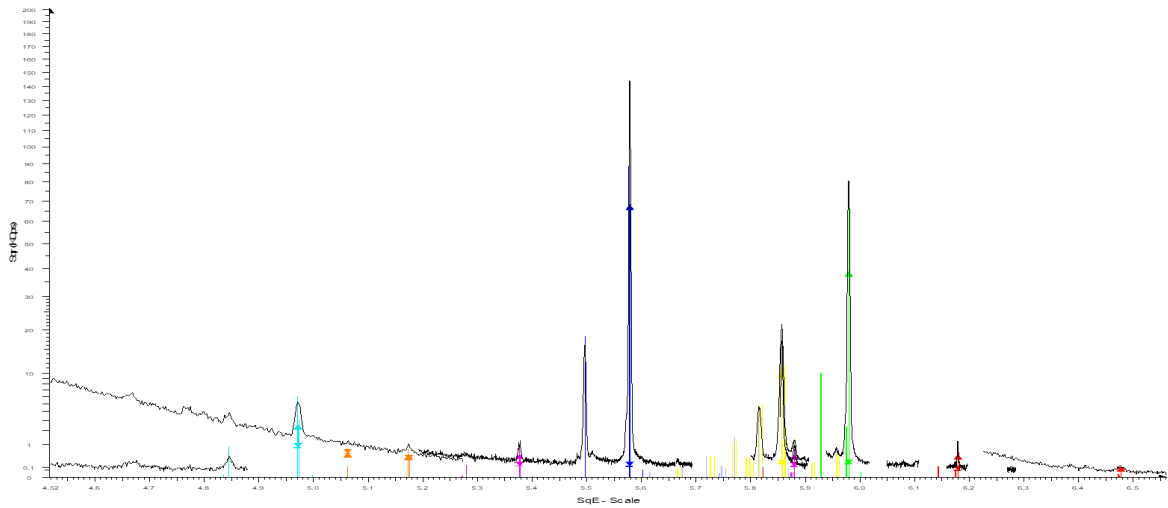


Figure 4.5 After the scaling experiment the scaled unmodified membrane was removed and a sample was analyzed by a Bruker AXS S4 Pioneer sequential X-ray fluorescence spectrometer (XRF) which the peaks at verified the scale present was calcium sulfate.

bulk precipitation-initiated scale. As can be seen in Figure 4.7, the mesh feed spacer itself became points for nucleation and accumulation of scale to create a denser cake layer that caused the significant decline in flux. While the printed feed spacer, Figure 4.6 showed points of bulk scale attaching itself to the membrane but not a dense cake layer or deposition on the micromixer itself.

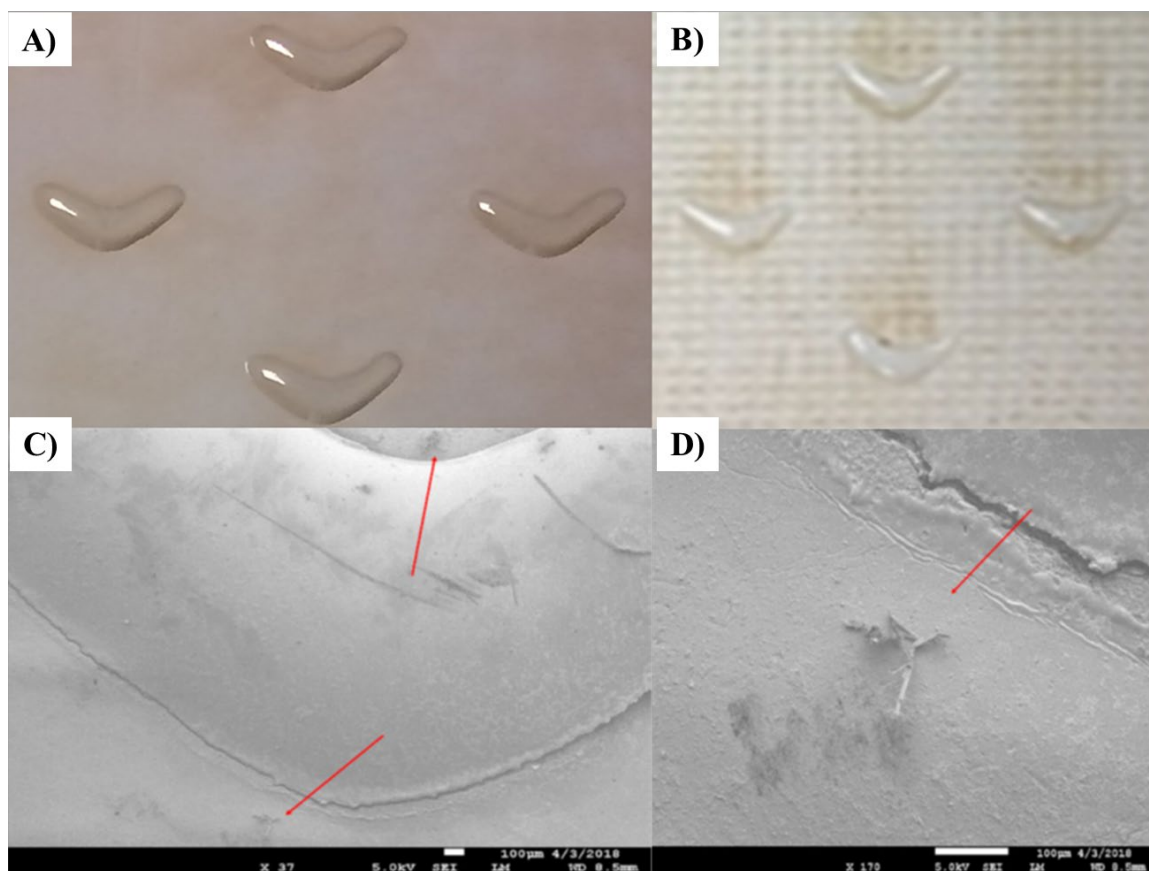


Figure 4.6 Optical and SEM imaging of micromixers printed directly on the membrane surface before and after scaling experiments showing minimal scale deposition on the membrane and micromixers.

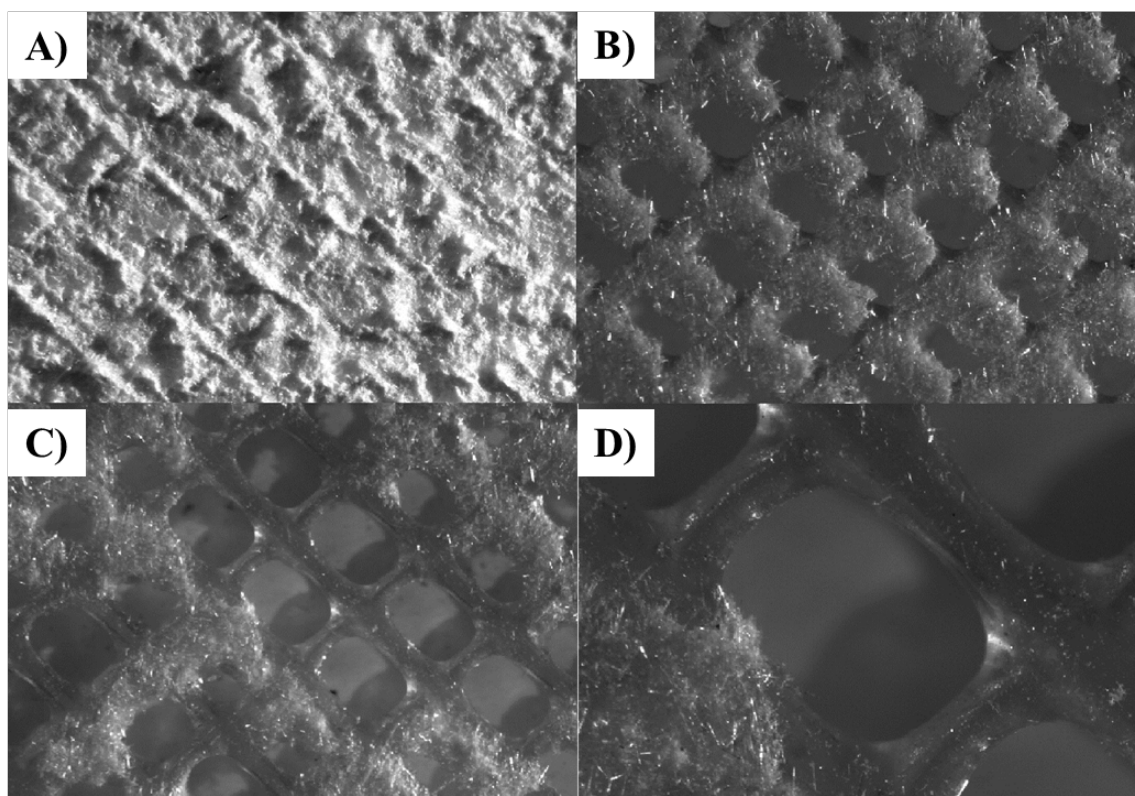


Figure 4.7 Optical imaging of membrane surface and mesh feed 20 mil mesh feed spacer after scaling experiments showing heavy membrane scaling on spacer and membrane.

While the scaling layer was so dense on the membranes that used the mesh spacer Figure 4.8, shows a pocket into the layer development itself. There are no two stemmed crystal structures that would be indicative of surface initiated scaling.

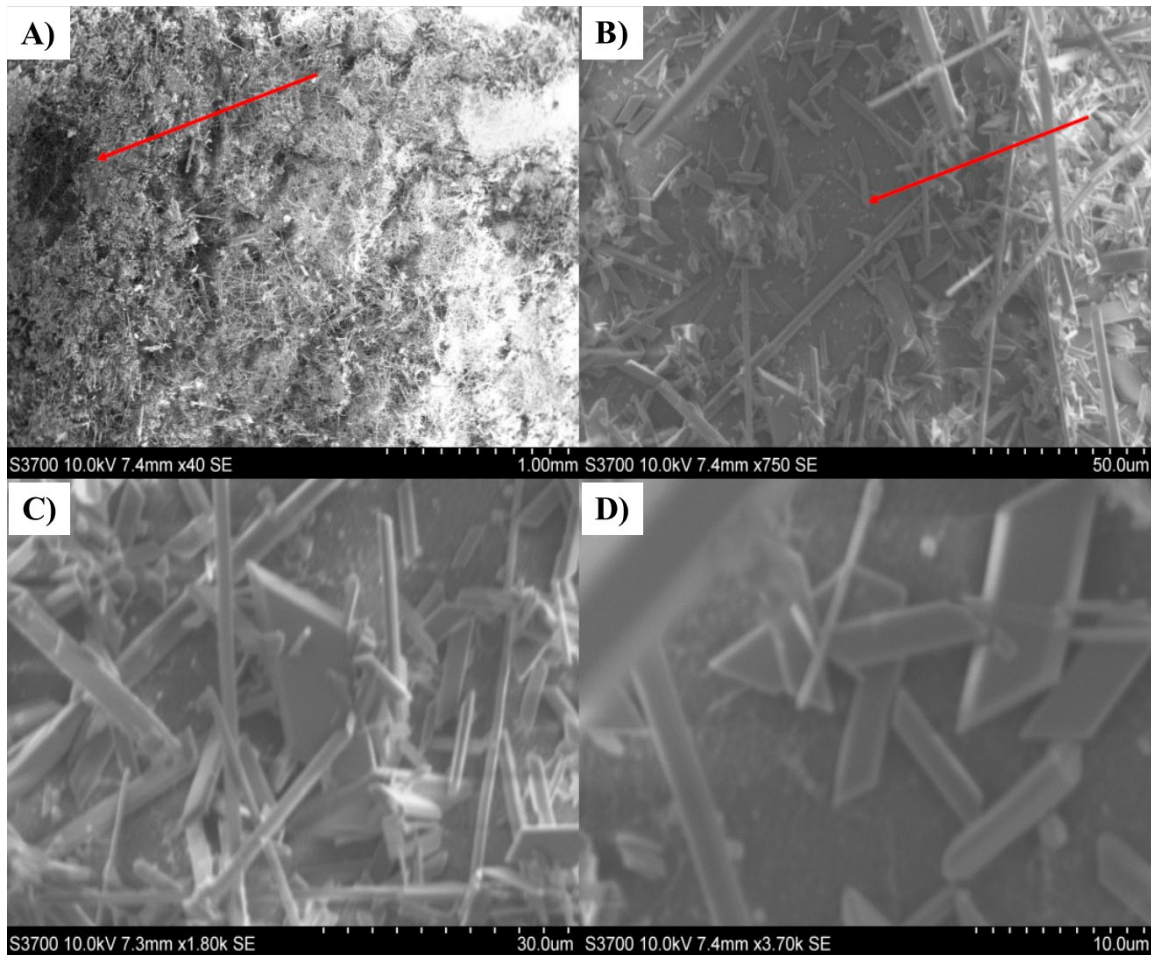


Figure 4.8 SEM imaging of unmodified membrane surface utilizing a 20 mil mesh feed spacer after scaling experiments showing bulk scaling with no surface initiated scale.

4.3.5 Scaling formation

Utilizing an acrylic transparent cell an RO membrane with the standard 0.508 mm mesh feed spacer utilized in previous experiments was exposed to the same operating conditions as the flux decline experiments previously described. Figure 4.9 B. shows that the scale first starts to setup on the membrane surface appearing to be a shiny crystal lattice forming. This is followed by a change in deposition and growth onto the feed spacer,

Figure 4.9 C. which is similar to the SEM picture seen in Figure 4.7. The last picture Figure 4.9 D, shows a heavily scaled feed spacer at the end of the experiment.

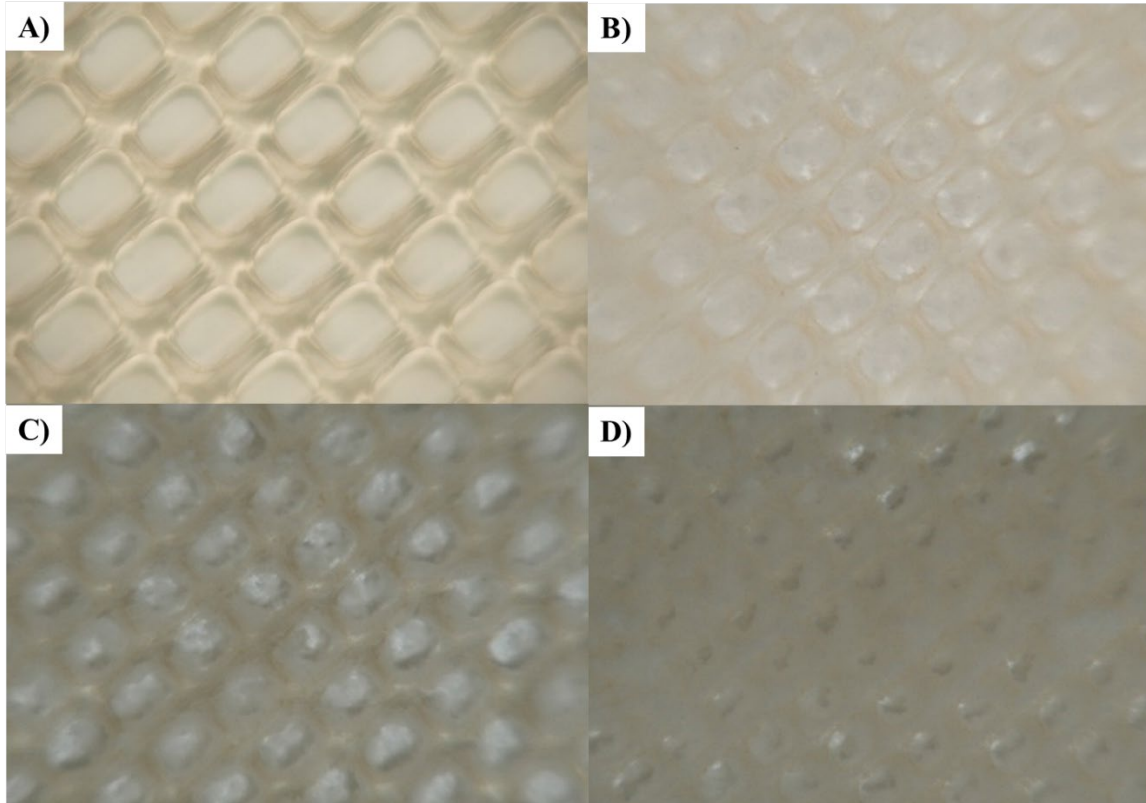


Figure 4.9 Mesh feed spacer scaling in transparent crossflow cell with extensive nucleation, growth and deposition on spacer.

Using the same setup a modified membrane was run under the same scaling conditions. Figure 4.10 B. shows initial scale formation starting to occur around the micromixers themselves. This was followed by continued deposition around the micromixers and deposition occurring in small amounts in the channel, too. The last picture Figure 4.10 D. shows more scale deposition has occurred but not in significant amounts as seen with the unmodified membrane utilizing the 0.508 mm mesh feed spacer.

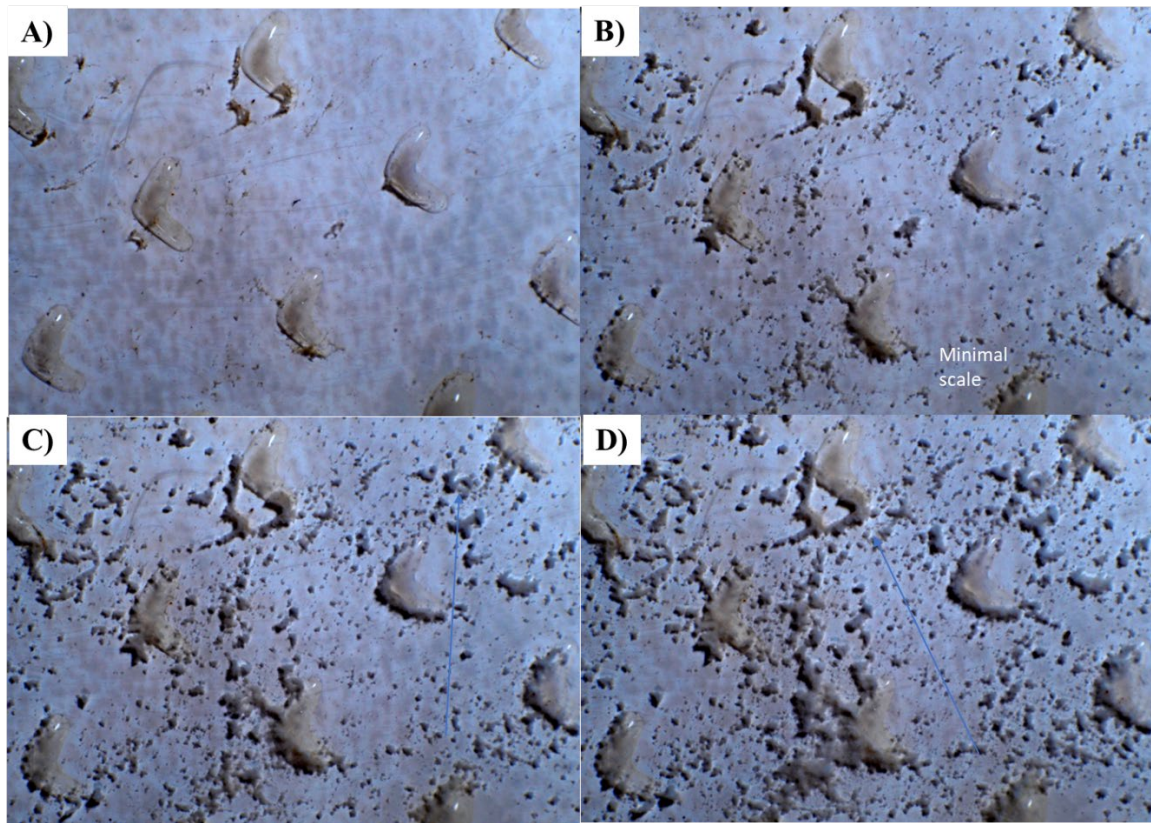


Figure 4.10 The modified membrane with scaling in transparent crossflow cell showing minimal nucleation, growth and deposition.

4.4.0 Discussion

Successful printing required a balance between the viscosity of the epoxy, the pressure applied to the syringe to get the right deposition, the speed of the print head, the intensity of the UV LEDs for curing, and the needle bore hole that the epoxy was dispensed from to ensure a successful print. Even with these optimized, continuous monitoring of the print process had to be done in real time to ensure the epoxy did not cure to the needle and cause blockage. During the period that the print head was in the air tweezers had to be

used occasionally to remove any buildup of epoxy that was starting to set too ensure uniform printing occurred.

Since the pure water flux is based on DI water with no concentration polarization effects the fluxes should be close for the modified and unmodified membranes if there was no damage to the membranes. Based on the modified membrane samples having an average salt rejection within .05% of the unmodified membranes, and both within 3% of the membrane manufacturers specifications it was determined no membrane damage was present. The printing process itself should not cause an increase in flux while maintaining the same salt rejection characteristics. This means the flux calculated based on subtracting the physical dimensions of the chevrons observed described in section 4.3.2 was inflated. The effective active membrane area was recalculated using the average pure water flux from the unmodified membranes (see appendix A). This showed that the active membrane area was actually 120 cm² for the modified membranes instead of 88 cm². The fluxes using this active membrane area were seen in Figure 3. This shed insight into the permeability of the epoxy material or the depth of the cross linking and impact on the diffusive layer of the membrane when put through the 3D printing process. In fact 32 cm² of the chevron area that shows as physically impacting the active membrane area actually allows diffusion through. This means that the printing process itself can be optimized to ensure the micromixers are bonded to the surface while minimizing the impact on the active membrane area.

During the scaling experiments there were two clear differences in scale development. The first, both the modified and unmodified membranes with the mesh

spacer showed similar flux decline when the scaling solution was introduced and flux was reduced based on the increase in ionic strength while operating at constant pressure. After approximately 5 hours of equilibration a sharp decline in flux for both sets of membranes was observed due to the solubility limit of the calcium sulfate being exceeded at the boundary layer and the onset of bulk precipitation of scale starting to occur and deposit on the membrane surface. This was followed by a 2 hour period of equilibrium, stabilized flux where the hydrodynamics of the feed channel prevented additional deposition of scale on the surface and flux decline for both the modified and unmodified membrane. So in totality of the scaling test both membranes behaved closely in relationship to their flux decline for the first ten hours. At this point the second development of scale occurs primarily for the unmodified membrane with the mesh feed spacer.

The flux drops consistently over the next 12 hours, a total of 78% due to the bulk scaling setting up on the mesh spacer and depositing in a cake like fashion from the filaments outward into the open space until the mesh spacer is completely filled. The modified membrane at this point drops minimal; a total of 24% in flux due to the improved hydrodynamic open channel flow created by the individual micromixers that minimized the scale deposition and impact on flux. This showed that individual micromixers printed directly onto a membrane surface will maintain flux longer compared to a standard feed spacer when exposed to a high scaling solution.

Neither the printed and industry standard feed spacer experienced surface initiated crystallization as can be seen by Figures 4.6 to 4.8, all scale was bulk crystallization which initiated at the boundary layer interface where the calcium sulfate became supersaturated

and deposited on the membrane and feed spacer. The ability of the printed micromixers to minimize scale deposition on the membrane surface and the feed channel over the mesh spacer during the scaling experiments was pronounced and supported by the optical images and SEM analysis of the membranes shown in Figures 4.6 to 4.8.

The development of scale formation by the modified and unmodified membranes was further explained by the scaling experiments conducted with the transparent cell under the same experimental conditions. Both membrane variations showed similar surface scale setup followed by minimal scale formation over the length of the experiment for the modified membrane. The unmodified membrane however after the initial surface scale deposition had extensive scale formation on the mesh feed spacer itself as can be seen in Figure 4.9 C. This picture also shows the open area between the scaled filaments that allow visualization down to the membrane surface itself showing similar scale deposition as seen in Figure 4.9 B. Supporting that after the initial surface deposition minimal surface accumulation occurs and instead the focus of the scale deposition is the mesh feed spacer itself. This latticed framework of scaling becomes so pronounced that sections of the feed channel and membrane become blocked with scale. The heavy cake formation caused by the mesh feed spacer lead to the rapid flux decline seen by the unmodified membrane but not the printed due to the open channel flow with the enhanced velocity profile.

4.5.0 Conclusion

Laboratory experiments were used to evaluate whether an enhanced design and pattern of individual micromixers printed directly onto the membrane surface in place of a feed spacer were able to maintain flux longer when treating a scaling water compared to a

standard mesh feed spacer. The results are consistent with the original hypothesis tested. The enhanced design and pattern of the micromixer minimized scaling in the feed channel relative to a standard mesh feed spacer. This was supported by the SEM images and the scaling experiments conducted in the transparent cell that showed extensive cake formation of scale on the unmodified membrane and feed spacer compared to the minimal deposition on the modified membrane. The enhanced design and pattern of the membrane with the printed micromixer was also able to maintain flux longer when treating water with a high scaling potential relative to an unmodified membrane operating with a standard mesh feed spacer. In fact the flux for the membrane with the mesh feed spacer dropped by 78% compared to the membrane with the printed micromixers which only dropped by 24%.

CHAPTER 5: REVERSE FLOW FEATURE OF MICROMIXER FOR ENHANCE CLEANING

5.1 INTRODUCTION

Reverse osmosis (RO) membrane fouling has been the Achilles heel to membrane operations since their inception whether it is treating seawater, brackish water, fresh water, process water or wastewater. To maintain flux and prevent fouling extensive and varied pretreatment approaches have been implemented. All different types and configurations of membranes and pretreatment processes in front of RO membranes such as microfiltration or ultrafiltration or even both have been employed. Regardless of these focused efforts to minimize fouling and the precursors that lead to fouling, eventually some type of fouling still occurs (Mulder 1991). Fouling is defined in the EPA's membrane filtration guidance manual as the gradual accumulation of contaminants on a membrane surface or within a porous membrane structure that inhibits the passage of water, thus decreasing productivity (EPA 2005). With fouling essentially inevitable, treatment operators keep daily logs of parameters used to monitor membrane operations providing insight into what type of fouling is occurring and how to tackle it. The typical design of a spiral-wound element (SWE) does not incorporate the ability to reverse flow the feed water as a cleaning method or even reverse operations. In fact there is a brine seal on the feed side of the element that in normal operations forces all water through the feed side of the element. For these systems, membrane fouling is controlled primarily with chemical cleaning, as well as by recovery and crossflow velocity which is set based on feed water quality into the RO train.

The recorded operator data is compared to membrane manufacturers recommend cleaning parameters such as when normalized permeate flow drops by 10% or normalized salt content of the product water increases by 10% or the differential pressure increases by 15% from the established baseline (Solutions 2010) Obviously, this only gives a slight insight into what type of fouling is occurring and further water quality analysis is needed and possible even a membrane autopsy, Figure 5.1 might need to be performed to determine exactly what type of fouling is present and what needs to be done to control its impact on water production and membrane life.

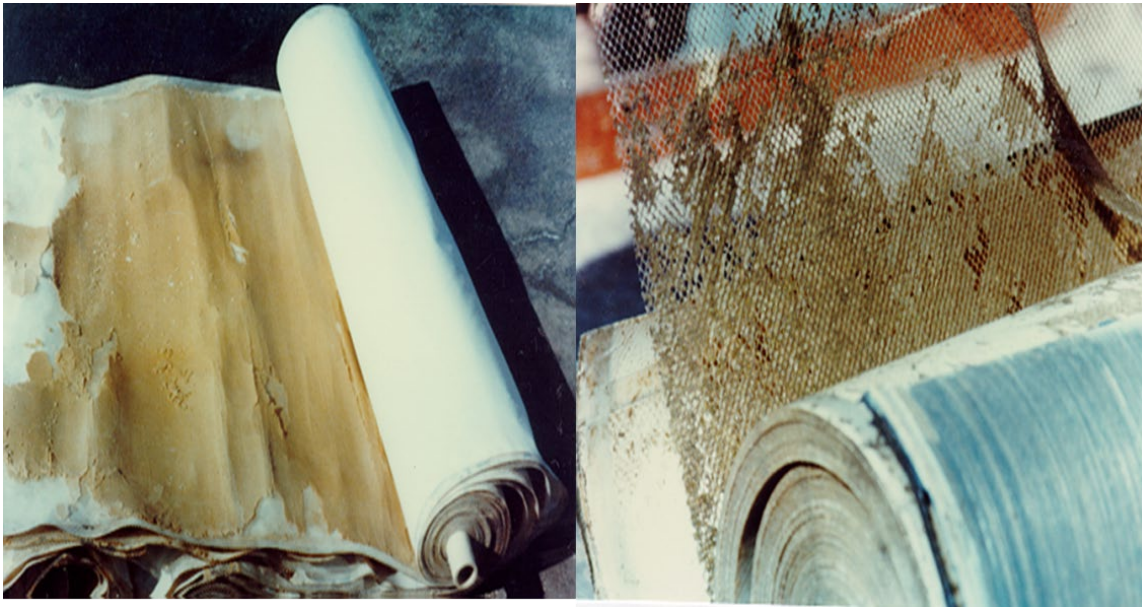


Figure 5.1 Fouled spiral wound reverse osmosis element (TARDEC 1998).

Membrane manufacturers identify different cleaning protocols depending on the foulant of concern. Dow Filmtec breaks their cleaning strategy into four categories utilizing the following chemicals to clean the identified foulant from the membrane element. Inorganic Salts using a .2% HCl or 2% citric acid solution, metal oxides using a

0.5% H_2PO_4 or 1% $\text{Na}_2\text{S}_2\text{O}_4$ solution, inorganic colloid using a 0.1 % NaOH and pH 12 and a silica or biofilm using a 0.1% NaOH and pH 12 at 30 degrees (Solutions 2010). While other membrane manufacturer breaks foulants into varied categories of foulants. Such as calcium compounds, sulphate compounds, Fe, metal oxides recommending cleaning with a low pH such as citric acid and silts, colloids, gelatinous polysaccharides substances and insoluble substances to be removed using a high pH NaOH and organic acids, oils, proteins, waxes, cellulotics, and paraffins using a detergent. Not only is it important to identify the correct foulant and cleaner it is important to make sure that cleaning is carried out in the right order when multiple foulants are present. Exposing fouled membranes to the wrong cleaner in the wrong order can cause irreversible fouling (Paul 1990; Ho and Kamalesh 2012; Solution 2010)

Once the correct cleaners are identified a typical cleaning regime might be to operate at 50% of feed flow to allow for breakup of fouling then operate at 100% of feed flow, both for 10 to 15 min with filter in place to ensure foulants are not reintroduced. Then circulate at 150% of the feed flow but not to exceed the feed pressure and pressure drop specified by the membrane manufacturer. Followed by a 1 hour soak and then recirculate cleaning solution for 15-60 min at high flow (Hydranautics 2016). This obviously represents a significant downtime, labor requirement, and chemical cost not to mention most membranes fail to return back to baseline flux and slowly degrade until they have to be replaced.

To combat fouling most research and development efforts to date have focused on pretreatment of the feed water, modifying the surface properties of the membrane, new

membranes and novel cleaning solutions. As stated in Chapter 2, other efforts such as surface modification of the membrane, new feed spacer designs, and printing directly on the membrane surface were tried with limited success (Suwarno et al. 2012; Picioreanu et al. 2009; Koutsou et al. 2007; Vrouwenvelder et al. 2006; Vrouwenvelder et al. 2009; and Radu et al. 2010). While some researchers have delved into spacer modification as described in the preceding Chapter all of these efforts have been to minimize the onset of fouling versus designing the feed spacer geometry to be impactful in a reverse flow cleaning regime. With this focus, one hypothesis was evaluated: 1) during flow reversal, printed micromixers will create hydrodynamic conditions that enhance scale removal.

5.2. Material and Methods

5.2.1 Model Description

COMSOL Multiphysics 5.0 (COMSOL Inc., Burlington, MA) was used to model the feed of channel of a RO SWE utilizing the enhanced microstructure geometry and patterning developed and tested in the previous two chapters with different reverse flow rates typical of forward flow cleaning. While the previous design was tailored to enhancing the forward fluid flow regime in the channel between 0.2 m/s and 0.3m/s, the enhanced zone with an inlet flow velocity of 0.104 m/s. The same features with the flow in the opposite direction were evaluated to determine the benefit of removing fouling from the membrane surface and feed channel. This was based on modeling different flowrates that are currently recommended by membrane manufactures when cleaning with chemicals in forward flow. Flow velocities were based on 0.25 LPM, 0.5 LPM (the normal flowrate that the experiments were run at) and 0.75 LPM.

5.2.2 Geometry Optimization

The channel was modeled with thirteen micromixers using the offset pattern to ensure the fluid flow profile being examined was a true representation of the impact of a repeating pattern and not impacted by the boundary conditions of the side walls. The area examined for interpolation of the velocity profile included the centered micromixer slicing through the surrounding fluid flow path to capture a section of non-repeating flow. This was to ensure the velocity profile could be compared for the different flowrates by percent coverage of an individual micromixer unit area.

5.2.3 Simulation conditions

As with the previous base model, the Navier-Stokes and continuity equations assuming Newtonian incompressible fluid were used for the flow modeling. The boundary conditions applied were the right channel wall was the inlet with the inlet flow velocity defined for a cleaning/backflush regime. The left channel wall was the exit with the outlet pressure set to the inlet pressure. The remaining structure walls were all set to no slip wall boundaries.

5.2.4 Materials

Commercial flat sheet RO membranes, SW30XLE manufactured by Dow Filmtec (Dow Chemical Co., Midland, MI) and procured through Sterlitech (Kent, WA) were used in this study. UV curable epoxy, UV15TK (Masterbond, Hackensack, NJ) was used for printing features on the membrane. Solutions were prepared using de-ionized water, ACS grade sodium chloride (NaCl) and sodium sulfate (Na_2SO_4) purchased from Sigma Aldrich (St. Louis, MO) and ACS grade calcium chloride ($\text{CaCl}_2 \cdot 2\text{H}_2\text{O}$) from LabChem.

Fluorescent dragon green 1.9 μm diameter styrene beads were purchased from Bangs Laboratories (Fishers, IN) and refrigerated until ready for use.

5.2.5 Printer

A modified 3D printer BioBots 1 (BioBots, Philadelphia, PA) was used to print stabilized micromixers directly on the surface of a membrane without needing any additional processing steps. This included an integrated UV 365 nm LED light for curing while printing and a larger print platform to be able to print on the entire active membrane area utilized by the cell, 140 cm^2 without moving the membrane swatch. The down selected enhanced micromixer and pattern based on the computational fluid dynamic (CFD) modeling was printed directly on the surface of the thin film composite polyamide RO membrane.

5.2.6 Low pressure transparent membrane cross flow cell system

The same test apparatus described in Chapter 3.2.8 was used to conduct image flow analysis using florescent micro beads, showing the fluid flow profile around the microstructure. Once the flux was determined to be constant fluorescent dragon green 1.9 μm diameter styrene beads were injected using a syringe pump that was plumbed at the inlet of the high pressure pump. The transparent cell was under a Nikon SMZ-18 stereo microscope (Nikon Melville, NY) and used to take pictures and video of the fluid flow profile around the chevron.

5.2.7 Optical Assessment of Scale Formation

To visually assess the formation of reverse flow cleaning, a fouling experiment was carried out in a low pressure transparent acrylic cross flow cell (Sterlitech, Kent, WA). The

acrylic cell had an effective membrane surface area of 140 cm². The cell channel depth was 0.8636 mm (34 mil) so acrylic shims were used to achieve the 0.508 mm (20 mil) feed channel height of the printed feed spacer and low foulant feed spacer. The same experimental setup (i.e. polypropylene feed tank (16 Liters), pump (Hydra-Cell model F20K52GSNEM, Wanner Engineering, Minneapolis, MN) backpressure reducing valve (Model BPH05-02T, Straval, Elmwood Park, NJ) described previously were also used for the optical experiments. A digital color camera DS-Fi3 5.9 megapixel (Nikon Melville, NY) was utilized to take photos and time lapse imaging every 10 seconds to show scale removal in real time and be visually documented.

5.3. Results

5.3.1 Velocity profile

The enhanced geometry of the micromixer and pattern developed in Chapter three and successfully tested in Chapter four under laboratory conditions to demonstrate a reduced scaling in the feed channel relative to a standard feed spacer was utilized. The enhancement provided the most coverage in the 0.2 m/s to 0.3 m/s range for forward flow, based on an inlet velocity, 0.104 m/s; further modeling was conducted in the reverse flow as a cleaning mechanism for scaling. Since a normal cleaning strategy utilizes lower and higher flowrates to remove foulants, three reverse inlet velocities were chosen to model. One at 0.104 m/s the velocity utilized during normal operations in forward flow. Along with 0.52 m/s which is half the normal flow velocity and then 0.156 m/s which is 1.5 times the normal flow velocity. The reverse flow modeled at the same inlet velocity and flow conditions developed the same open channel continuous velocity profile; figure 2 B., as

seen in the forward flow velocity profile. Reducing the inlet velocity by half created the same continuous channeled velocity profile but with a reduced velocity profile primarily in the light blue range, 0.5 to 1.5 m/s range as can be seen in figure 5.2 A. With the inlet velocity increased to 0.156 m/s the velocity profile maintained continuous open channel flow in the dark red zone, velocities greater than 0.25 m/s.

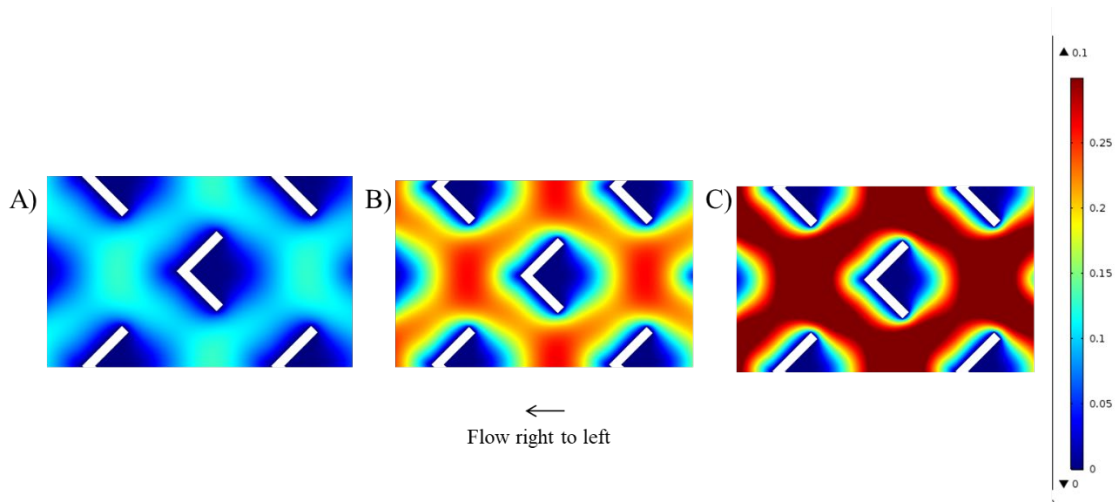


Figure 5.2. Full velocity profile from 0 to 0.3 m/s showing influence of different reverse flow velocities: A) 0.052 m/s B) 0.104 m/s C) 0.156 m/s on the amount of open channel flow and velocity regions with the optimal design pattern: 90 degree, offset, 3mm chevron length, and 5.75 mm gap.

5.3.2 Fluid flow profile

The fluid flow profile coverage for the enhanced geometry and pattern were very similar in forward flow and reverse flow as can be seen in figure 5.3 A. and B. The velocity range was changed to have a lower limit of 0.001 m/s to eliminate some random directional arrows. This <0.001 m/s velocity zone was then replaced with the red arrows showing the corrected flow direction based on carrying the flow vectors modeled into the chevron. Both

flow directions provided similar velocity flow vectors except they were in the opposite direction. The major difference was the flow behind the micromixers themselves; the fluid flow profile for the reverse flow drove into the middle of the backside of the chevron and then swept outward and around to the front. The flow profile in the forward direction drove into the tip of the chevron splitting the flow around the chevron and then curving around into the backside of the chevron where the two flow streams meet and flow back into the feed channel.

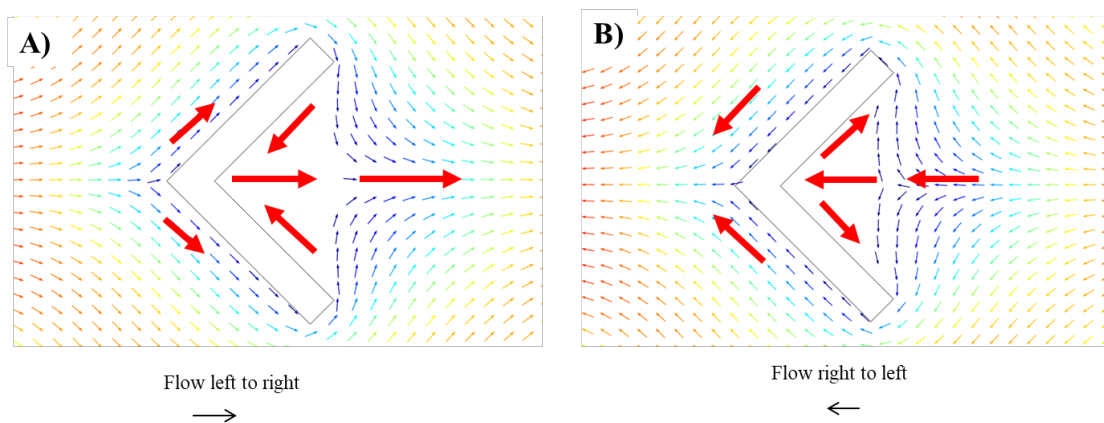


Figure 5.3. Full fluid flow profile for a feed velocity of 0.104 m/s A) forward flow B) reverse flow both with an offset pattern, 3mm chevron length, and 5.75 mm gap, and 90 degrees.

5.3.3 Fluorescence Imaging

A modified membrane with the enhanced micromixer and pattern were placed into an acrylic transparent crossflow cell for fluid flow visualization. A membrane swatch was run for 24 hours to ensure compaction and equilibration at the proper flowrate to achieve the inlet velocity, 0.104 m/s. Once the flowrate was established fluorescence beads were introduced and videos and pictures were taken, figure 5.4 A. and B. that showed the

forward flow CFD modeling matched the bead flow under actual operating conditions. Specifically, the flow portion at the bottom of the chevron flowing in and back out at the center point behind the micromixer. The picture also verified through the fluid flow imaging an unhindered flow path while the mesh spacer modeled extensively by other researchers () shows a fluid flow profile traversing up and down the feed channel due to the filaments obstructing the flow and contact points with the membrane. Previous researchers modeled flow depictions were verified using the transparent flow through cell and fluorescent beads video available at <https://doi.org/10.6084/m9.figshare.7312337.v1> with beads sometimes catching and adhering to the filament.

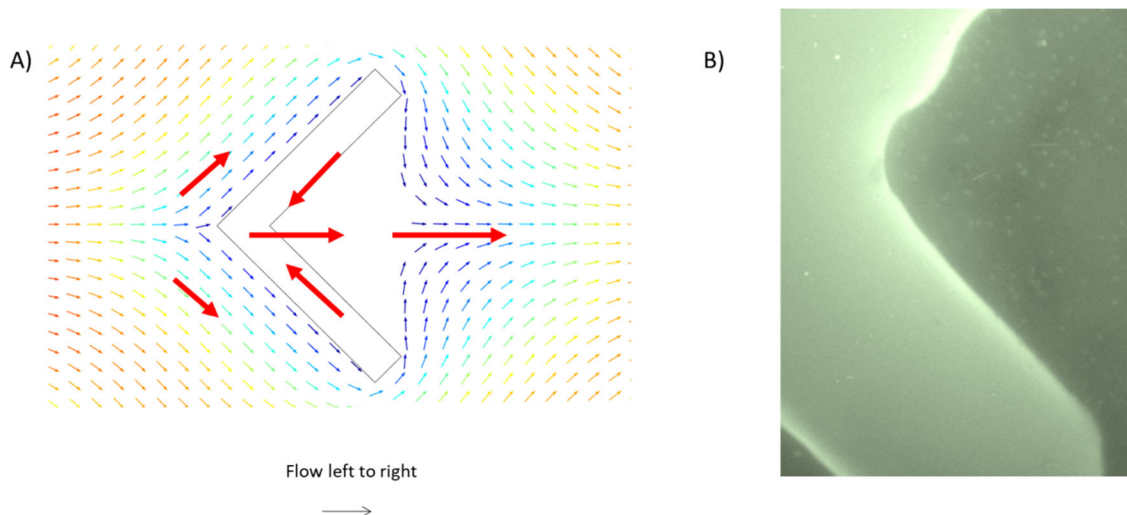


Figure 5.4 Full fluid flow profile for feed velocity of 0.104 m/s A) forward flow with offset pattern, 3mm chevron length, 5.75 mm gap and 90 degree B) video of fluorescence imaging bead flow profile (available at <https://doi.org/10.6084/m9.figshare.7309148.v1>) Figure 5.5 A. and B. show that the reverse flow model developed was supported by the optical imaging of the bead flow in reverse in the feed channel. The bead flow goes into

the back of the chevron and the splits and flows around coming back into one flow path at the chevron tip.

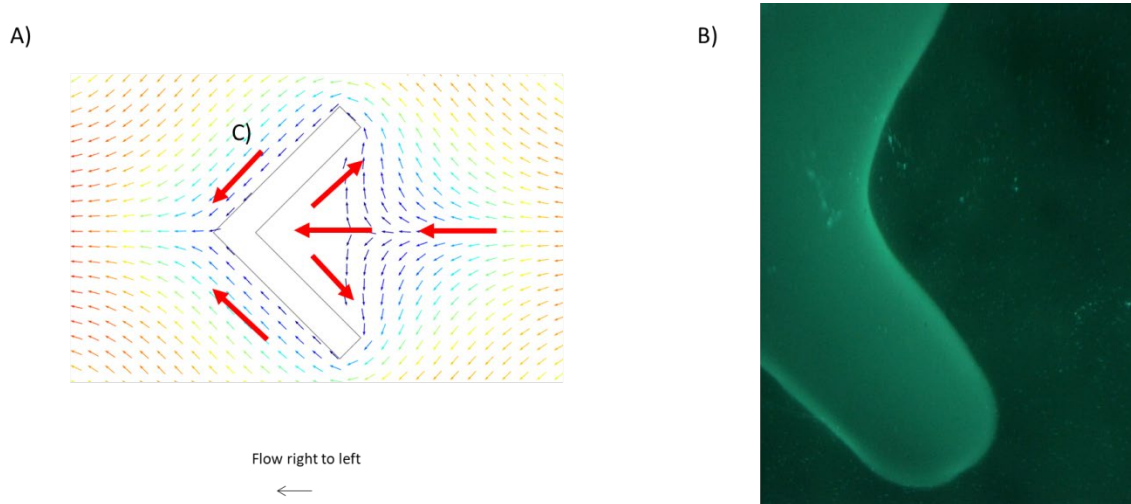


Figure 5.5 Full fluid flow profile for feed velocity of 0.104 m/s A) reverse flow with offset pattern, 3mm chevron length, 5.75 mm gap and 90 degree B) video of fluorescence imaging bead flow profile (available at <https://doi.org/10.6084/m9.figshare.7309220.v1>)

The reverse flow was shown with fluorescent bead streaking depicted with the red arrows in Figure 5.6.

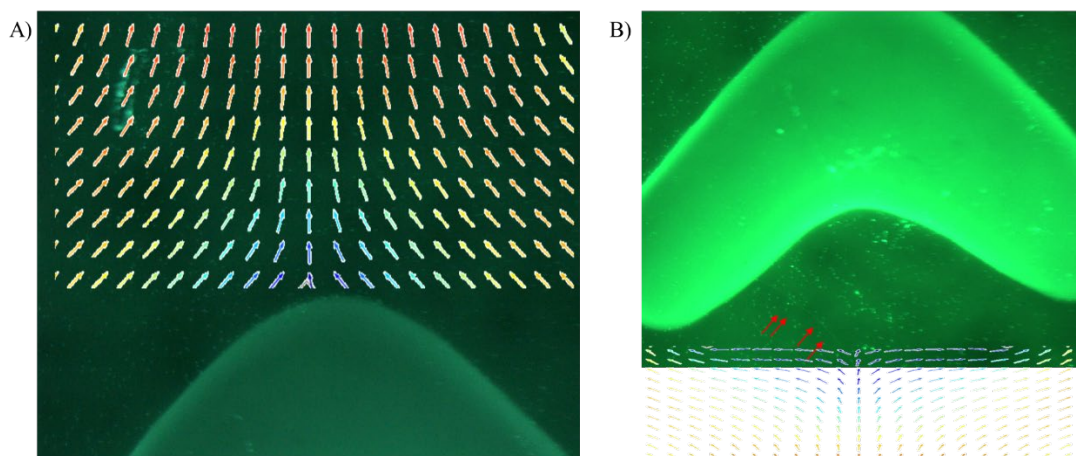


Figure 5.6 Fluorescence imaging bead flow profile for A) top and B) bottom of chevron with a feed velocity of 0.104 m/s. Reverse flow with an offset pattern, 3mm chevron length, 5.75 mm gap and an angle of 90 degrees.

5.3.4 Scale formation and removal

A transparent crossflow cell with a modified RO membrane was run using the same scaling experiments previously described in Chapter 4. At the end of the experiment the scaling solution was removed and replaced with DI water, Figure 5.7 A. The picture depiction shows that the majority of the scale over a five minute period was washed away from the membrane surface reaching a point where there was minimal scale present and the reverse flush was no longer removing what was left. Some scale appears lodged in the backside of the chevron in the last picture, Figure 5.7 D. The reverse clean was followed

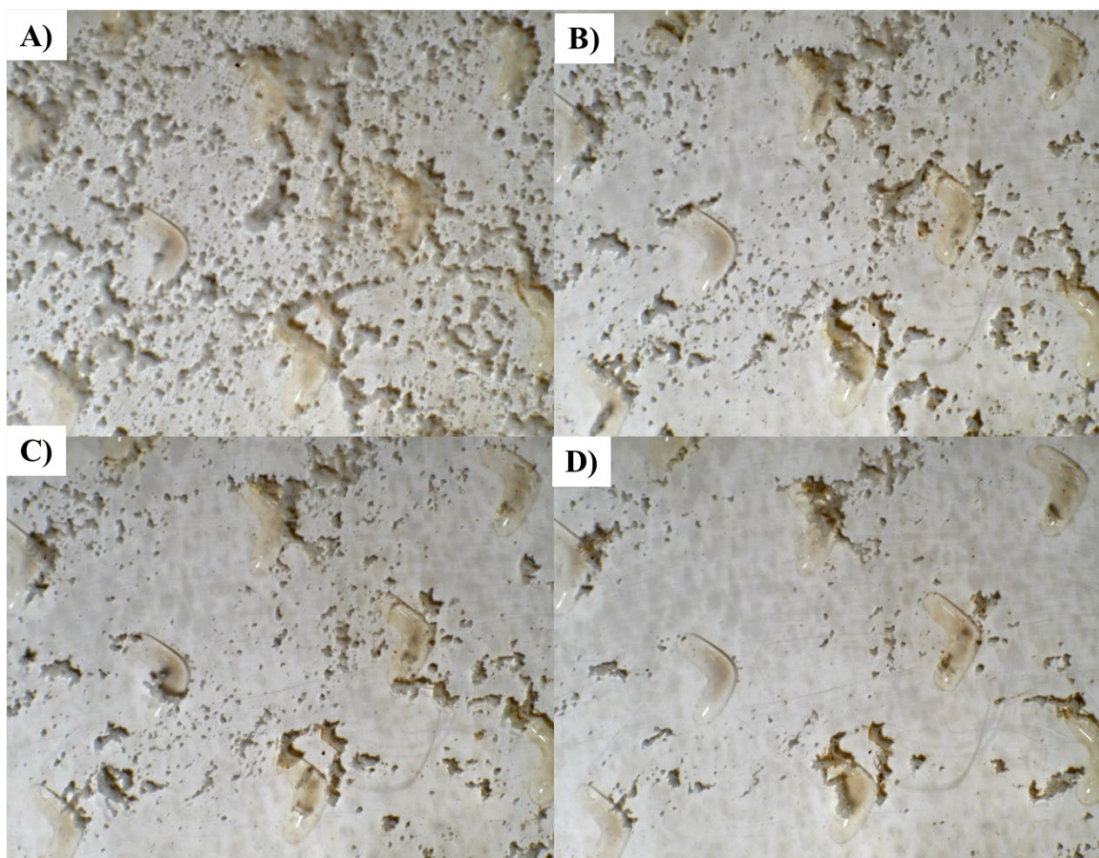


Figure 5.7 Reverse flow effectively removed scale A) membrane scale after 24 hour scaling experiment (video available at <https://doi.org/10.6084/m9.figshare.7309208.v1>) (B) reverse flow remove the majority of the scale C) minimal scale left for removal D) reverse flow cleaning after five minutes the majority of the scale was removed (video available at <https://doi.org/10.6084/m9.figshare.7309211.v1>).

by the flow being changed back to normal operations which removed the remainder of scale as can be seen in Figure 5.8 B. through the open channel flow hydrodynamics established by the individual micromixers.

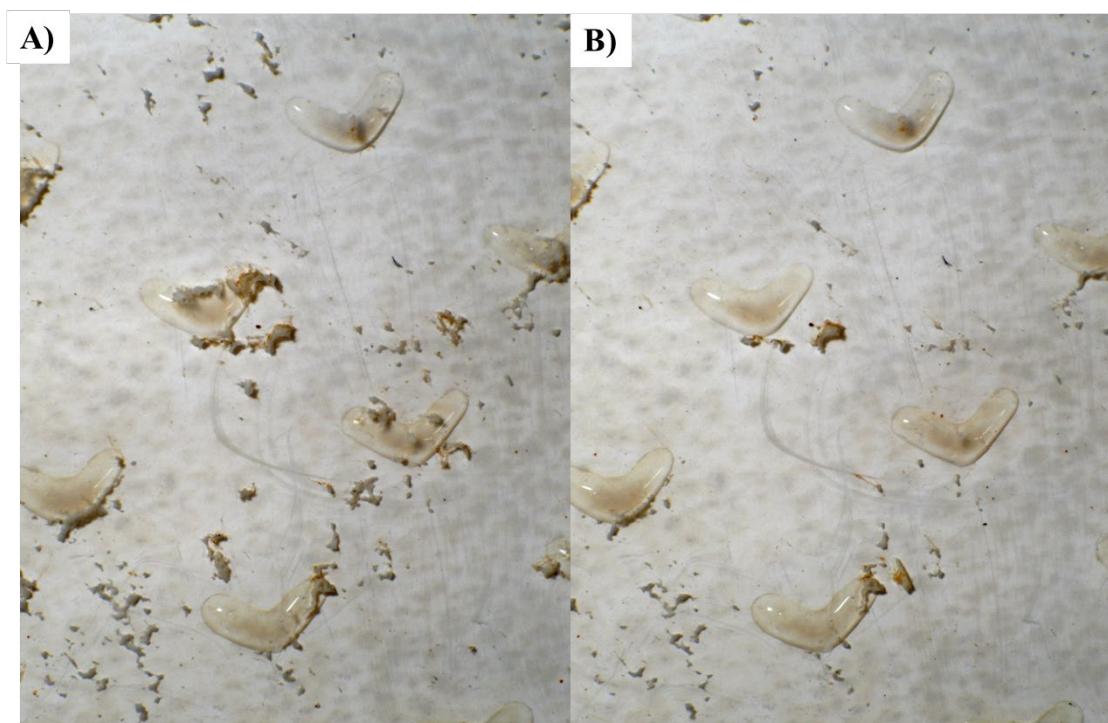


Figure 5.8 Return to normal forward flow effectively removing remaining scale A) membrane scale after five minutes of reverse flow B) minimal scale left after forward flow for 30 seconds.

5.3.5 Water quality of reverse clean

After the scaling experiments were conducted water samples were taken at the onset of the reverse flow cleaning. After five minutes of cleaning another sample was taken again and the system was shut down and piping was switched back to forward flow. The system was started again and another sample was captured. The samples were analyzed for sodium, chloride, calcium and sulfate. As can be seen in Figure 5.9, three different runs with the samples averaged versus the unmodified membranes operated with a mesh feed spacer showed no discernable difference in water quality of reject samples. At the end of the reverse flush and after the return to normal flow modified and unmodified water samples

also showed no significance between the reverse flush and the forward flush. However, at the end of the experiments there was significantly more scale present on the unmodified membranes and mesh feed spacer versus the modified membranes. The SEM images in Chapter 4 showing the top view and side profile of the difference in scale support previous researchers statements that the structure of the mesh feed spacer that causes fouling to occur creates issues in dislodging and removing the entrapped foulants when cleaning (Riley and Milstead 1992). This further demonstrated the enhanced hydrodynamics created by the individual micromixers and open channels of the modified membranes to remove fouling during reverse flow compared to the regular membrane operated with a mesh feed spacer.

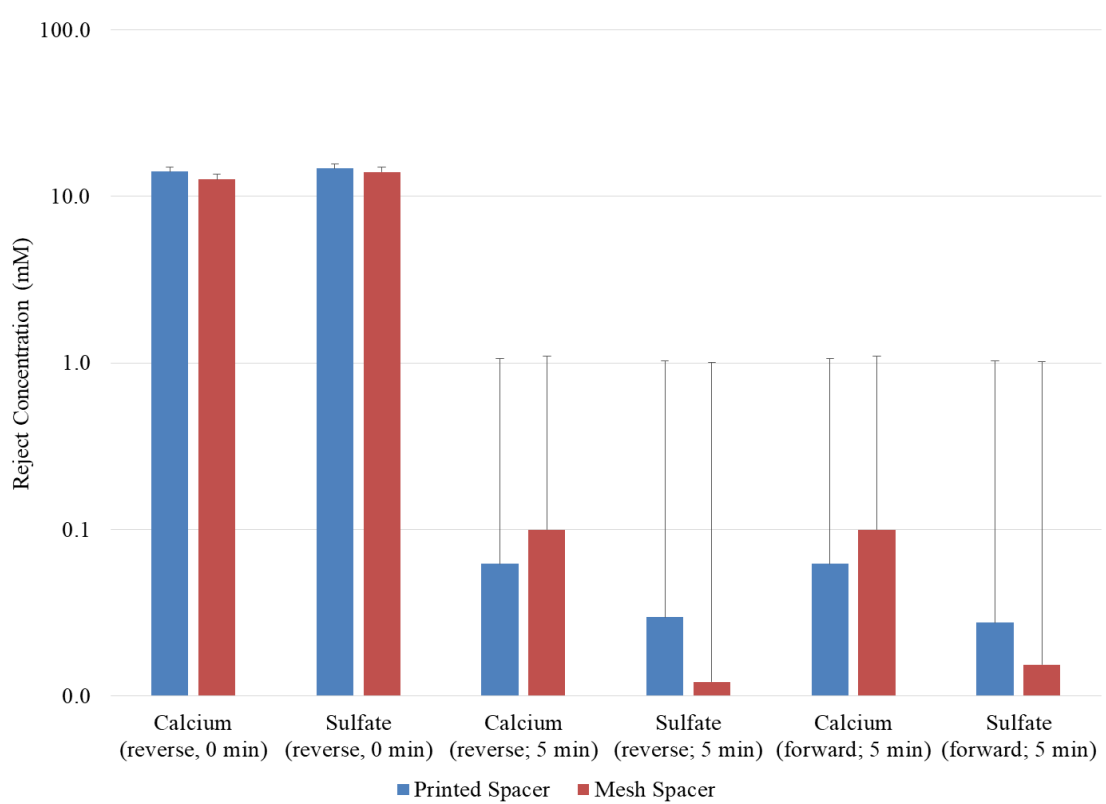


Figure 5.9. Average water quality data for 3 modified and 3 unmodified membranes during reverse flow cleaning after membranes were scaled. At start of reverse flush water sample, time zero, showed no difference for calcium sulfate removal. Samples after 5 minutes of reverse flow and followed by return to normal operations also showed no significant difference.

5.4. Discussion

5.4.1 Velocity profile

At the reduced flowrate there was a continuous unimpeded velocity profile in the channels adjacent to the micromixers in reverse flow that should allow for the gentle breakup and reduction of any fouling buildup. This flow followed by increasing to the normal flowrate showed the same optimal velocity range develop as the velocity profile in the forward flow at his inlet velocity. Running in reverse flow at this velocity should continue to move disrupted foulants from the feed channel. Following these two flowrates with an increase to 150% of the normal operating flow drives the feed channel velocity up by over a factor of 2 pushing the open channel closer to the micromixers reducing the low/no flow zones. While exceeding a velocity of 0.3 m/s has been shown to create non-recirculating zones prone to fouling during normal membrane operations and not beneficial during extended operations. The modeling shows a continuous uninterrupted flow channel which at high temporary velocities would create a localized scouring effect to aid in removing foulants. This reverse cleaning regime has the ability to either replace a chemical cleaning cycle or be used to augment if needed.

5.4.2 Fluid flow profile

The importance of these fluid flow paths lies in the fact that the micromixers themselves were identified through the modeling to be in no/low flow zones which means potential for foulants to build up around them. Being able to change the flow path to the opposite direction allows the disruption or dislodging of foulants or potential foulants before they take hold and cause irreversible fouling. For example it has been shown that biofouling builds up with streamers behind the structures and particulate buildup is in front of the structure (Ngene 2010). With these two types of fouling a directional change with a higher flowrate should aid in dislodging the foulant and sending them into the open flow channel and out the reject side of the spiral wound feed channel out to waste.

5.4.3 Scale formation and removal

Visual scale formation was evaluated using an acrylic transparent crossflow cell for both a modified and unmodified membrane with a 20 mil mesh feed spacer. The time lapse imagery showed scale deposition start on the membrane surface, then the feed spacer with continued cake growth building out from the feed spacer. The field of view showed visualization of the center of the spacer down to the membrane surface elucidating that while the onset was the solubility being exceeded at the boundary layer the primary nucleation and deposition of the cake scaling formation was on the mesh feed spacer. The modified membrane showed some scale deposition around the micromixers and in the feed channel but was minimal compared to the scaling of the mesh spacer on the unmodified membrane. Reverse flushing of the modified membrane showed removal of the majority of scale at the first pulse but reached a point where there was no gain from continued

flushing. The return back to normal flow removed some residual foulant at onset of flow and then was in equilibrium with whatever foulants were left.

5.5 Conclusion

CFD modeling was used to evaluate different reverse flow velocities impact on an enhanced microstructure geometry and pattern. The focus was to determine the impact on the hydrodynamic conditions representative of a SWE feed channel. Reversing the feed velocity showed it was possible to minimize the area of no/low flow velocity in a reverse flow clean. Laboratory experiments in a transparent crossflow cell using fluorescence imaging of 1.9 μm beads supported the modeling based on the fluid flow visualization showing the same as the modeling. The same setup was used to show scale formation with the printed membrane and the unmodified membrane with the mesh feed spacer. The optimized individual micromixer design and patterning created unhindered feed channels that when operated in the reverse flow with an enhanced velocity flushed the foulants away. The results were consistent with the hypothesis 1) during flow reversal, printed micromixers will create hydrodynamic conditions that enhance scale removal.

CHAPTER 6: SIGNIFICANCE & CONCLUSIONS

This dissertation focused on developing a novel method for separating reverse osmosis (RO) membrane leaves in spiral wound elements (SWEs) by printing micromixers directly onto the membrane surface. COMSOL Multiphysics 3.0 was used to design the enhanced microstructure and pattern for improved feed channel hydrodynamics. A modified BioBots 3-D printer was used to deposit and cure the epoxy, UV15TK to the membrane surface in the modeled microstructure and pattern. The modified membranes intrinsic properties, scaling impact, and cleaning potential were investigated and compared to the unmodified membranes using a diamond mesh feed spacer.

A hydrodynamic model of a RO feed channel without a feed spacer was developed using computational fluid dynamics. Using an inlet flow velocity of 0.104 m/s different chevron micromixer designs were evaluated with the objective to maximize the velocity coverage in the feed channel from 0.2 m/s to 0.3 m/s. This velocity region has been shown to create optimal hydrodynamic conditions in the feed channel for reduced fouling. The modeling was used to minimize the membrane area influenced by channel velocities of <0.1 m/s and >0.3 m/s. These velocity regions have been observed to create localized recirculating zones that cause foulant deposition and accumulation (Amokrane et al. 2015; Bucs et al. 2015; Koutsou et al. 2007). The channel was modeled with 9 to 17 micromixers to ensure the fluid flow profile accurately depicted the impact of the specific micromixer geometry and pattern being evaluated and was not influenced by the boundary conditions selected for the side walls. The area of quantification was centered on the middle chevron and included the surrounding areas (Figure 3.3), ensuring a representative unit area for

velocity profiles were compared for different design configurations. This approach made it possible to quantify feed channel velocity profiles due to changes in micromixer geometry. The approach taken was an advancement over previous research which was limited by a small number of structures analyzed and artifacts from boundary conditions. Based on this study, a 90-degree chevron with 3 mm length sides distributed in an offset pattern with a gap length of 5.75 mm was found to be optimal. This design provided the largest amount of enhanced velocity coverage (39.2% of area) with unhindered flow paths and a minimal combined fouling region (21.9% of area).

A desktop 3-D printer was modified to print the enhanced micromixer design directly onto the surface of a thin-film composite polyamide RO membrane. Based on available literature surveyed this is the first report of a desktop 3-D printer being used to print functional, individual micromixers directly to a membrane surface without damaging it. Ho et al. (2008) and Altman et al. (2010) reported a manual two-step process that created a repeating continuous pattern with no ability to make isolated structures on the membrane surface. This significant achievement demonstrates a wide-array of micromixers can be modeled, printed and evaluated under realistic condition of membrane operations. This is a major advancement over previous research which had only theoretically demonstrated potential flow conditions or used stereolithography on glass plates to evaluate individual microstructures.

Laboratory experiments utilizing fluorescent styrene beads were used to validate fluid flow profiles generated from the theoretical models. The modified membranes were operated in a transparent crossflow cell using the same flow conditions modeled using

CFD. Flow paths illuminated by fluorescent beads showed continuous channel flow and flow around the chevrons with no recirculating zones. The fluorescent imaging of the feed channel flow provided confirmation of the feed flow pattern predicted by the CFD models. This is the first-time laboratory trials using fluorescent beads have confirmed CFD model predictions of complex 3-D printed membrane structures.

Modified membranes were characterized for pure water flux and salt rejection in accordance with the membrane manufactures specifications. The average salt rejection and flux for printed membranes were statistically indistinguishable ($\pm 3\%$ standard deviation) from unmodified membranes, within the range specified by manufacturers. Based on the rejection and the flux the membrane swatches were not damaged by the printing process.

Once the membrane flux and salt rejection were verified to be within the correct ranges scaling experiments were initiated by adding calcium chloride and sodium sulfate solutions to make a 0.03 M scaling feed solution. The flux dropped similarly for both the printed membranes and unmodified membranes operating with the standard feed spacers. Four hours after introducing the scaling solution, the flux declined again for both the modified and unmodified membranes indicating the onset of bulk scale formation. This scale was found to be calcium sulfate precipitate forming in the boundary layer and depositing on the membrane surface. Once bulk scale formed there was a significant difference in scale buildup and flux decline as the runs continued between the membranes. The unmodified membranes with the standard 0.508 mm mesh feed spacer had an average flux decline of 78% while the modified membranes had an average flux decline of 24% over the next fourteen hours. The results are consistent with the hypothesis that the optimal

design and pattern of the micromixer identified through computational modeling, based on hydrodynamics, will minimize scaling relative to a standard feed spacer.

After 24 hours of scaling, reverse flow cleaning was initiated with distilled water at the same flowrate used to run the membranes under normal operating conditions. The first liter of flush water was captured. This was followed by another collection of reverse flush water after five minutes and another sample after operations were returned to normal flow. The samples were analyzed for sodium, chloride, calcium and sulfate. The water quality results showed no significant differences between the modified membranes and the unmodified membranes utilizing the mesh spacer. However, all unmodified membranes with mesh feed spacers showed significantly more scale present than the modified membranes at the end of the experiments. The SEM analysis (Figure 4.8) support this observation. All scale was identified as bulk precipitation, with no surface initiated dihedral scale present. Since there was significantly more scale on the unmodified membrane and spacer that could be removed these results suggest hindered flow paths in the mesh feed spacer likely reduced the removal of scale foulant. While the modified membranes showed minimal scale present after the experiments indicating that the reverse flush worked.

CFD modelling was extended to evaluate the impact of reverse flow cleaning at different feed velocities based on forward flush cleaning protocols. An inlet clean velocity of 0.052 m/s, 0.104 m/s and 0.156 m/s were modeled. The different inlet velocities showed similar velocity profiles in reverse with decreased and increased velocity regimes. Starting with a reverse flow of 0.104 m/s to potentially scour any foulant buildup that might not be

fully adhered to the membrane surface or feed spacer followed by increasing to 0.156 m/s should flush all foulants from the membrane feed channel.

Visual scale formation was evaluated using an acrylic transparent crossflow cell for both a modified and unmodified membrane with a feed spacer. The time-lapse imagery showed scale deposition originating on the membrane surface, then forming on the feed spacer with continued cake growth building out from the feed spacer over time. Visualization of the center of the spacer down to the membrane surface indicated that while scale formation initiates at the boundary layer due to solubility limitations, the majority of the cake scaling formation occurred at the mesh feed spacer with the spacer providing points for nucleation and growth. The modified membrane showed some scale initiation around the micromixers and in the feed channel. This was minimal compared to the scaling of the mesh spacer on the unmodified membrane. Reverse flushing of the modified membrane showed the majority of scale was removed during the first pulse of reverse flow. After the initial flow reversal, the system reached a point where minimal scale removal was observed (i.e. there was no benefit from continued flushing after 5 minutes). Return to normal flow conditions (i.e. forward flow) showed some residual foulant flush from the feed channel during the first one minute only. This suggests pulsing the cleaning solution in the reverse flow direction for a briefly (<5 min) followed by a pulse in normal operations may enhance cleaning of the modified membrane. The results of chemical analyses of flush water (Figure 5.9) are also consistent with this interpretation.

This dissertation demonstrated a proof-of-concept design optimization for the next generation of membrane spacers. The concept of moving away from a material insert as

the separation method for the membrane leaves in a SWE to utilizing micromixers printed directly on the membrane is an important advancement. This important advancement includes the (1) implementation of enhanced chevron micromixers that significantly reduce membrane fouling and (2) the ability to clean using a reverse flush process before irreversible fouling occurs. A development method to print a wide-variety of micromixers directly on the membrane surface in numerous patterns has the potential to create a new class of SWEs. These elements can be optimized to reduce fouling for specific feed water quality conditions. This integrated approach to optimizing feed channels through the use of customizable micromixers provides a major advance in membrane technology that has the potential to reduce the need for pretreatment and maintenance of RO membranes. This is likely to translate into capital and operating cost reductions, ultimately decreasing the cost of providing clean drinking water.

APPENDIX A

$$A_m := 140 \text{ cm}^2 \quad \text{Active Membrane Area} \quad \text{ml} := 10^{-3} \cdot L$$

Note: 1st run is distilled water run through system so osmotic pressure equals zero also run 24 hours at 20.7 bar to compact and stabilize membrane. (product(p), membrane(m), bulk(b))

$$Q_p := 3.8 \frac{\text{ml}}{\text{min}}$$

$$P_f := 20.7 \cdot \text{bar} \quad P_p := 0 \cdot \text{bar} \quad O_m := 0 \cdot \text{bar} \quad O_p := 0 \cdot \text{bar}$$

$$J_w := \frac{Q_p}{A_m} = 16.286 \frac{L}{\text{hr} \cdot \text{m}^2} \quad J_w = 9.593 \frac{\text{gal}}{\text{day} \cdot \text{ft}^2}$$

Flux is Liter/(meter squared * hour) (LMH) or gallons/(feet squared *day) (GFD)

$$A_{\text{purewaterpermeation}} := \frac{J_w}{((P_f - P_p) - (O_m - O_p))} = 0.787 \frac{L}{\text{hr} \cdot \text{bar} \cdot \text{m}^2}$$

Note: 2nd run is 2000 mg/L NaCl solution run through system so osmotic pressure of bulk and product can be determined, flux with boundary layer effects can be measure and concentration at the membrane wall can be calculated to determine salt water transport coefficient.

$$\text{molar mass}_{\text{NaCl}} := 58.443 \cdot \frac{\text{gm}}{\text{mol}} \quad T := 298 \cdot K \quad R = 8.314 \frac{\text{kg} \cdot \text{m}^2}{\text{s}^2 \cdot K \cdot \text{mol}}$$

$$C_b := 2000 \frac{\text{mg}}{L} \quad C_{\text{bmolar}} := \frac{C_b}{\text{molar mass}_{\text{NaCl}}} = 34.221 \frac{\text{mol}}{\text{m}^3} \quad O_b := C_{\text{bmolar}} \cdot R \cdot T = 0.848 \text{ bar}$$

$$C_p := 40 \frac{\text{mg}}{L} \quad C_{\text{pmolar}} := \frac{C_p}{\text{molar mass}_{\text{NaCl}}} = 0.684 \frac{\text{mol}}{\text{m}^3} \quad O_p := C_{\text{pmolar}} \cdot R \cdot T = 0.017 \text{ bar}$$

$$Q_p := 3.4 \frac{\text{ml}}{\text{min}} \quad J_p := \frac{Q_p}{A_m} = 14.571 \frac{L}{\text{hr} \cdot \text{m}^2}$$

$$O_m := - \left(\frac{J_p}{A_{\text{purewaterpermeation}}} \right) + (P_f - P_p) - O_p = 2.162 \text{ bar} \quad t := \frac{J_p}{A_{\text{purewaterpermeation}}} = 18.521 \text{ bar}$$

$$C_{\text{mmolar}} := \frac{O_m}{R \cdot T} = 87.257 \frac{\text{mol}}{\text{m}^3} \quad C_m := C_{\text{mmolar}} \cdot \text{molar mass}_{\text{NaCl}} = 5.1 \frac{\text{gm}}{L}$$

$$\frac{C_m - C_p}{C_b - C_p} = 2.581$$

$$R := \frac{C_b - C_p}{C_b} = 0.98$$

Reynolds number

$$\mu := .104 \cdot \frac{m}{s} \quad \eta := 0.001 \text{ Pa}\cdot s \quad \rho := 988 \frac{kg}{m^3} \quad h := .5 \text{ mm}$$

$$Re_h := \frac{2 \cdot \mu \cdot h \cdot \rho}{\eta} = 102.752$$

$$w := 165 \cdot \text{mm}$$

$$d_h := \frac{2 \cdot w \cdot h}{(w + h)} = 0.997 \text{ mm}$$

$$Re := \frac{\mu \cdot d_h \cdot \rho}{\eta} = 102.442$$

$$V_{Tot} := A_m \cdot h = 7 \text{ cm}^3 \quad V_{sp} := 1 \cdot \text{cm}^3 \quad A_w := \text{cm}^2$$

$$d_{hs} := 4 \cdot \frac{(V_{Tot} - V_{sp})}{A_w} = 24 \text{ cm}$$

$$x := 23 \frac{\text{gal}}{\text{day} \cdot \text{ft}^2} = 39.048 \frac{L}{\text{hr} \cdot \text{m}^2}$$

$$y := \frac{x}{800 \text{ psi}} = 0.029 \frac{\text{gal}}{\text{day} \cdot \text{ft}^2 \text{ psi}}$$

$$y = 0.708 \frac{L}{\text{hr} \cdot \text{bar} \cdot \text{m}^2}$$

APPENDIX B

 Reading data base.

DATABASE
 SOLUTION_MASTER_SPECIES
 SOLUTION_SPECIES
 SOLUTION_SPECIES
 PHASES
 PHASES
 SURFACE_MASTER_SPECIES
 SURFACE_SPECIES
 END

 Reading input data for simulation 1.

SOLUTION 1
 temp 25
 pH 7
 pe 4
 redox pe
 units mmol/kgw
 density 1
 water 1 # kg
 REACTION 1 Initial Salt Solution
 NaCl 0.0342
 1 moles in 1 steps
 SAVE solution 2
 END

 Beginning of initial solution calculations.

Initial solution 1.

-----Solution composition-----

Elements	Molality	Moles
Pure water		

-----Description of solution-----

pH	=	7.000
pe	=	4.000
Activity of water	=	1.000
Ionic strength (mol/kgw)	=	1.004e-07
Mass of water (kg)	=	1.000e+00
Total alkalinity (eq/kg)	=	6.935e-10
Total carbon (mol/kg)	=	0.000e+00
Total CO2 (mol/kg)	=	0.000e+00
Temperature (°C)	=	25.00
Electrical balance (eq)	=	-6.935e-10
Percent error, $100 \cdot (\text{Cat} - \text{An}) / (\text{Cat} + \text{An})$	=	-0.35
Iterations	=	0
Total H	=	1.110137e+02
Total O	=	5.550683e+01

-----Distribution of species-----

Species	Molality	Activity	Log Molality	Log Activity	Log Gamma	mole V cm ³ /mol
OH-	1.007e-07	1.007e-07	-6.997	-6.997	-0.000	(0)
H+	1.001e-07	1.000e-07	-7.000	-7.000	-0.000	0.00
H2O	5.551e+01	1.000e+00	1.744	0.000	0.000	18.07
H(0)	1.416e-25					
H2	7.079e-26	7.079e-26	-25.150	-25.150	0.000	(0)
O(0)	0.000e+00					
O2	0.000e+00	0.000e+00	-41.995	-41.995	0.000	(0)

-----Saturation indices-----

Phase	SI**	log IAP	log K(298 K, 1 atm)
O2(g)	-39.09	44.00	83.09 O2

**For a gas, SI = log₁₀(fugacity). Fugacity = pressure * phi / 1 atm.
For ideal gases, phi = 1.

Beginning of batch-reaction calculations.

Reaction step 1.

Using solution 1.

Using reaction 1. Initial Salt Solution

Reaction 1. Initial Salt Solution

1.000e+00 moles of the following reaction have been added:

Reactant	Relative moles
NaCl	0.03420

Element	Relative moles
Cl	0.03420
Na	0.03420

-----Solution composition-----

Elements	Molality	Moles
Cl	3.420e-02	3.420e-02
Na	3.420e-02	3.420e-02

-----Description of solution-----

pH	=	6.998	Charge balance
pe	=	-1.079	Adjusted to redox equilibrium
Activity of water	=	0.999	
Ionic strength (mol/kgw)	=	3.420e-02	
Mass of water (kg)	=	1.000e+00	
Total alkalinity (eq/kg)	=	6.935e-10	
Total carbon (mol/kg)	=	0.000e+00	
Total CO2 (mol/kg)	=	0.000e+00	
Temperature (°C)	=	25.00	
Electrical balance (eq)	=	-6.935e-10	
Percent error, 100*(Cat- An)/(Cat+ An)	=	-0.00	
Iterations	=	8	

110
 Total H = 1.110137e+02
 Total O = 5.550683e+01

-----Distribution of species-----

Species	Molality	Activity	Log Molality	Log Activity	Log Gamma	mole V cm ³ /mol
OH-	1.198e-07	1.002e-07	-6.921	-6.999	-0.078	(0)
H+	1.191e-07	1.004e-07	-6.924	-6.998	-0.074	0.00
H2O	5.551e+01	9.988e-01	1.744	-0.001	0.000	18.07
Cl	3.420e-02					
Cl-	3.420e-02	2.882e-02	-1.466	-1.540	-0.074	(0)
H(0)	2.035e-15					
H2	1.017e-15	1.025e-15	-14.993	-14.989	0.003	(0)
Na	3.420e-02					
Na+	3.420e-02	2.882e-02	-1.466	-1.540	-0.074	(0)
O(0)	0.000e+00					
O2	0.000e+00	0.000e+00	-62.321	-62.318	0.003	(0)

-----Saturation indices-----

Phase	SI**	log IAP	log K(298 K, 1 atm)	
Halite	-4.68	-3.08	1.60	NaCl
O2(g)	-59.41	23.68	83.09	O2

**For a gas, SI = log₁₀(fugacity). Fugacity = pressure * phi / 1 atm.
 For ideal gases, phi = 1.

 End of simulation.

 Reading input data for simulation 2.

```

USE solution 2
REACTION 2 Scaling Soluiton
  CaCl2      0.0304
  Na2SO4     0.0304
  1 moles in 1 steps
End
  
```

 Beginning of batch-reaction calculations.

Reaction step 1.

Using solution 2. Solution after simulation 1.
 Using reaction 2. Scaling Soluiton

Reaction 2. Scaling Soluiton

1.000e+00 moles of the following reaction have been added:

Reactant	Relative moles
CaCl2	0.03040
Na2SO4	0.03040

Element	Relative moles
Ca	0.03040
Cl	0.06080

Na	0.06080
O	0.12160
S	0.03040

-----Solution composition-----

Elements	Molality	Moles
Ca	3.040e-02	3.040e-02
Cl	9.500e-02	9.500e-02
Na	9.500e-02	9.500e-02
S	3.040e-02	3.040e-02

-----Description of solution-----

pH	=	7.064	Charge balance
pe	=	-1.579	Adjusted to redox equilibrium
Activity of water	=	0.996	
Ionic strength (mol/kgw)	=	1.741e-01	
Mass of water (kg)	=	1.000e+00	
Total alkalinity (eq/kg)	=	6.935e-10	
Total carbon (mol/kg)	=	0.000e+00	
Total CO2 (mol/kg)	=	0.000e+00	
Temperature (°C)	=	25.00	
Electrical balance (eq)	=	-6.841e-10	
Percent error, 100*(Cat- An)/(Cat+ An)	=	-0.00	
Iterations	=	8	
Total H	=	1.110137e+02	
Total O	=	5.562843e+01	

-----Distribution of species-----

Species	Molality	Activity	Log Molality	Log Activity	Log Gamma	mole V cm ³ /mol
OH-	1.618e-07	1.162e-07	-6.791	-6.935	-0.144	(0)
H+	1.147e-07	8.629e-08	-6.940	-7.064	-0.124	0.00
H2O	5.551e+01	9.959e-01	1.744	-0.002	0.000	18.07
Ca	3.040e-02					
Ca+2	2.123e-02	6.807e-03	-1.673	-2.167	-0.494	(0)
CaSO4	9.165e-03	9.165e-03	-2.038	-2.038	0.000	(0)
CaOH+	2.065e-08	1.578e-08	-7.685	-7.802	-0.117	(0)
Cl	9.500e-02					
Cl-	9.500e-02	7.148e-02	-1.022	-1.146	-0.124	(0)
H(0)	1.458e-14					
H2	7.289e-15	7.587e-15	-14.137	-14.120	0.017	(0)
Na	9.500e-02					
Na+	9.210e-02	6.930e-02	-1.036	-1.159	-0.124	(0)
NaSO4-	2.899e-03	2.187e-03	-2.538	-2.660	-0.122	(0)
O(0)	0.000e+00					
O2	0.000e+00	0.000e+00	-64.076	-64.059	0.017	(0)
S(-2)	8.059e-20					
HS-	5.074e-20	3.108e-20	-19.295	-19.508	-0.213	(0)
H2S	2.809e-20	2.809e-20	-19.552	-19.552	0.000	(0)
S5-2	1.103e-21	1.554e-22	-20.957	-21.809	-0.851	(0)
S6-2	3.364e-22	4.737e-23	-21.473	-22.324	-0.851	(0)
S4-2	2.799e-22	3.942e-23	-21.553	-22.404	-0.851	(0)
S3-2	4.377e-23	6.163e-24	-22.359	-23.210	-0.851	(0)
S2-2	4.218e-24	5.939e-25	-23.375	-24.226	-0.851	(0)
S-2	5.776e-30	1.805e-30	-29.238	-29.743	-0.505	(0)
S(6)	3.040e-02					
SO4-2	1.834e-02	5.878e-03	-1.737	-2.231	-0.494	(0)
CaSO4	9.165e-03	9.165e-03	-2.038	-2.038	0.000	(0)
NaSO4-	2.899e-03	2.187e-03	-2.538	-2.660	-0.122	(0)
HSO4-	6.711e-08	4.957e-08	-7.173	-7.305	-0.132	(0)

-----Saturation indices-----

Phase	SI**	log IAP	log K(298 K,	1 atm)	
Anhydrite	-0.04	-4.40	-4.36		CaSO4
Gypsum	0.21	-4.40	-4.61		CaSO4:2H2O
H2S(g)	-18.56	-26.57	-8.01		H2S
Halite	-3.91	-2.31	1.60		NaCl
Lime	-20.74	11.96	32.70		CaO
Mirabilite	-3.45	-4.57	-1.11		Na2SO4:10H2O
O2(g)	-61.15	21.94	83.09		O2
Portlandite	-10.85	11.96	22.80		Ca(OH)2
Sulfur	-13.46	-15.60	-2.14		S
Thenardite	-4.87	-4.55	0.32		Na2SO4

**For a gas, SI = log10(fugacity). Fugacity = pressure * phi / 1 atm.
 For ideal gases, phi = 1.

 End of simulation.

REFERENCES

- Ahmed, Daniel, Stephen Benkovic, and Tony Jun Huang. "Spatiotemporal control of chemical microenvironment using oscillating microstructures." U.S. Patent Application 14/092,104, filed November 27, 2013.
- Altman, Susan J., Lucas K. McGrath, Howland DT Jones, Andres Sanchez, Rachel Noek, Paul Clem, Adam Cook, and Clifford K. Ho. "Systematic analysis of micromixers to minimize biofouling on reverse osmosis membranes." *Water research* 44, no. 12 pp 3545-3554, 2010.
- Amokrane, M., D. Sadaoui, C. P. Koutsou, A. J. Karabelas, and M. Dudeck. "A study of flow field and concentration polarization evolution in membrane channels with two-dimensional spacers during water desalination." *Journal of Membrane Science* 477 pp 139-150, 2015.
- Araújo, P. A., J. C. Kruithof, M. C. M. Van Loosdrecht, and J. S. Vrouwenvelder. "The potential of standard and modified feed spacers for biofouling control." *Journal of Membrane Science* 403 pp 58-70, 2012.
- Barger, Marilyn, Drew Hoff, Robert P. Carnahan, and Richard A. Gilbert. "Reverse osmosis ("RO") membrane system incorporating function of flow channel spacer." U.S. Patent 6,632,357, issued October 14, 2003.
- Bucs, Sz S., A. I. Radu, V. Lavric, J. S. Vrouwenvelder, and C. Picioreanu. "Effect of different commercial feed spacers on biofouling of reverse osmosis membrane systems: A numerical study." *Desalination* 343 pp 26-37, 2014.

- Bucs, Sz S., A. I. Radu, V. Lavric, J. S. Vrouwenvelder, and C. Picioreanu. "Experimental and numerical characterization of the water flow in spacer-filled channels of spiral-wound membranes." *Water Research* 87 pp 29-310, 2015.
- Bystrianský, Martin, et al. "The presence of ferric iron promotes calcium sulphate scaling in reverse osmosis processes." *Desalination* 393 (2016): 115-119.
- Cohen, Yoram, Raphael Semiat, and Anditya Rahardianto. "A perspective on reverse osmosis water desalination: Quest for sustainability." *AIChE Journal* 63.6 (2017): 1771-1784.
- Cooper, K. G., et al. "The threshold scale inhibition phenomenon." *Desalination* 31.1-3 (1979): 257-266.
- Downing, Edward A., Amos J. Coleman, and Thomas H. Bagwell Jr. "US Army reverse osmosis membrane research programs." *Desalination* 99.2-3 (1994): 401-408.
- Environmental Protection Agency (EPA). *Membrane Filtration Guidance Manual*. Washington, D.C., United States: Office of Water, 2005.
- Feng, D., J. S. J. van Deventer, and C. Aldrich. "Ultrasonic defouling of reverse osmosis membranes used to treat wastewater effluents." *Separation and Purification Technology* 50, no. 3 pp. 318-323, 2006.
- Fimbres-Weihs, G. A., and D. E. Wiley. "Review of 3D CFD modeling of flow and mass transfer in narrow spacer-filled channels in membrane modules." *Chemical Engineering and Processing: Process Intensification* 49.7 (2010): 759-781
- Gallab, A. A. S., et al. "Effect of Different Salts on Mass Transfer Coefficient and Inorganic Fouling of TFC Membranes." *J Membr Sci Technol* 7.175 (2017): 2.
- Gimmelshtein, Margarita Modek, and Raphael Semiat. "Investigation of flow next to membrane walls." *Journal of Membrane Science* 264.1-2 (2005): 137-150.

Guillen, Greg, and Eric MV Hoek. "Modeling the impacts of feed spacer geometry on reverse osmosis and nanofiltration processes." *Chemical Engineering Journal* 149, no. 1 pp 221-231, 2009.

Ho, Clifford K., et al. "Analysis of micromixers to reduce biofouling on reverse-osmosis membranes." *Environmental progress* 27.2 (2008): 195-203.

Ho, Winston, and Kamallesh Sirkar. *Membrane handbook*. Springer Science & Business Media, 2012.

<http://www.biobots.io/>

Hydranautics." Technical Service Bulletin 207.01 for Foulants and cleaning procedures for sanitary, food processing type composite polyamide RO/NF membrane elements" Nitto Group Company August 2016.

Karabelas, A. J., A. Karanasiou, and D. C. Sioutopoulos. "Experimental study on the effect of polysaccharides on incipient membrane scaling during desalination." *Desalination* 416 (2017): 106-121.

Karabelas, A. J., A. Karanasiou, and S. T. Mitrouli. "Incipient membrane scaling by calcium sulfate during desalination in narrow spacer-filled channels." *Desalination* 345 (2014): 146-157.

Karabelas, A. J., M. Kostoglou, and S. T. Mitrouli. "Incipient crystallization of sparingly soluble salts on membrane surfaces: The case of dead-end filtration with no agitation." *Desalination* 273.1 (2011): 105-117.

Kodým, R., F. Vlasák, D. Šnita, A. Černín, and K. Bouzek. "Spatially two-dimensional mathematical model of the flow hydrodynamics in a channel filled with a net-like spacer." *Journal of Membrane Science* 368, no. 1 pp 171-183, 2011.

- Koutsou, C. P., S. G. Yiantsios, and A. J. Karabelas. "Direct numerical simulation of flow in spacer-filled channels: effect of spacer geometrical characteristics." *Journal of Membrane Science* 291, no. 1 pp 53-69, 2007.
- Koutsou, C. P., S. G. Yiantsios, and A. J. Karabelas. "Direct numerical simulation of flow in spacer-filled channels: effect of spacer geometrical characteristics." *Journal of Membrane Science* 291, no. 1 pp 53-69, 2007.
- KrishnaáJuluri, Bala, and Tony JunáHuang. "A millisecond micromixer via single-bubble-based acoustic streaming." *Lab on a Chip* 9, no. 18 pp 2738-2741, 2009.
- Le Gouellec, Yann A., and Menachem Elimelech. "Calcium sulfate (gypsum) scaling in nanofiltration of agricultural drainage water." *Journal of Membrane Science* 205.1-2 (2002): 279-291.
- Lee, Sangho, and Chung-Hak Lee. "Effect of operating conditions on CaSO₄ scale formation mechanism in nanofiltration for water softening." *Water Research* 34.15 (2000): 3854-3866.
- Liu, Jiuqing, Ashkan Iranshahi, Yuecun Lou, and Glenn Lipscomb. "Static mixing spacers for spiral wound modules." *Journal of Membrane Science* 442 pp 140-148, 2013.
- Maruf, Sajjad H., et al. "Fabrication and characterization of a surface-patterned thin film composite membrane." *Journal of Membrane Science* 452 pp 11-19, 2014.
- Miller, Daniel J., Paula A. Araujo, Patricia B. Correia, Matthew M. Ramsey, Joop C. Kruithof, Mark CM van Loosdrecht, Benny D. Freeman, Donald R. Paul, Marvin Whiteley, and Johannes S. Vrouwenvelder. "Short-term adhesion and long-term biofouling testing of polydopamine and poly (ethylene glycol) surface modifications of membranes and feed spacers for biofouling control." *water research* 46, no. 12 pp 3737-3753, 2012.

- Mulder, J. Basic principles of membrane technology. Springer Science & Business Media, 1991.
- Nam, Jong-Woo, et al. "The evaluation on concentration polarization for effective monitoring of membrane fouling in seawater reverse osmosis membrane system." *Journal of Industrial and Engineering Chemistry*, 2013.
- Ngene, Ikenna S., et al. "Particle deposition and biofilm formation on microstructured membranes." *Journal of membrane science* 364.1-2 (2010): 43-51.
- Paul, David, and Abdul Rahman M. Abanmy. "Reverse osmosis membrane fouling—the final frontier." *Ultra Pure Water* 7.3 (1990): 25-36.
- Picioreanu, C., J. S. Vrouwenvelder, and M. C. M. Van Loosdrecht. "Three-dimensional modeling of biofouling and fluid dynamics in feed spacer channels of membrane devices." *Journal of Membrane Science* 345, no. 1 pp 340-354, 2009.
- R.L. Riley and C.E. Milstead, Evaluation of RO feedwater spacers final report. US Army Report, Contract DAAK70-91-P-0581, 1992.
- Radu, A. I., J. S. Vrouwenvelder, M. C. M. Van Loosdrecht, and C. Picioreanu. "Modeling the effect of biofilm formation on reverse osmosis performance: flux, feed channel pressure drop and solute passage." *Journal of Membrane Science* 365, no. 1 pp 1-15, 2010.
- Radu, A. I., J. S. Vrouwenvelder, M. C. M. Van Loosdrecht, and C. Picioreanu. "Modeling the effect of biofilm formation on reverse osmosis performance: flux, feed channel pressure drop and solute passage." *Journal of Membrane Science* 365, no. 1 pp 1-15, 2010.
- Rasband, W.S., ImageJ, U. S. National Institutes of Health, Bethesda, Maryland, USA, <https://imagej.nih.gov/ij/>, 1997-2018.
- Schwinge, J., D. E. Wiley, and A. G. Fane. "Novel spacer design improves observed flux." *Journal of membrane Science* 229.1-2 (2004): 53-61.

Shmulevsky, Marina, et al. "Analysis of the onset of calcium sulfate scaling on RO membranes."

Journal of Membrane Science 524 (2017): 299-304.

Solutions, Water. "FILMTEC™ Reverse Osmosis Membranes." *Technical Manual, Form 609-*

00071 (2010): 1-180.

Suwarno, S. R., X. Chen, T. H. Chong, V. L. Puspitasari, D. McDougald, Y. Cohen, Scott Alan

Rice, and Anthony Gordon Fane. "The impact of flux and spacers on biofilm

development on reverse osmosis membranes." *Journal of Membrane Science* 405 pp 219-

232, 2012.

Thompson, John, et al. "Real-time direct detection of silica scaling on RO membranes." *Journal*

of Membrane Science 528 (2017): 346-358.

Vrouwenvelder, J. S., DA Graf Von Der Schulenburg, J. C. Kruithof, M. L. Johns, and M. C. M.

Van Loosdrecht. "Biofouling of spiral-wound nanofiltration and reverse osmosis

membranes: a feed spacer problem." *Water Research* 43, no. 3 pp 583-594, 2009.

Vrouwenvelder, J. S., J. A. M. Van Paassen, L. P. Wessels, A. F. Van Dam, and S. M. Bakker.

"The membrane fouling simulator: a practical tool for fouling prediction and control."

Journal of Membrane Science 281, no. 1 pp 316-324, 2006.

Walker, S. J. "Growth of Biological Films on Reverse Osmosis Membranes". Baltimore: Johns

Hopkins University, 1986.

Wang, Jinwen, et al. "A critical review of transport through osmotic membranes." *Journal of*

Membrane Science 454 (2014): 516-537.

Wang, Jinwen, et al. "Effects of water chemistry on structure and performance of polyamide

composite membranes." *Journal of Membrane Science* 452 (2014): 415-425.

- Wijmans, Johannes G., and Richard W. Baker. "The solution-diffusion model: a review." *Journal of membrane science* 107.1-2 (1995): 1-21.
- Xie, Peng, Lawrence C. Murdoch, and David A. Ladner. "Hydrodynamics of sinusoidal spacers for improved reverse osmosis performance." *Journal of Membrane Science* 453 (2014): 92-99.
- Yang, Xing, Rong Wang, Anthony G. Fane, Chuyang Y. Tang, and I. G. Wenten. "Membrane module design and dynamic shear-induced techniques to enhance liquid separation by hollow fiber modules: a review." *Desalination and Water Treatment* 51, no. 16-18 pp 3604-3627, 2013.

ABSTRACT**ANALYSIS OF MICROMIXERS TO MINIMIZE SCALING EFFECTS ON
REVERSE OSMOSIS MEMBRANES**

by

Jeremy Stephen Walker**December 2018****Advisor:** Dr. Shawn McElmurry**Major:** Civil Engineering**Degree:** Doctor of Philosophy

Structural elements, typically mesh spacers, are required between membrane leaves in spiral wound elements to ensure flow through reverse osmosis (RO) modules. The standard diamond-shaped mesh spacer results in non-ideal hydrodynamics that can lead to fouling, which ultimately reduces the flux of water through the membrane and the operational life of the unit. Additionally, traditional mesh feed spacers do not allow for reverse flow cleaning due to obstructed flow paths and, once fouled, the entrapment of scale. To address this shortcoming, a novel method for separating RO membrane leaves in spiral wound elements is developed and evaluated.

Three-dimensional (3-D) printing was utilized to manufacture micromixers directly on membrane swatches. To enhance performance, a two-dimensional computational fluid dynamic model was used to select the optimal geometry and pattern of 3-D printed micromixers. The optimal geometry selected created unhindered flow between 0.2 m/s and 0.3m/s, using an inlet flow velocity of 0.104 m/s, across 40% of the membrane surface.

Laboratory experiments were conducted to evaluate the performance of micromixers and compared to unmodified membranes with a standard 20 mil (0.508 mm) mesh feed spacer. Pure water flux and salt rejection were found to be similar to standard membranes, indicating the 3-D printing process did not damage intrinsic membrane properties. Calcium sulfate scaling experiments were conducted. Scale initially began to form within 2 hours of treatment resulting in a flux decline of approximately 10% for both modified and unmodified membranes. Over 14 hours, an average flux decrease of 24% was observed for modified membranes compared to an average flux decrease of 78% for the unmodified membranes. This demonstrated the improved resistance to fouling created by the open channel design with optimal flow conditions.

Based on the open-channel flow paths created using 3-D printed micromixers, improved scale removal by reverse flow cleaning procedures was evaluated. The modified membranes showed 5-10% more removal for calcium sulfate compared to the unmodified membrane utilizing a 20 mil (0.508 mm) mesh feed spacer. Following cleaning, all three unmodified membranes and feed spacers had significant remaining scale, while all three modified membranes showed minimal scale.

Micromixers printed directly to the membrane surface offers the ability to optimize feed channel hydrodynamics, reduce scale formation, minimize flux decline, and allow for reverse flow cleaning of fouled membranes, representing a significant advancement in membrane technology.

AUTOBIOGRAPHICAL STATEMENT

I graduated from the University of South Florida in 1998 with a B.S. in Civil Engineering. I moved to Michigan upon completion of my degree and started working fulltime for the United States Army as a civilian in the capacity of a project engineer. I finished my M.S. in Environmental Health from the University of Michigan, Ann Arbor in 2013 while working fulltime. I promptly began my PhD journey in Civil Engineering at Wayne State University the summer of 2013. I will continue working as an experimenter civil engineer for the US Army.